université PARIS-SACLAY

First study of the 6-neutron system from the decay of resonances in ^{10}He

Première étude du système de 6 neutrons via la décroissance des résonances d' ^{10}He

Thèse de doctorat de l'université Paris-Saclay

École doctorale n°576 Particules, hadrons, énergie et noyaux : instrumentation, image, cosmos et simulation (PHENIICS)
Spécialité de doctorat : Physique Nucléaire
Graduate School : Physique, Référent : Faculté des sciences d'Orsay

Thèse préparée dans l'unité de recherche **IJCLab** (Université Paris-Saclay, CNRS), sous la direction de **Didier BEAUMEL**, Directeur de recherche CNRS, IJCLab Orsay, et le co-encadrement de **Pengjie LI**, Chercheur-Ingenieur, Université de Fudan, Shanghai.

Thèse soutenue à Paris-Saclay, le 27 Mai 2026, par

Omar Nasr

Composition du jury

Membres du jury avec voix délibérative

Anna CORSI Directrice de recherche, CEA, Université Paris-Saclay	Présidente
Alexandre OBERTELLI Professeur, Institut für Kernphysik, Technische Universität Darmstadt	Rapporteur & Examinateur
Dolores CORTINA Professeure, Instituto de Física Corpuscular, CSIC-UV	Rapporteure & Examinatrice
François DE OLIVEIRA Directeur de recherche CNRS, GANIL	Examinateur

THESE DE DOCTORAT

NNT : 2026UPASP030

université PARIS-SACLAY

ÉCOLE DOCTORALE
Particules, hadrons, énergie et noyau : instrumentation, imagerie, cosmos et simulation (PHENIICS)

Titre : Première étude du système de 6 neutrons via la décroissance des résonances d' ^{10}He
Mots clés : Multineutrons, noyaux légers riches en neutrons, réactions de knock-out de clusters, masse manquante, ^{10}He état fondamental, résonances dans l' ^{10}He.

Résumé : La recherche de systèmes à plusieurs neutrons liés ou résonants reste un défi de longue date tant en physique nucléaire théorique qu'expérimentale. Cette thèse se concentre sur l'analyse de nouvelles données obtenues au RIKEN concernant le système à six neutrons (6n). Pour la première fois, le spectre d'énergie expérimental de ce système a été déterminé. Le mécanisme de production implique la désintégration alpha en vol d'isotopes ^{10}He non liés, générés par la réaction de knockout de cluster $^{14}\mathrm{Be}(p, p-\alpha)^{10}\mathrm{He}^*$ en cinématique inverse. Cette approche a également permis de déterminer les résonances dans le ^{10}He, qui ont ensuite été comparées à la littérature existante.

L'expérience a été menée avec succès au RIKEN/RIBF à l'aide du spectromètre SAMURAI prealablement a la these. L'analyse des données effectuee durant la these a permis d'extraire le spectre à 6 neutrons par reconstruction de la masse manquante — une première dans le domaine. Des calculs d'espace de phase ont été effectués et superposés aux données expérimentales afin d'identifier des résonances potentielles. En outre, les résonances dans le ^{10}He ont été caractérisées et comparées aux résultats publiés précédemment.

Title: First study of the 6-neutron system from the decay of resonances in ^{10}He
Keywords: Multineutrons, light neutron-rich nuclei, cluster knockout reactions, missing mass, ^{10}He ground state, resonances in ^{10}He.

Abstract: The search for bound or resonant multineutron systems remains a longstanding challenge in both theoretical and experimental nuclear physics. This thesis focuses on the analysis of novel data obtained at RIKEN concerning the six-neutron (6n) system. For the first time, the experimental energy spectrum of this system was extracted. The production mechanism involves the in-flight alpha decay of unbound ^{10}He isotopes, generated via the $^{14}\mathrm{Be}(p, p\alpha)^{10}\mathrm{He}^*$ cluster knockout reaction in inverse kinematics. This approach also enabled the determination of resonances in ^{10}He, which were subsequently compared to existing literature.

The experiment was successfully conducted at RIKEN/RIBF using the SAMURAI spectrometer prior to the thesis. Data analysis performed during the thesis led to the extraction of the 6-neutron spectrum through missing-mass reconstruction for the first time. Phase-space calculations were performed and overlaid on the experimental data to identify potential resonances. As an additional outcome, resonances in ^{10}He were characterized and benchmarked against previously published results.

Contents

1 Introduction **15**

1.1 Motivation 15

1.2 Brief history of multineutron experimental studies 18

1.2.1 GANIL: First RIB experiment 19

1.2.2 RIKEN: 4*n* experiment: Kisamori et al. (2016) 22

1.2.3 RIKEN 4n experiment: Duer et. al. (2022) 23

1.2.4 RIKEN: 3n experiment 26

1.2.5 Stable beam experiment 28

1.3 Beyond the 4*n* system 29

1.4 Our approach to study 6-neutron system 30

2 Experimental setup **31**

2.1 Overview 31

2.2 Beam 34

2.2.1 Primary beam 34

2.2.2 Secondary beam (BigRIPS) 35

2.3 Beamline detectors 37

2.3.1 Beamline plastics 38

2.3.2 Beamline Drift chambers 38

2.4 Solid Hydrogen Target 40

2.5 Recoil protons detection (ESPRI) 41

2.5.1 RDC . . . 42
2.5.2 Plastic scintillator . . . 42
2.5.3 NaI(Tl) scintillator . . . 43
2.6 Cluster detection system (Telescope) . . . 43
2.7 SAMURAI magnet . . . 45
2.8 Residual nucleus detection . . . 47
2.8.1 Forward drift chambers . . . 48
2.8.1.1 FDC0 . . . 48
2.8.1.2 FDC2 . . . 48
2.8.2 Hodoscope . . . 48
2.9 Neutrons detection (NEBULA) . . . 50
2.10 Triggers . . . 52

3 Analysis **55**
3.1 Beam Plastics . . . 56
3.1.1 Time-of-flight calibration . . . 57
3.1.1.1 Slew effect . . . 57
3.1.1.2 Position dependence . . . 58
3.1.2 Beam energy (ToF) and particle identification . . . 60
3.2 Beam Drift chambers . . . 61
3.2.1 Calibration . . . 62
3.2.2 Track reconstruction and residue . . . 63
3.2.3 Beam profile on target . . . 66
3.2.4 Position resolution . . . 68
3.3 ESPRI . . . 69
3.3.1 RDC calibration . . . 70
3.3.2 NaI(Tl) energy calibration . . . 72
3.3.3 Plastic time-of-flight . . . 73
3.3.3.1 Time calibration . . . 73

3.3.3.1.1 Position correction . . . 74
3.3.3.1.2 Slew correction . . . 75
3.3.3.2 Excitation energy . . . 77
3.3.3.3 Time of flight correction . . . 78
3.3.3.4 ESPRI particle identification . . . 81
3.4 Telescope . . . 81
3.4.1 DSSD energy calibration . . . 82
3.4.2 CsI(Tl) energy calibration . . . 84
3.4.3 Alpha particle identification . . . 86
3.5 Hodoscope . . . 87
3.5.1 Particle identification . . . 87
3.6 Magnetic rigidity ($B\rho$) of decay alpha . . . 87
3.6.1 FDC2 . . . 88
3.6.2 FDC2 alignment with hodoscope . . . 90
3.6.3 Magnetic field map . . . 92
3.6.4 $B\rho$ reconstruction . . . 93
3.6.4.1 Propagation in the magnetic field . . . 93
3.6.4.2 NPTool logic . . . 95
3.6.5 $B\rho$ extraction and resolution . . . 95

4 Results and Discussion **99**

4.1 Status of ^{10}He spectroscopy . . . 99
4.1.1 ^{10}He excitation energy spectrum . . . 101
4.1.2 Voigt fit . . . 102
4.1.3 Resolution determination from simulation for the ^{10}He spectrum . . . 103
4.1.4 Decomposition of the ^{10}He spectrum in ^{8}He channel . . . 106
4.1.5 New results on ^{10}He . . . 110
4.2 Calculation of the 6-neutron system energy . . . 111
4.2.1 Background reduction . . . 111

4.2.2 Resolution of 6-neutron energy spectra from simulation 112
4.2.3 Phase-space calculation 114
4.2.3.1 6-neutron system phase-space 116
4.2.4 Comparison of 6-neutron spectra with phase-space calculations 116

5 Conclusions and perspectives **123**
5.1 Conclusions 123
5.2 Prospective 124

A Three-body Kinematics **125**

B Lorentz Invariant Phase Space calculation **129**

Résumé en français **141**
Motivation 141
Dispositif expérimental 142
Analyse 143
Résultats et discussion 143
Conclusion 144

List of Figures

1.1 Nuclear chart up to Z=10 (Neon) with possible multineutrons highlighted in red. 16

1.2 Experimental setup inside the vacuum chamber. From left to right: the beam tracking detectors, the target, and the telescope for the detection of charged fragments (see text) [18]. 19

1.3 Scatter plot of the PID vs the (E_p/E_n) ratio for the data from the $(^{14}\mathrm{Be}, X + n)$ reaction, with the PID projection shown on the left and horizontal dashed lines indicating ^{14}Be events within the PID and vertical dashed line indicating the threshold of 1.4 for multineutron detection [18]. 20

1.4 Experimental setup of the $^{8}\mathrm{He}(d,^{6}\mathrm{Li})4n$ experiment performed at GANIL (left) (figure from [23]). Excitation energy spectrum of the $4n$ system (right). 21

1.5 Missing-mass spectrum of the tetraneutron system. The solid (red) curve represents the sum of the direct decay of correlated two-neutron pairs and the estimated background. The dashed (blue) curve represents the estimated background multiplied by a factor of 10 [25]. 23

1.6 Quasi-elastic scattering of the ^{4}He core from a ^{8}He projectile off a proton target in the laboratory frame. The length of the arrows represents the momentum per nucleon (the velocity) of the incoming and outgoing particles. Z_{beam} is the beam axis [27]. 24

1.7 Schematic overview of the setup [27]. 24

1.8 Missing mass spectrum of the tetraneutron system extracted from the $^{8}\mathrm{He}(p, p\alpha)$ reaction. The different curves represent a Breit–Wigner resonance (pink), a non-resonant continuum (dashed blue), the background from two step processes (green) and the total sum (solid blue) [27]. 25

1.9 Double-differential cross-section spectra for the ^{3}H(t,^{3}He)3n (red) and ^{3}He(^{3}He,t)3p (blue) reactions. The error bars and shaded regions represent the statistical and systematic uncertainties, respectively. The numbers in parentheses represent the average momentum transfers $q_{c.m.}$ [MeV/c] (left). Comparison of the theoretical calculations with the experimental data (right). The theoretical calculations are the quasi-free calculations (top), and the F-P calculations without (middle) and with (bottom) a phenomenological 3NF [33]. . . 27

1.10 Comparison between the ^{3}He inter-atomic potential and the n-n potential in the singlet state [2]. 29

2.1 A schematic view of SAMURAI12 quasi-free scattering experiment at RIBF facility [51]. . 31

2.2 Schematic of SAMURAI12 experimental setup [51]. 32

2.3 Schematic view of ESPRI and Telescope around SHT during $(p, p\alpha)$ reaction [51]. 33

2.4 RIBF accelerator mode AVF+RRC+SRC [51]. 35

2.5 Schematic overview of BigRIPS for SAMURAI spectrometer. 35

2.6 Schematic representation of detectors at F5 focal point (figure from [31]). 36

2.7 Schematic view of branching beamlines of BigRIPS (figure from [31]). 37

2.8 Distances between beamline plastics at focal points F3,F7, and F13. 38

2.9 BDC schematic view [Front view(Left), Top view(right)](figure from [39]). 39

2.10 Schematic view of SHT chamber window materials (left). Picture of SHT with a hole highlighted by dashed line taken during the experiment (right)[51]. 41

2.11 Schematic view of the layers of ESPRI. 43

2.12 Top view of Telescope arms (left) and detector configuration scheme (right). 44

2.13 Schematic view of iron component of the SAMURAI magnet. X-Z plane view (top left), X-Y plane view (bottom left), Y-Z plane view (bottom right) (figure from [39]) 46

2.14 Trajectory calculations for beam and residues of interest in the case of ^{14}Be beam at 150 MeV/u. (Color code black:beam; red:^{4}He; blue:^{8}He). 47

2.15 FDC2 schematic view [39]. 49

2.16 Hodoscope view of SAMURAI12. 50

2.17 Schematic view of NEBULA [39]. 51

2.18 Typical configuration of RIBF DAQ (figure from [62]). 53

3.1 Scheme of plastic scintillator. 56

3.2 Illustration of the time walk effect (figure from [63]). 58

3.3 Correction of the slew effect on time-of-flight (ToF). 59

3.4 ^{12}Be SBT1 position correction in log Z scale. 60

3.5 SAMURAI12 particle identification(Log Z scale) for three physics beam settings. 61

3.6 Scheme of the tracking process in the drift chamber. 62

3.7 Example of BDC1/2 and FDC0 STC. 63

3.8 Example of the reconstruction of a track. 64

3.9 BDC1, BDC2, and FDC0 residue in X and Y. 65

3.10 Beam position and angle reconstruction on target for ^{12}Be beam (a, b) and ^{14}Be beam (c, d). 67

3.11 Scheme of BDC1, BDC2, SHT, and FDC0 to illustrate reconstruction of beam position on target. 68

3.12 Difference between measured and interpolated BDC2 position. BDC2 X(left). BDC2 Y(right). 69

3.13 Example of RDC STC. 71

3.14 Right arm ESPRI RDC residue. 71

3.15 ^{10}Be proton energy vs angle from Lise++ (figure from [51]). 72

3.16 NaI(Tl) ADC vs proton angle (left); NaI(Tl) energy calibration fit (right) figures obtained from [51]. 73

3.17 ESPRI plastic ΔY vs ΔT plot before (left) and after (right) position correction. 75

3.18 ESPRI plastic ΔT plot before (blue) and after (red) position correction. 75

3.19 ESPRI plastic ΔT vs Charge plot before (left) and after (right) time walk correction. 76

3.20 ESPRI plastic ΔT plot before (blue) and after (red) slew correction. 76

3.21 77

3.22 ^{12}Be beam ^{8}He excitation energy vs. proton energy deduced from ToF pre ToF correction (left), and post ToF correction (right). 78

3.23 Proton ToF deduced vs measured by the plastic with fit (red), 45° line (green) and black dotted lines corresponding to proton energy in MeV of different ToF. 80

3.24 80

3.25 ^{14}Be ESPRI PID plots. 82

3.26 Illustration of DSSD SCM figure obtained from [66]. 83

3.27 ADC correlation between 13th back strip and 14th front strip before (left) and after (right) alignment figures obtained from [51]. 84

3.28 DSSD energy spectrum (left) and corresponding calibration plot with two points (right) figures obtained from [51]. 84

3.29 SHT copper frame interactions with beam. 85

3.30 Telescope CsI(Tl) calibration (left) and energy spectrum (right) figures obtained from [51]. 86

3.31 Telescope particle identification with alpha cut in red. 86

3.32 Hodoscope particle identification for a single bar. HODF(left), HODP(right). 87

3.33 89

3.34 FDC2 X and V layers residue when including U layers (black) vs when excluding U layers (red). 90

3.35 FDC2 XY position plot with target area and beam PID conditions (left). FDC2 XY position plot with target area, beam PID, and ^{4}He HOD gate conditions (right). 91

3.36 Schematic diagram illustrating FDC2 and hodoscope placement. The blue dashed line represents a nucleus exiting the magnet and hitting two adjacent hodoscope bars. 91

3.37 Extrapolation of FDC2 on Hodoscope bars when two adjacent bars have been tagged (left). Zoom in of left figure with a fitted Gaussian (right). 92

3.38 Schematic diagram of the SAMURAI magnet showing entry position detection with FDC0 (red star) and extrapolated position at FDC2 (blue star). 96

3.39 ^{4}He beam energy distribution measured with the plastic detectors placed at F7 and F13. . . 97

3.40 $B\rho$ reconstruction of ^{4}He beam with a Gaussian fit in red. 97

3.41 SBT1 time (left), SBT2 time (right) both with a Gaussian fit. 98

4.1 Relative energy spectrum of the ^{8}He + 2n system from the ^{1}H(^{11}Li,^{8} He + 2n) reaction. Experimental data are shown as filled circles with error bars. The dashed and dotted lines describe Breit–Wigner shaped resonances. The solid line is the sum of these two components. (Fig. from [73]). 100

4.2 ^{10}He excitation energy relative to the threshold of 2n emission with ^{8}He HOD gate in black and ^{4}He HOD gate in red. 102

4.3 ^{10}He simulation with a Gaussian fit for each 1 MeV excitation energy bin. 105

4.4 Excitation energy versus resolution (σ) obtained from Gaussian fits to each 1 MeV bin (Black:pre correction, Red:post correction). 105

4.5 ^{10}He energy spectrum from ^{14}Be$(p, p\alpha)^{10}$He reaction w.r.t. ^{8}He+2n fit with Voigt function of 1 resonance. 106

4.6 ^{10}He energy spectrum from ^{14}Be$(p, p\alpha)^{10}$He reaction w.r.t. ^{8}He+2n fit with Voigt function of 2 resonances. 107

4.7 ^{10}He energy spectrum from ^{14}Be$(p, p\alpha)^{10}$He reaction w.r.t. ^{8}He+2n fit with Voigt function of 3 resonances. 107

4.8 The experimental three-body decay energy of ^{10}He is shown as solid black circles with statistical error bars. A Breit-Wigner resonance [solid gray (red) line] and non-resonant background (short dashed blue line) from the Monte Carlo simulation have been fit to the experimental distribution. The sum of the Breit-Wigner and non-resonant components is shown as a solid black line (χ^2/μ = 0.75). The inset shows a fit to the experimental data which includes the population of the first excited state at 4 MeV (long dashed green line) as measured in [73](Fig. obtained from [74]). 108

4.9 (Color online) ^{8}He$-n-n$ relative energy spectrum obtained from the ^{11}Li$(p,2p)$ reactions compared to two previous results from RIKEN [71] and GSI [73] (both efficiency corrected and re-scaled to match the peak height of current data). The errors shown are statistical. The data are also compared to theoretical calculation (black solid line) that is decomposed to three components: $^{8}\mathrm{He}_{g.s} + [1s_{1/2}]^2$ (red dashed line), $^{8}\mathrm{He}_{g.s} + [0p_{1/2}]^2$ (blue dashed line) and others (two neutrons in partial waves other than $1s_{1/2}$ and $0p_{1/2}$, green dashed line). The upper panel displays the $2n$ detection efficiency after the cross-talk rejection. . . 110

4.10 (left)^{10}He energy relative to the threshold of $2n$ emission with ^{4}He HOD gate without NEBULA trigger (black), with NEBULA trigger (red), and the blue shade represents the range of energies above threshold for $6n$ emission. (right) $6n$ spectrum corresponding to ^{10}He excitation energy covered by blue shade without NEBULA trigger (black), and with NEBULA trigger (red). 112

4.11 σ vs E_{6n} for the $6n$ simulation obtained from fitting each 1 MeV bin with a Gaussian (Black:pre correction, Red:post correction). 114

4.12 Example of recurring process taking place in the phase-space calculation code (E, and Ω are the energy and direction respectively). 115

4.13 $6n$ energy from phase-space calculation vs. the corresponding energy in ^{10}He w.r.t. ^{8}He+$2n$ threshold with the three ranges of energy considered highlighted (Red:3-7 MeV, Green:7-11 MeV, and Violet:11-15 MeV). 116

4.14 (left)^{10}He energy relative to the threshold of $2n$ emission with ^{4}He HOD gate and NEBULA trigger. (right) $6n$ spectrum corresponding to ^{10}He energy (0-15) MeV (red) and normalized phase-space (blue). 117

4.15 (left)^{10}He energy relative to the threshold of $2n$ emission with ^{4}He HOD gate with NEBULA trigger (red). (right) $6n$ spectrum corresponding to ^{10}He energy covered by blue shade (red) and normalized phase-space (blue). R_1:[a-b], R_2:[c-d], and R_3:[e-f]. 118

4.16 Experimental $6n$ excitation energy obtained after the subtraction of the phase-space calculation for different energy range regions of ^{10}He w.r.t. ^{8}He + $2n$ energy. 120

4.17 Experimental 6*n* excitation energy spectrum corresponding to ^{10}He energy $-5 < E_{^{10}He} < 3$ MeV (left) and $0 < E_{^{10}He} < 3$ MeV (right). 121

4.18 Experimental 6*n* excitation energy spectrum corresponding to ^{10}He energy $-20 < E_{^{10}He} < -10$ MeV. 121

List of Tables

2.1 BigRIPS parameters 37
2.2 BDC parameters 40
2.3 RDC parameters 42
2.4 Telescope parameters. 45
2.5 SAMURAI dipole magnet parameters [40] 46
2.6 SAMURAI12 magnetic flux density settings. 47
2.7 FDC2 parameters [39] 49
2.8 NEBULA parameters [61] 52
2.9 Trigger list of the S12 experiment. 54
2.10 S12 experiment run summary. 54

3.1 Beam spot characteristics. 68
3.2 Telescope energy loss for each beam setting 82
3.3 Telescope CsI(Tl) energy for each case. 85

4.1 Parameter condition used for the Voigt fit with two resonances (orange boxes for fixed parameters, and green boxes for limited parameters). 109
4.2 Parameter condition used for the Voigt fit with three resonances (orange boxes for fixed parameters, and green boxes for limited parameters). 109

Chapter 1

Introduction

This thesis studies the data obtained from the SAMURAI12 collaboration experiment performed at the RIBF facility at the RIKEN Nishina Center in Spring of 2018. The analysis was done to extract the first 6-neutron spectra obtained from the decay of resonances in ^{10}He. As a byproduct of the analysis, new information on the spectroscopy of ^{10}He could be extracted.

1.1 Motivation

Understanding the nuclear system relies on theoretical models that describe the nucleon–nucleon interaction within the nucleus. Among these, the liquid-drop model provides an overall solid description of nuclear binding energies across the nuclear chart. For a nucleus consisting of **Z** protons and **N** neutrons, the binding energy can be expressed as

$$B(Z,N) = a_v A - a_s A^{\frac{2}{3}} - a_c \frac{Z^2}{A^{\frac{1}{3}}} - a_a \frac{(N-Z)^2}{A} \pm \frac{\delta}{A^{\frac{1}{2}}} \tag{1.1}$$

where the first three terms correspond to the volume, surface, and Coulomb contributions, that reflect the analogy of the nucleus being a charged liquid drop. The remaining terms account for the asymmetry between neutrons and protons and pairing effects, respectively, which arise from quantum properties of the nucleus [1].

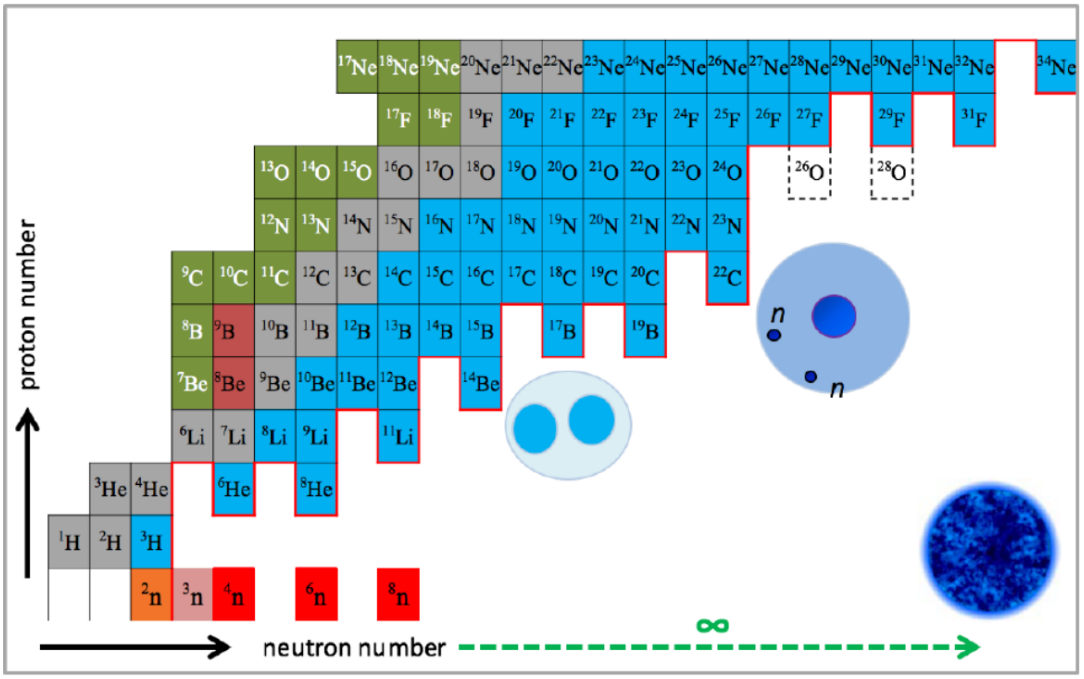


Figure 1.1: Nuclear chart up to Z=10 (Neon) with possible multineutrons highlighted in red.

The liquid-drop model was able to demonstrate the properties of most the nuclei in the valley of stability which exhibit properties like a liquid drop such as radial border ($R \approx r_0 A^{\frac{1}{3}}$), constant density within that border ($\rho(r) \approx \rho_0$), and a homogeneous nucleon mixture ($\rho_n(r) \approx \frac{N}{Z}\rho_p(r)$) [2]. Although the liquid-drop model is compatible to a great degree with nuclei with N/Z ratio far from the valley of stability, it fails to account for phenomena taking place under extreme conditions, such as halo structures in nuclei with very large N/Z ratios like ^{11}Li and ^{14}Be ground states, where the wave function of the weakly bound valence neutrons extends far beyond the nuclear core [3]. Another example is the clustering that takes place in neutron-rich nuclei where the core of the nucleus consists of alpha clusters and the excess neutrons act as electrons in a molecule. In such a scenario, it is possible for several of these valence neutrons to escape and form a quasi-bound state [2]. Extending on this argument, consider a case where we have a proton-less nucleus. While the Coulomb term disappears entirely, the asymmetry term is massively enhanced which leads to a negative binding energy making the system unbound. Hence, the liquid-drop model does not predict the existence of a bound multineutron system.

In this context, the study of such proton-less nuclei has attracted considerable attention. Although no bound system composed solely of neutrons has been conclusively observed, its possible existence would have deep implications for our understanding of nuclear forces, and environments with extreme neutron

excess such as neutron stars. Motivated by these questions, experimental and theoretical efforts to identify multineutron systems date back to the early 1960s.

It is well established that a bound system of two neutrons (dineutron) does not exist in free space; however, strong dineutron correlations can take place in certain weakly bound nuclei, especially halo systems. The question is whether a bound or quasi-bound system of neutrons may exist beyond N=2 (Fig. 1.1). In this context, multiple theoretical studies have explored the possible existence of multineutron systems. The general conclusion of these calculations over the years is that no bound $3n$ or $4n$ system exists when realistic nucleon–nucleon interactions are used. In particular, if one attempts to artificially bind a tetraneutron system, the neutron–neutron potential V_{nn} must be scaled by an unrealistically large factor, which is not compatible with the known properties of nuclear forces [2]. If such systems cannot be bound, the next natural step is to investigate whether they could exist as unbound resonant states.

Starting from the late 70s, Glöckle et al. solved the Faddeev equations exactly in momentum space for the 3n system through several papers ([4],[5],[6], and [7]). Their results showed that the 2-body neutron-neutron interaction V_{nn} would need to be increased by a factor of about 3.7 to bind the trineutron [5], even when higher partial waves beyond the S-wave were included. In a further attempt to seek a possible resonance [6][7], they scaled only the waves beyond s-waves in order to bind the trineutron, and then decreased the scaling factor to zero. The overall conclusion of using these "exact" calculations was that no trineutron bound state exists, nor any resonance in the physical region.

This approach was later extended by Lazauskas and Carbonell, who investigated the evolution of bound states into the continuum for both trineutron and tetraneutron systems by introducing additional three-body or four-body forces acting on $3n$ and $4n$ systems respectively [8][9]. These artificial forces do not affect the subsystems and can be gradually removed without introducing spurious effects. Their results showed that neither trineutron nor tetraneutron systems can exist as bound states or as observable resonances.

Another approach to the tetraneutron problem was proposed by Pieper, who used a many-body model approach using Green Function Monte Carlo (GFMC) methods to study the possible existence of a bound tetraneutron state [10]. His findings confirmed that a bound tetraneutron state was not possible without distorting very negatively the results for all neighboring light nuclei. However, he suggested that a possible $4n$ resonance could exist at only about 2 MeV. For this, he computed the energy of a $4n$ bound state

confined within a Woods–Saxon potential with fixed diffuseness, and the radius of the trap was varied until the system became unbound. By extrapolating the last energy values to the limit where the external potential vanishes, a possible tetraneutron resonance was found at an energy of about 2 MeV, its width being probably very large. This method avoids the need for global scaling of the interaction, which would otherwise lead to strong deviations from well-established nuclear properties, such as the strong binding of dineutron or trineutron systems.

More recently, further calculations using many-body models with realistic interactions were performed ([11], [12], [13], and [14]). These calculations relied on binding the resonances which led to nonphysical systems containing strongly bound dineutrons or trineutrons.

Following these results, Hiyama et al. performed an extensive study focusing on the T=3/2 component of the three-body force acting in neutron-rich systems using exact calculations [15]. Their analysis led to the conclusion that neither trineutron nor tetraneutron systems can exist as bound states or as experimentally observable resonances. Finally, we mention that very recently, calculations were performed using the lattice effective field theory [16]. No narrow resonance near threshold was found in this work.

In parallel to these calculations, experimental investigations into the possible existence and properties of multineutron clusters have been implemented, which we briefly report below.

1.2 Brief history of multineutron experimental studies

The search for multineutron systems started in the 1960s with stable beam experiments producing multineutrons via activation reactions, using pion beams, or through transfer reactions, bringing essentially negative conclusions on the existence of multineutron states (see [17] for a detailed report). With the advent of the 21st century, the production of radioactive ion beams (RIBs) facilitated more in-depth studies of the multineutron systems. Several experiments were conducted to search for bound or quasi-bound systems of $3n$ and $4n$, mainly with RIBs and we briefly present their method and results.

1.2.1 GANIL: First RIB experiment

The study of multineutron systems took a significant step forward with the first experiment using radioactive ion beam providing data on the 4*n* system, conducted in 2001 at GANIL by M. Marquès et al. [18]. The main goal of the experiment was to study clustering in light nuclei near the particle emission threshold. One of the most promising candidates for such a system was ^{14}Be, which has a separation energy for four neutrons of 5 MeV [18].

For this experiment, a breakup reaction study was performed using a ^{14}Be beam at 35 MeV/u impinging on a thick carbon target. To handle the beam's energy spread of about 10%, time-of-flight (ToF) measurements were taken using two position-sensitive PPACs (Parallel Plate Avalanche Counters) placed 24 meters apart upstream of the target. The beam was identified on a particle-by-particle basis using a 300 μm-thick silicon detector placed after the second PPAC [19]. To detect the charged fragments from the breakup, a large-area position-sensitive Si-CsI telescope was set up at zero degrees, 11.4 meters downstream from the target. The CsI detectors in the telescope also served as a veto for high-energy light charged particles heading toward the neutron detectors as shown in Fig. 1.2 [19].

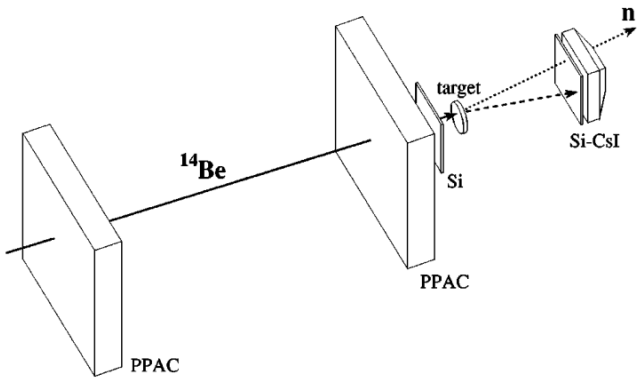


Figure 1.2: Experimental setup inside the vacuum chamber. From left to right: the beam tracking detectors, the target, and the telescope for the detection of charged fragments (see text) [18].

For neutron detection, the DEMON array, which consisted of 99 liquid scintillators capable of distinguishing neutrons from gamma rays or cosmic rays was used. The DEMON array covered a broad angular range, from $+13^\circ$ to -40° horizontally and $\pm 14^\circ$ vertically, with the modules arranged in a staggered configuration between 2.5 and 6.5 meters from the target [20][21].

Neutron identification relied on pulse-shape analysis. Only events in which a single DEMON module

fired in coincidence with a charged fragment were considered in the analysis, which helped avoid contamination from cross-talk [20]. This setup allowed the team to clearly differentiate neutrons from other particles, ensuring solid data on the breakup products.

In liquid scintillators, neutrons are indirectly detected. When a neutron of energy E_n enters a scintillator, it can undergo n-p scattering, transferring some of its energy to a proton, which is then detected where $(E_p \leq E_n)$. In many cases, the neutron can exit the detector. The deposited energy can be determined through calibration with sources and cosmic rays. By comparing the detected energy from the scintillator with the neutron energy (from ToF), the neutron's characteristics can be determined. In ideal conditions, the proton energy (E_p) should be less than or equal to the neutron energy (E_n), so the ratio (E_p/E_n) should typically be ≤ 1. However, due to the detector's resolution, this ratio can sometimes exceed 1. For the DEMON array, the upper limit of this ratio was ~ 1.4 [20][18].

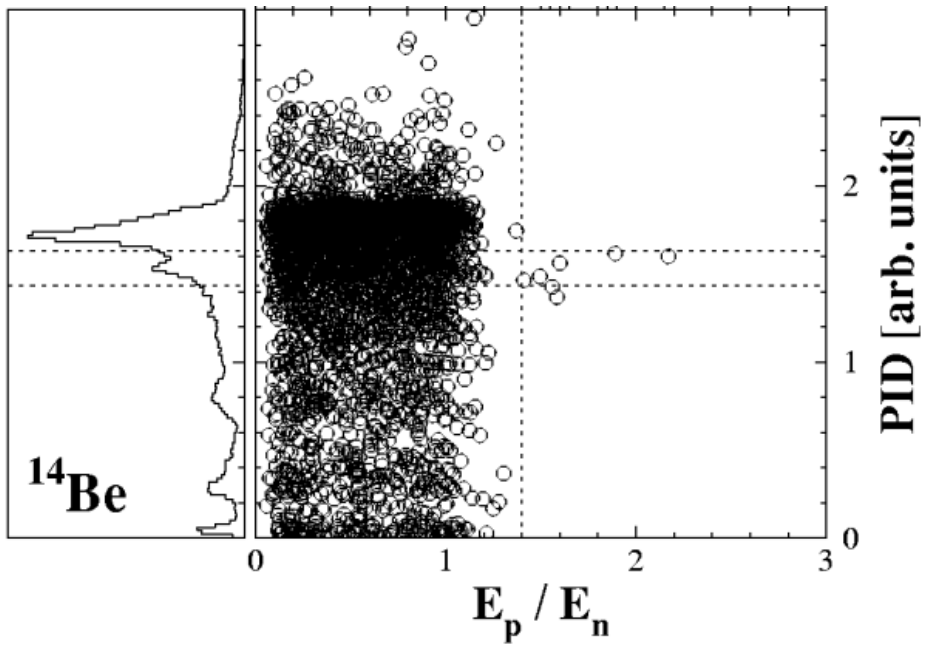


Figure 1.3: Scatter plot of the PID vs the (E_p/E_n) ratio for the data from the $(^{14}\text{Be}, X + n)$ reaction, with the PID projection shown on the left and horizontal dashed lines indicating ^{14}Be events within the PID and vertical dashed line indicating the threshold of 1.4 for multineutron detection [18].

If the (E_p/E_n) ratio exceeds 1.4, it can indicate the presence of a bound multineutron system [18]. Figure 1.3 shows the scatter plot of the PID vs the (E_p/E_n) ratio for the data from the $(^{14}\text{Be}, X + n)$ reaction, with the PID projection shown on the left. Horizontal dashed lines marked the ^{14}Be events within the PID, while a vertical dashed line indicated the threshold of 1.4 for multineutron detection.

The results show six events coincident with ^{14}Be had (E_p/E_n) ratios above the 1.4 threshold. This strongly suggested the presence of a multineutron system. Since dineutrons and trineutrons are unbound, these events were interpreted as tetraneutrons, marking an important observation in the ongoing search for multineutron systems [2]. Later on, the group performed further analysis and deduced that the six events could be compatible with the formation of a 4-neutron resonance with an energy of about 2 MeV (or less) above threshold [22].

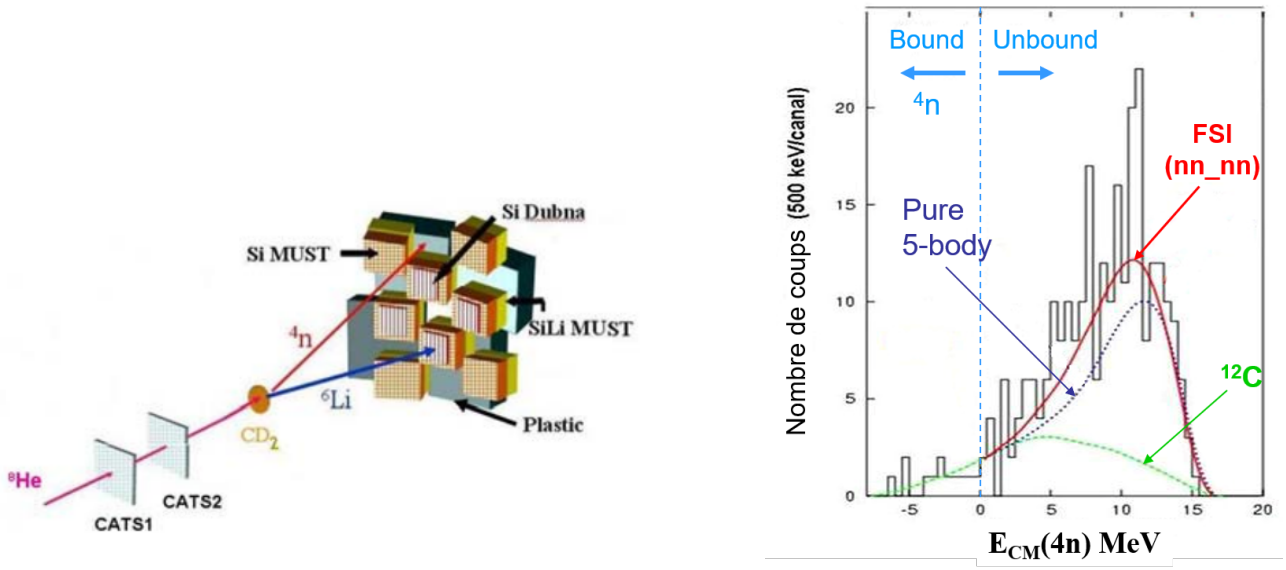


Figure 1.4: Experimental setup of the ^{8}He$(d,^6$Li$)4n$ experiment performed at GANIL (left) (figure from [23]). Excitation energy spectrum of the $4n$ system (right).

Motivated by the intriguing results obtained from the experiment of Marquès, another experiment was proposed at GANIL with a new approach aiming to obtain the missing mass spectrum of the $4n$ system using a high intensity ^{8}He beam and utilizing the MUST array [24]. The experiment was performed at GANIL using a beam of ^{8}He at 15 A.MeV impinging on a CD_2 target of about 1 mg/cm^2 thickness and the alpha-transfer reaction ^{8}He$(d,^6$Li$)4n$ was studied. The ^{6}Li particles' energy and angle were detected using the MUST array to which 65 μm-thin Silicon detectors were added. The neutrons were detected using thick plastic detectors placed at forward direction (experimental setup shown in Fig. 1.4 (left)). Excitation energy spectrum of the $4n$ system was deduced from the missing-mass using the energy and angle of ^{6}Li while the spectrum was gated by requiring at least one neutron to be detected in coincidence with the ^{6}Li. Events below the threshold of $\alpha + 4n$ were considered background originating from the ^{12}C in the CD_2 target. Figure 1.4 (right) shows the excitation energy of the $4n$ system with the ^{12}C induced

background in green dashed line, pure 5-body phase-space calculation in blue dashed line, and a simple $2n - 2n$ interaction simulation in the final state in red line. As shown in the figure, there is no indication of a bound $4n$ state. The experimental spectrum is well reproduced by the sum of the contribution of ^{12}C in the target and the $2n - 2n$ simulation except for a structure at around 11 MeV.

1.2.2 RIKEN: $4n$ experiment: Kisamori et al. (2016)

The study of multineutron systems continued to evolve with the suggestion from ab initio calculations incorporating realistic nuclear interactions that a broad resonance tetraneutron state could exist around 2 MeV above the threshold. This prediction is based on the extrapolation of the calculated energy with an external potential well [10]. In light of these theoretical predictions, an experiment was conducted by K. Kisamori et al. at the Radioactive Ion Beam Facility (RIBF) to explore the possibility of a resonant tetraneutron state using the double charge exchange (DCX) reaction ^{4}He(^{8}He,^{8} Be).

To carry out the DCX reaction, a primary ^{18}O beam at 230 MeV/u was directed onto a 20-mm-thick beryllium target. This interaction produced a secondary ^{8}He beam with an energy of 186 MeV/u and an intensity of 2×10^6 counts/s. The secondary beam was then focused and purified to a purity of 99.3%, with its momentum determined using the BigRIPS facility [25]. The purified ^{8}He beam was subsequently transported to a liquid helium target, placed at the SHARAQ spectrometer's focal point, with a thickness of 136 mg/cm^2.

The key reaction, ^{4}He(^{8}He,^{8} Be), took place when a ^{4}He nucleus in the target exchanged charge with the incoming ^{8}He beam. This resulted in the production of ^{8}Be, which then decayed into two alpha particles. The momenta of these alpha particles were precisely measured by the high-resolution SHARAQ spectrometer [26].

To determine the missing mass energy of the 4n system, the experiment calculated it on an event-by-event basis using the momenta of the beam and the two alpha particles produced from the decay of ^{8}Be [25]. The results are shown in Fig. 1.5, which presents the missing mass energy of the tetraneutrons, E_{4n}, covering the energy range of $-25 < E_{4n} < 65$ MeV, with the overall missing mass resolution determined to be 1.2 MeV in sigma [25]. In this plot, $E_{4n} = 0$ corresponds to the threshold of four-neutron decay.

Within the low statistics, the data show a peak of four counts in the low energy region $0 < E_{4n} < 2$ MeV

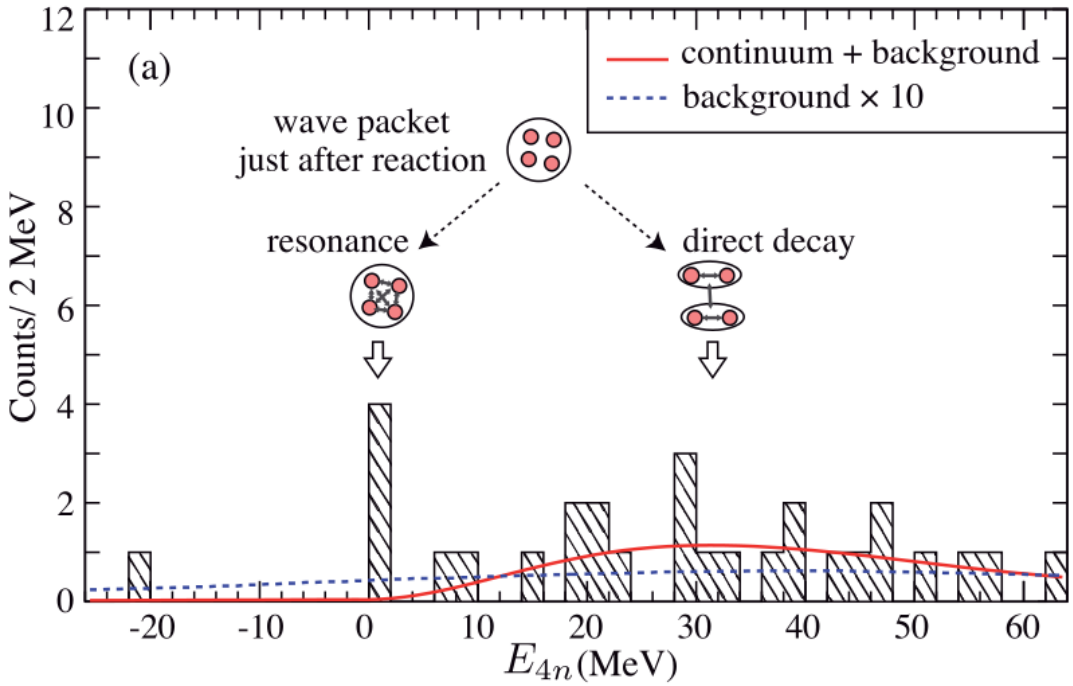


Figure 1.5: Missing-mass spectrum of the tetraneutron system. The solid (red) curve represents the sum of the direct decay of correlated two-neutron pairs and the estimated background. The dashed (blue) curve represents the estimated background multiplied by a factor of 10 [25].

at 0.8 ± 1.4 MeV with an upper limit on the width of 2.6 MeV, along with a continuum in the higher energy region, $E_{4n} > 2$ MeV. The significance of this peak was found to be 4.9σ. These two distinct features were interpreted as representing two different states: the first, a resonant state of the tetraneutron system, and the second, a direct decay process involving final-state interactions between two correlated neutron pairs, contributing to the observed continuum [25].

1.2.3 RIKEN 4n experiment: Duer et. al. (2022)

The most significant experiment for the $4n$ was the experiment performed by M. Duer and her team at RIKEN using the SAMURAI spectrometer. The experiment aimed to populate possible tetraneutron states using the quasi-elastic knockout reaction of an alpha particle from a high-energy ^{8}He projectile using a proton target and obtain a tetraneutron missing mass spectrum with good statistics and low background. The knockout reaction $^{8}\mathrm{He}(p, p\alpha)$ was performed in inverse-kinematics with large momentum transfer as it can knockout the alpha core in the ^{8}He (Fig. 1.6). Due to its cluster structure, the state of remaining four valence neutrons sharing a center-of-mass motion may have a large overlap with a tetraneutron state [28]

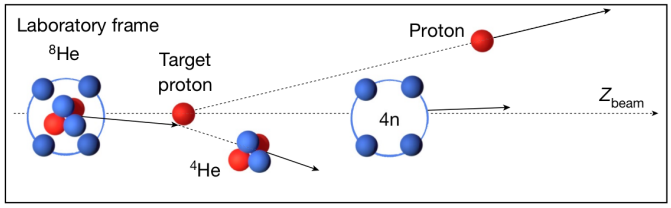


Figure 1.6: Quasi-elastic scattering of the ^{4}He core from a ^{8}He projectile off a proton target in the laboratory frame. The length of the arrows represents the momentum per nucleon (the velocity) of the incoming and outgoing particles. Z_{beam} is the beam axis [27].

[29].

A primary beam of ^{18}O was directed at a beryllium production target to produce a secondary beam of ^{8}He at 156 MeV/u which then impinges on a 5-mm-thick liquid hydrogen target. Inside the reaction chamber and downstream from the target, three planes of silicon-strip detectors, where each plane consists of two orthogonal layers enabling position measurements in both horizontal and vertical directions, served for tracking, energy-loss measurement and reconstruction of the reaction vertex [27]. Downstream from the reaction chamber, the recoil proton and knockout alpha were separated using the SAMURAI magnet with a nominal magnetic field of 1.25 T, afterwards, a drift chamber was used to track the proton and alpha after the magnet, which could then be identified using two scintillator walls located beyond the drift chamber and used to detect the energy-loss and time-of-flight [27]. A schematic overview of the setup at SAMURAI can be seen in Fig. 1.7.

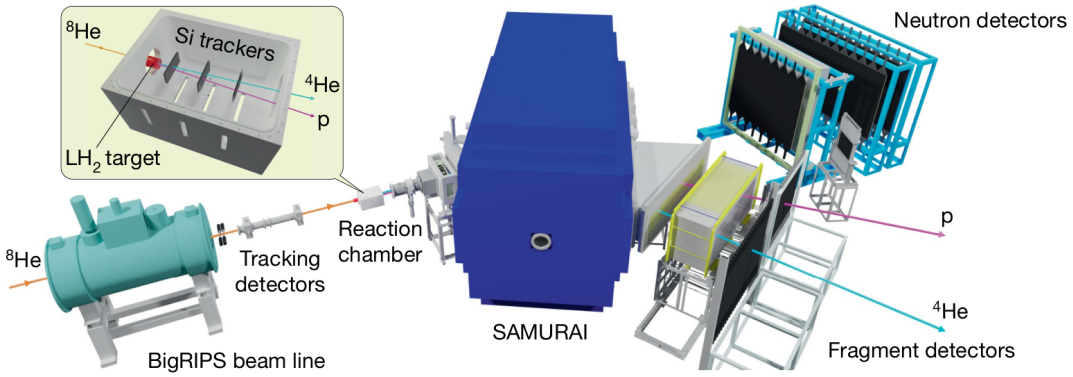


Figure 1.7: Schematic overview of the setup [27].

Selection of the proper events was done in an event-by-event basis through identifying the beam and the proton and alpha of the knockout from the detectors after the SAMURAI magnet. Afterwards, the missing

mass energy of the $4n$ system was calculated using

$$E_{4n} = \sqrt{E_{miss}^2 - \boldsymbol{P}_{miss}^2} - 4m_n \tag{1.2}$$

where E_{miss} and $\boldsymbol{P}_{miss}$ are the energy and momentum of components of the missing momentum four-vector of the $4n$ and m_n is the neutron mass. Figure 1.8 show the missing mass spectrum of the $4n$

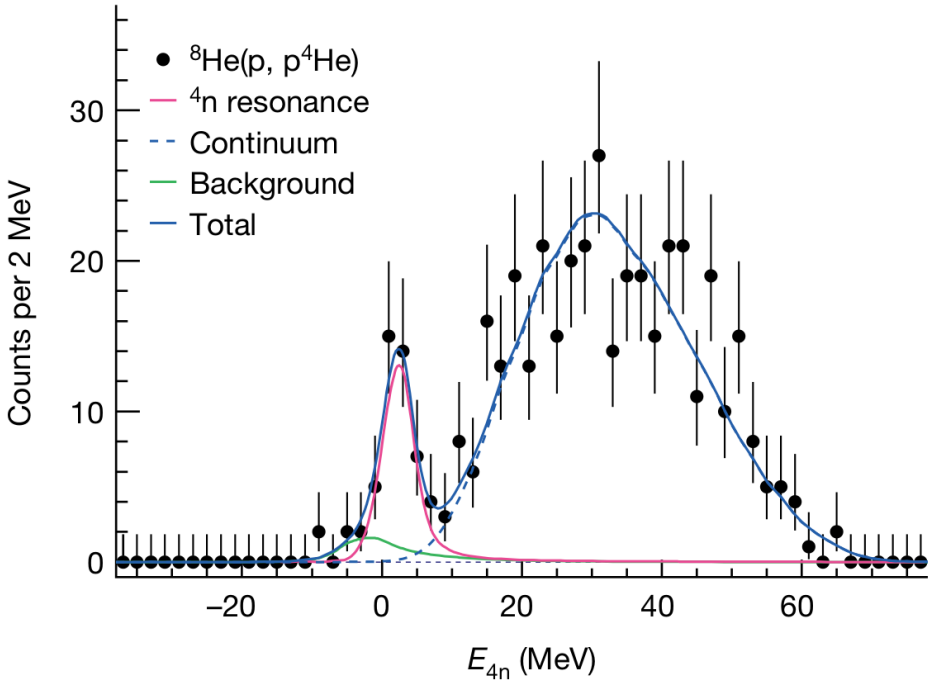


Figure 1.8: Missing mass spectrum of the tetraneutron system extracted from the ^{8}He$(p, p\alpha)$ reaction. The different curves represent a Breit–Wigner resonance (pink), a non-resonant continuum (dashed blue), the background from two step processes (green) and the total sum (solid blue) [27].

system fit with a Breit-Wigner resonance fit for the resonance and continuum. For the first time in multineutron studies, a very significant signal was observed. Namely, a clear resonance-like structure with significant statistics and low background was found at $E_r = 2.37 \pm 0.38(\text{stat.}) \pm 0.44(\text{sys.})$ MeV with a width $\Gamma = 1.750 \pm 0.22(\text{stat.}) \pm 0.30(\text{sys.})$ MeV, which was followed by a broad non-resonant continuum. This result is compatible with a tetraneutron state that is unbound with a lifetime of $(3.8 \pm 0.8) \times 10^{-22}$s [27].

Following the publication of these results, the interpretation of the peak at 2.37 MeV which could be a tetraneutron resonance, Lazauskas et al. performed a calculation which interpreted the peak as a consequence of dineutron-dineutron correlations [30] and it was able to reproduce the data from the

experiment by Duer to a great extent.

1.2.4 RIKEN: 3n experiment

The exploration of multineutron systems advanced further with the RIKEN Nishina Center's Radioactive Ion Beam Facility (RIBF) [31] due to its high capabilities in production of radioactive ion beams. Building upon the insights gained from earlier experiments at GANIL, K. Miki and his team investigated the possible existence of 3-neutron ($3n$) resonances, particularly the resonance at 1.29 MeV, which had been suggested by theoretical calculations based on the no-core Gamow shell model [14].

The experiment was split into two parts, focusing on both 3-proton (3p) and 3-neutron (3n) systems. Although the ^{3}He(^{3}He, t)$3p$ experiment was not performed at RIKEN, the analysis of both experiments was done conjointly. The focus in this section will be on the 3n results. The 3n part was carried out at the SHARAQ spectrometer [26]. A primary beam of ^{4}He at 200 MeV/u was directed onto a 6-cm-thick ^{9}Be target, producing a secondary triton beam at 170 MeV/u. This beam was purified and separated using the BigRIPS fragment separator [32] before being transported to a secondary target placed at the pivot point of the SHARAQ spectrometer [33]. The secondary beam, which had a high intensity of 5×10^7 pps and a purity of 99%, was then used for the ^{3}H(t,^{3} He)$3n$ on the triton target.

For this experiment, a newly developed radioactive tritium target made from self-supporting Ti-^{3}H was tested and employed during the experiment [34]. This target was prepared from an 80-μm-thick titanium foil with a tritium loading ratio of ^{3}H/Ti = 1.5, giving a tritium thickness of 3 mg/cm^2. The stored activity in this target was 1.6 TBq, making it the thickest Ti-^{3}H target ever created at the time.

The ^{3}H(t,^{3} He)$3n$ reaction was investigated by analyzing the emitted ^{3}He particles using the SHARAQ spectrometer. The spectrometer provided an excitation energy resolution of 1 MeV (FWHM) and an angular resolution of 0.7° (FWHM) [33]. The data collected were used to measure the double-differential cross section in the lab frame as a function of excitation energies in the 3n and 3p systems at each momentum transfer $q_{c.m}$ as shown in Fig. 1.9 (left). The zero of each excitation energy corresponded to the total mass of three free nucleons, with the red and blue histograms representing the missing mass spectra for the ^{3}H(t,^{3} He)$3n$ and ^{3}He(^{3}He, t)$3p$ reactions, respectively [33]. Interestingly, no peak-like structures were observed in the excitation energy spectra for either the 3n or 3p reactions in the region between 0–20 MeV.

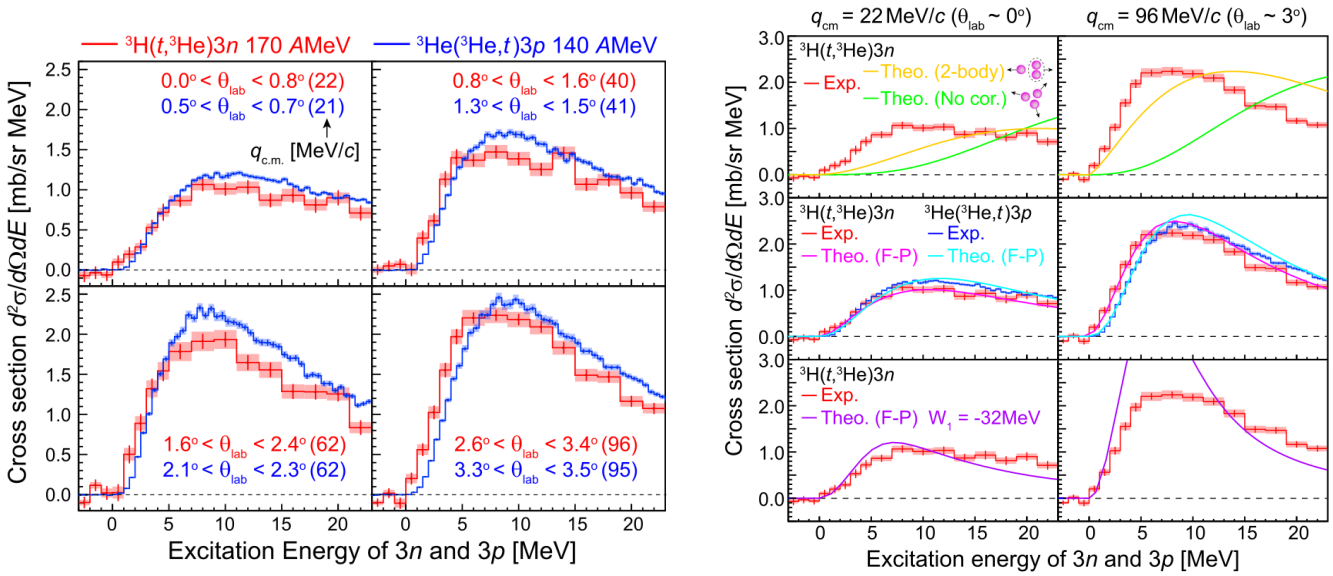


Figure 1.9: Double-differential cross-section spectra for the ^{3}H(t,^{3} He)3n (red) and ^{3}He(^{3}He, t)3p (blue) reactions. The error bars and shaded regions represent the statistical and systematic uncertainties, respectively. The numbers in parentheses represent the average momentum transfers $q_{c.m.}$ [MeV/c] (left). Comparison of the theoretical calculations with the experimental data (right). The theoretical calculations are the quasi-free calculations (top), and the F-P calculations without (middle) and with (bottom) a phenomenological 3NF [33].

This absence of peaks suggests that one of the nucleons in the three-nucleon system does not exhibit a strong correlation with the other two correlated neutrons [33]. To further interpret the data, the results were compared to both quasi-free formalism, which describes the phase-space distributions of the 3n or 3p systems in the final states [35], and Faddeev-PWIA (F-P) calculations [36]. These calculations, which do not predict any 3n resonance poles in the observable regions, were found to reproduce the overall E_x distributions of the experimental cross sections (Fig. 1.9 (right)), supporting the conclusion that no 3n resonance exists within the current dataset.

Recent work by S. W. Huang et al. (To be published in Phys. Rev. Res. soon) discussed the ^{8}He(p,pn) reaction experiment performed at SAMURAI using a secondary beam of ^{8}He at 156 MeV/u with intensity $\sim 10^5$ pps impinging on the 15-mm-thick liquid hydrogen target of MINOS [37]. The secondary beam was tracked with the help of two drift chambers while the recoil protons from the (p, pn) reaction were tracked using a cylindrical time projection chamber surrounding the target with approximately $20° - 60°$ angular coverage [38]. The reaction populates ^{7}He* which can decay to ^{4,6}He. These charged fragments are then momentum analyzed using the SAMURAI spectrometer [39][40]. The neutrons with the forward-going momenta were determined by their ToF using the NeuLAND [41] and NEBULA [42] plastic scintillator

arrays. The analysis was done using the invariant-mass method and they were able to directly measure the $3n$ emission from ^{7}He for the first time. A prominent resonance-like structure above the threshold of ^{4}He + $3n$ was found at 2.08(4) MeV with a width of 3.9(2) MeV. Using state-of-the-art structure model calculations, the peak-like structure was attributed to the predicted $3/2^-_2$ state of ^{7}He with a possible small admixture from $5/2^-_1$ excited state. A broad structure at 1 MeV was observed in the $3n$ invariant-mass spectrum and it was very well reproduced by the sequential decay of ^{7}He* via ^{6}He$^{*}(2^+_1)$ using simulations incorporating $n-n$ correlations. Hence, no evidence of any significant three-neutron correlations including trineutron resonance was found.

1.2.5 Stable beam experiment

An experiment was performed using a stable beam, taking advantage of its many orders of magnitude higher intensity compared to radioactive ion beams (RIBs), as well as its better-defined momentum [43]. The aim was to study the three-proton pickup reaction ^{7}Li(^{7}Li,^{10}C)$4n$, using a $^{7}Li^{3+}$ beam at 46 MeV delivered by the MP Tandem accelerator in Garching.

The beam impinged on a target consisting of nominally 100 μg/cm^2 thick layers of 99% enriched ^{7}LiO, deposited on 20 μg/cm^2 carbon foils. The ^{10}C ejectiles were momentum analyzed at a scattering angle of 7.0° in the Q3D magnetic spectrograph [44, 45]. At the focal plane, a combined detection system described at [46, 47] was employed, consisting of a single-wire proportional counter for energy-loss and position determination, together with an array of 96 PIN silicon detectors (each 10 mm wide and 30 mm high), providing the residual energy and additional position information [43].

In the angular range $6° - 9.5°$, a clear peak was observed in the ^{7}Li(^{7}Li,^{10}C)$4n$ reaction, corresponding to an excitation energy of 2.93(16) MeV in the final system. This structure was interpreted as possibly due to for a bound tetraneutron state, with a binding energy of BE = +0.42(16) MeV, in agreement with previous theoretical and experimental indications [18, 25]. This was considered a weak indication of the possible existence of a bound tetraneutron system.

1.3 Beyond the 4*n* system

As mentioned above, no conclusive results were obtained regarding the existence of a tetraneutron system. Besides, as mentioned before, adding more neutrons seems to increase the stability of the nucleon system which can motivate the search for hexaneutrons. Another possible hint for the 6-neutron is the analogous case of liquid $(^3\mathrm{He})_\mathrm{N}$ in atomic physics. As in the case of neutrons, ^{3}He atoms are fermions and their attractive interactions are too weak to form a dimer. Furthermore, although they differ in scale, the interaction potential shape of the He-He interaction is very similar to that of the n-n case as illustrated in Fig. 1.10 [2].

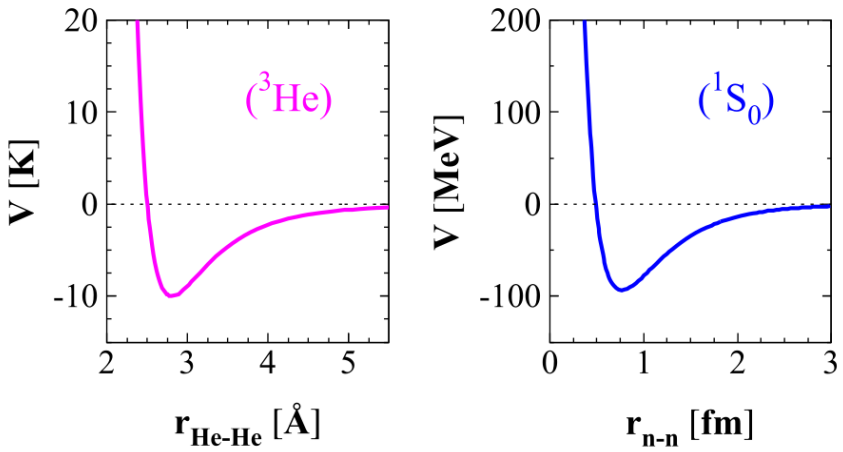


Figure 1.10: Comparison between the ^{3}He inter-atomic potential and the n-n potential in the singlet state [2].

Therefore, considering that a very high number of ^{3}He atoms (N~ 30) form a liquid drop [48], perhaps there could be a critical number of neutrons beyond which a bound or quasi-bound state can exist.

Finally, we note that on the theoretical side, predictions based on a cluster approach derived from shell-structure in the framework of the so-called Isomorphic Shell Model were reported in [49]. Interestingly, it was found that 6*n* is a more favorable candidate for stability or as a low-lying resonance than 4*n*, while the dineutron remains unbound. However, it can be noticed that this model contains semi-classical approximations and does not use realistic interactions.

1.4 Our approach to study 6-neutron system

In this work, the investigation of hexaneutrons was done using the quasi-free scattering reaction $^{14}\mathrm{Be}(p, p\alpha)^{10}\mathrm{He}^{*}$ where the ^{14}Be beam of energy $\sim$ 150 MeV/u impinged on a solid hydrogen target of thickness 2mm. The reaction populated resonances in ^{10}He which can then decay through several channels such as ^{8}He + 2n, ^{6}He + 4n, and ^{4}He + 6n above the corresponding thresholds. The 6n spectrum was constructed using missing mass by obtaining information about the energy and angle of the recoil proton, knocked-out alpha, as well as the decay alphas. Although the missing mass method cannot obtain direct information about neutron correlations as it does not rely on detecting the 6n directly, it enables the determination of the 6n energy spectrum without the need to detect six correlated neutrons which is, as mentioned above, an extremely difficult task.

In the subsequent section, a detailed explanation of the experimental setup will be discussed.

Chapter 2

Experimental setup

This chapter will be a detailed description of the setup used for the SAMURAI12 experiment performed at the RIKEN Nishina Center **R**adioactive **I**on **B**eam **F**actory (RIBF) facility [50].

2.1 Overview

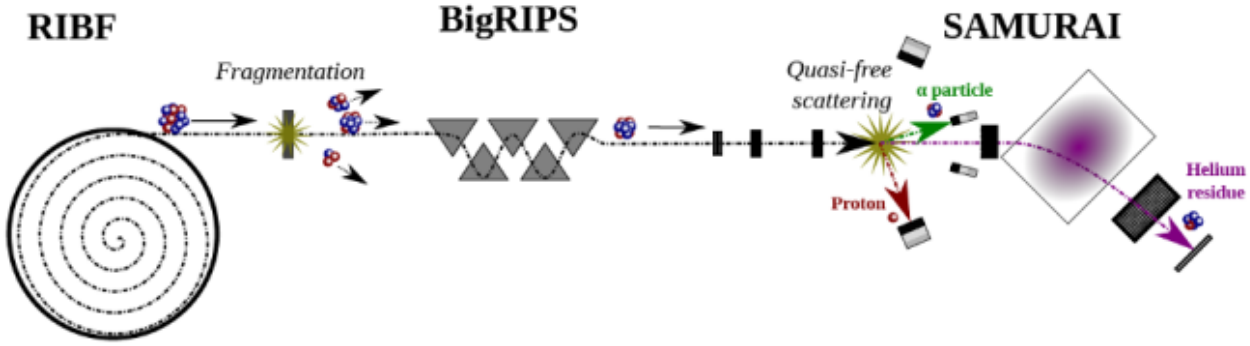


Figure 2.1: A schematic view of SAMURAI12 quasi-free scattering experiment at RIBF facility [51].

The **R**adioactive **I**on **B**eam **F**actory (RIBF) is a facility with the capability to generate high-energy radioactive ion beams of a myriad of nuclei with high purity and good selection. The SAMURAI12 experiment was performed using the SAMURAI spectrometer [52]. Figure 2.1 shows the overview of the experimental setup. During the SAMURAI12 experiment, a 230 MeV/u primary beam of ^{18}O was used on a thick Be target, where a fragmentation reaction generated secondary beams of ^{10,12,14}Be at approximately

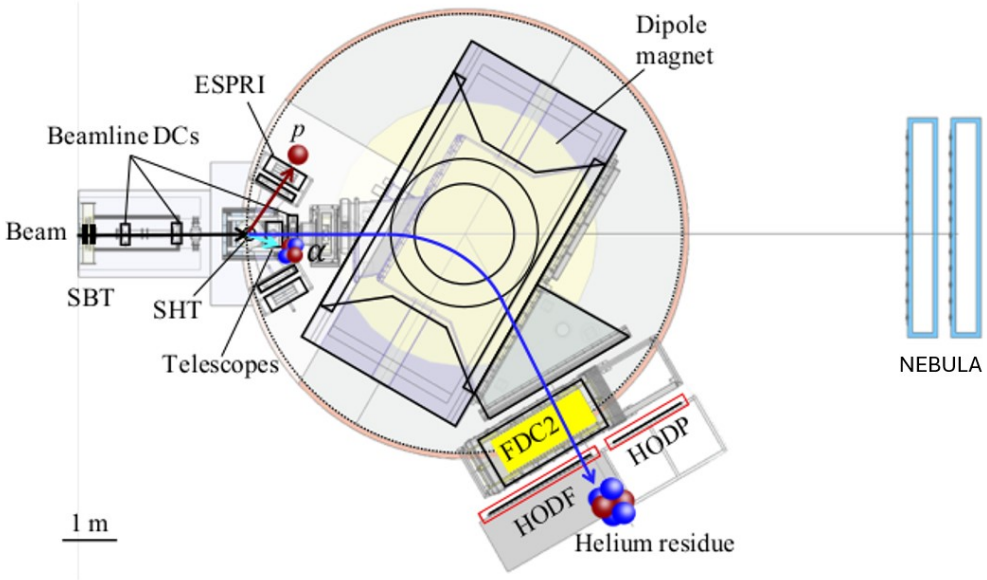


Figure 2.2: Schematic of SAMURAI12 experimental setup [51].

150 MeV/u. The secondary beams were selected and purified by the BigRIPS fragment separator [52]. The secondary beam was then transported to the SAMURAI large acceptance spectrometer to interact with a **S**olid **H**ydrogen **T**arget (SHT) [53], where the (p,pα) reaction took place. As shown in Fig. 2.2, the particles and residue produced in the reaction are detected by a series of different types of detectors to measure their energy and scattering angle. Description of these detectors will be provided in the following sections.

The main goals of the present work are to study the excitation energy of ^{10}He populated states by the quasi-free reaction $^{14}\mathrm{Be}(p, p\alpha)^{10}\mathrm{He}^{*}$ in inverse kinematics as well as the excitation energy of the 6-neutron system obtained from the decay of ^{10}He into an alpha and six neutrons. The missing mass method was utilized to obtain the excitation energy of the 6-neutron system given that the efficiency of measuring six correlated neutrons is extremely low. The method depends on accurately measuring the energy and trajectory (incident and scattering) angles of the beam as well as the products of the $(p, p\alpha)$ reaction, then deducing the energy of the remaining components of the reaction through the conservation of energy and momentum. Initially, the secondary beam is prepared using a series of accelerators, magnets, degraders, and slits to obtain optimal purity and accurate energy determination. The energy of the beam is determined using the two plastic scintillators located at F7 and F13 in order to measure the energy loss

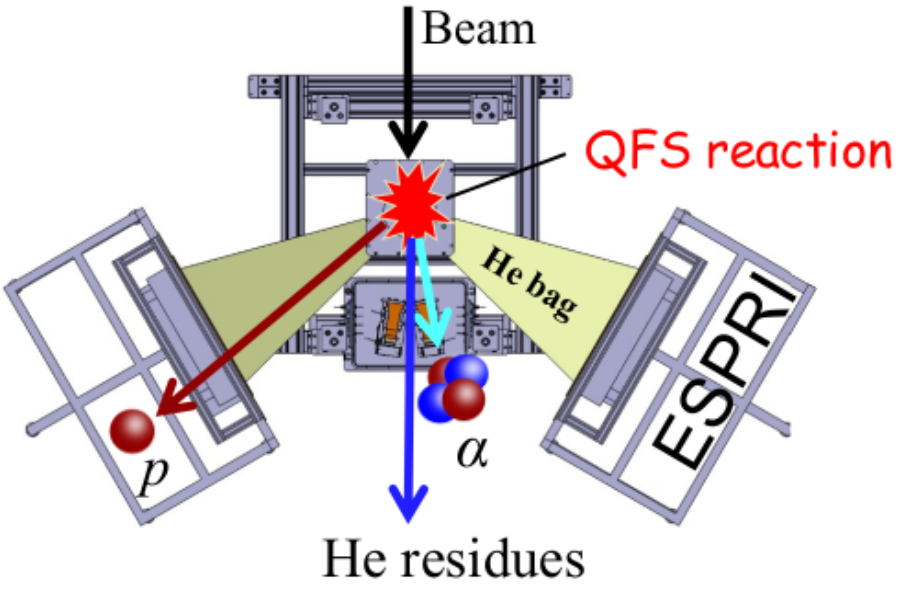


Figure 2.3: Schematic view of ESPRI and Telescope around SHT during $(p, p\alpha)$ reaction [51].

and time-of-flight (ToF) of the beam. The energy of the beam can subsequently be determined using the energy loss - time-of-flight ($\Delta E - ToF$) method, and the spread of energy can be determined. Afterward, the incident beam trajectory can be measured using two identical drift chambers (BDC1, BDC2) placed approximately 1 meter apart upstream of the target. The reaction takes place in a 2-mm-thick SHT with a diameter of 30mm.

Figure 2.3 shows a schematic of the $(p, p\alpha)$ reaction in the **E**lastic **S**cattering of **P**rotons by **R**adioactive **I**on beams (ESPRI) and Telescope systems. The recoil protons are detected using the ESPRI recoil protons spectrometer, which consists of two arms covering the lab system angular range of $50° - 70°$, corresponding to $40° - 70°$ in the center of mass (CM) system. Each arm contains a multi-wire drift chamber (MWDC) from which the trajectory, hence, the scattering angle of the recoil protons can be calculated, plastic scintillators to measure energy loss and time-of-flight of the protons, and NaI(Tl) scintillation detectors to measure the full energy of the protons. This allows the particle identification to be determined using $(\Delta E - E)$ or $(\Delta E - ToF)$ methods. In a similar manner, the knock-out cluster (alpha) detection system (Telescope) is comprised of two arms covering $4° - 12°$ angular range. Telescope consists of two stages. The first stage comprises a double-sided silicon strip detector (DSSD) that measure both the energy loss and the trajectory of the alpha particles, while the second stage contains CsI(Tl) scintillation detectors for

measuring the remaining energy of the fragments. This enables the measurement of the scattering angles in addition to the energy of the alpha using the $(\Delta E - E)$ technique.

Afterward, the trajectory of the ^{6,8,10}He residues obtained from the ^{10,12,14}Be$(p, p\alpha)$ reactions are detected using the **F**orward **D**rift **C**hamber (FDC0), which is placed approximately 1.2 m upstream from the SAMURAI magnet entrance. When different residue nuclei reach the magnet, they are deflected with different magnetic rigidity $(B\rho)$ values according to their mass, momentum, and charge, following the formula $(B\rho = \frac{p}{q})$. After the magnet, neutrons that pass through its gap are detected by two walls of plastic scintillators, called the NEBULA array. Meanwhile, the trajectories of the fragments, which are necessary for the rigidity calculation, are detected by the second forward drift chamber (FDC2). To perform particle identification beyond the magnet, two arrays of plastic scintillators, called HODP and HODF, are used to measure energy loss and time-of-flight.

2.2 Beam

The **R**adioactive **I**on **B**eam **F**actory (RIBF) of the RIKEN Nishina Center is a state-of-the-art facility capable of producing high-energy radioactive ion beams with energies up to 440 MeV/nucleon for light ions and 350 MeV/nucleon for very heavy ions [50].

2.2.1 Primary beam

The RIBF facility can accelerate a large number of nuclei with different energies. It is comprised of different types of injectors and cyclotrons (RILAC, RRC, AVF, fRC, IRC, and SRC) [50], each covering a certain range of nuclei and energies [31]. These cyclotrons and injectors have different operation modes depending on the species of the desired nucleus, its energy, and the frequency needed. There are three modes available, each defined by a different combination of stages and techniques; the SAMURAI12 experiment employed mode (3) (Fig. 2.4). This mode starts with an ECR ion source injecting ^{18}O atoms to AVF which accelerates the ^{18}O to 3.8 MeV/nucleon, which is followed by a stripper that completely removes the electrons from these ^{18}O atoms. Afterward, the particles are moved to the RRC, which can accelerate them up to 100 MeV/nucleon. Finally, the SRC accelerates the nuclei to energies up to 230

MeV/nucleon.

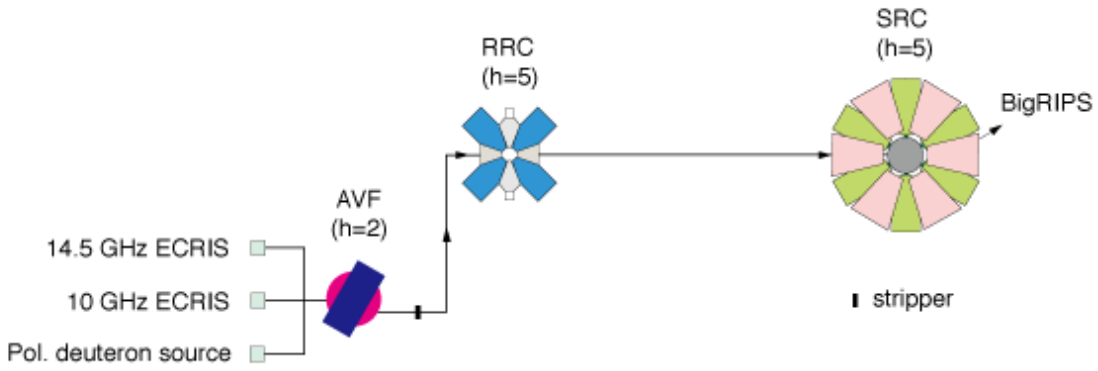


Figure 2.4: RIBF accelerator mode AVF+RRC+SRC [51].

2.2.2 Secondary beam (BigRIPS)

The secondary beam is produced by the in-flight beam separator BigRIPS [54]. It consists of a series of slits, quadrupole magnets, dipole magnets, and detectors. There are 7 focal points that define the BigRIPS RI beam separator, numbered F0-F7. Within this context, F0-F2 comprises the first stage which is responsible for secondary beam production and separation, while F3-F7 comprises the second stage which performs the ion identification on an event-by-event basis.

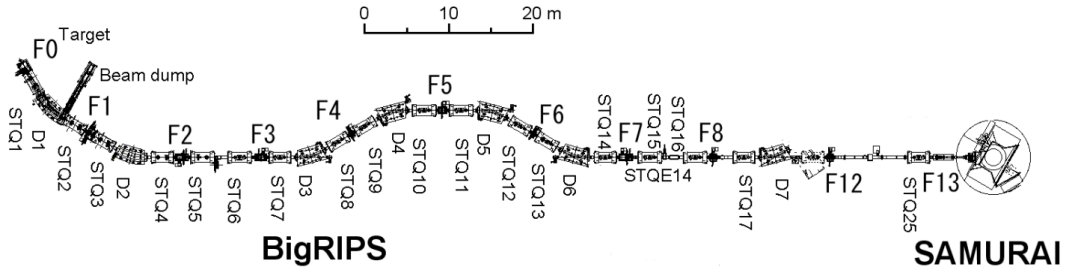


Figure 2.5: Schematic overview of BigRIPS for SAMURAI spectrometer.

Starting at F0, the interaction between the primary beam and a production target occurs, producing the secondary beam of ions of interest along with multiple other nuclear species. Subsequently, in the order shown in Fig. 2.5, the beam is then separated from some of the impurities using a series of 4 superconducting quadrupole triples (STQ) aligned from STQ1 to STQ4, two room temperature dipoles (RTD) with bending angle of 30° (D1-D2), and an achromatic wedge-shaped degrader placed at F1 to make

isotopic separation based on the momentum achromat technique. A high-power beam dump is placed near D1 to stop heavy ions of the primary beam, in addition to a thick block of concrete weighing 10,000 tons to shield from neutron radiation produced by the target and beam dump [39]. After the achromatic point F2, both STQ5 and STQ6 are placed to transport the separated RI beam by forming a telescopic system. Starting from F3, the second stage contains 8 STQs from STQ7 until STQ14, and 4 RTDs with a bending angle of 30° (D3-D6) comprising a four-bend achromatic spectrometer while F4, F5, and F6 are momentum-dispersive. The final focus F7 is doubly achromatic. The parameters of BigRIPS are shown in Table 2.1.

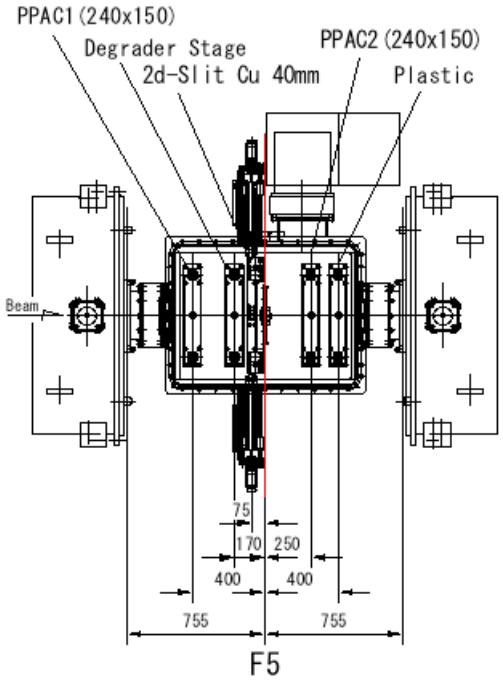


Figure 2.6: Schematic representation of detectors at F5 focal point (figure from [31]).

As many impurities in the RI beam exist at the first stage, the second stage of BigRIPS contains multiple parallel-plate avalanche counters (PPACs) and plastic scintillators to be able to measure the position, energy loss, and timing (e.g. see Fig. 2.6) of different species of particles in the beam and identify them using the $\Delta E - ToF$ method (determining A/q and Z) to adjust the slits and magnets selecting $B\rho$ values corresponding to the nucleus of interest (^{10,12,14}Be in our case).

The RI beam tagged by the second stage detectors is then transported to one of the three experimental halls ZeroDegree, SHARAQ, or SAMURAI spectrometers, as shown in Fig. 2.7. The SAMURAI

spectrometer starts at F13, and the optics for the secondary beam are tuned to position the beam on the SHT.

Table 2.1: BigRIPS parameters

Separator config	Tandem
First stage	STQ1-D1-STQ2-STQ3-D2-STQ4
Second stage	STQ5-D3-STQ6-STQ7-D4-STQ8-STQ9-D5-STQ10-STQ11-D6-STQ12
Degrader type	Wedge @F1, F4, F5, F6
Magnet type	Normal conducting Dipole and Superconducting Quadrupole
Angular acceptance	80 mrad horizontal and 100 mrad vertical
Momentum acceptance	6 %
Maximum rigidity	9 Tm
Total path length	F0-F7: 78 m
Momentum dispersion	-2.31 cm/% for first stage and 3.3 cm/% for second stage
Momentum resolution	1290 for first stage and 3300 for second stage (dX=1mm)
Focal plane	(F1,F4,F5,F6) are momentum dispersive, (F2,F3) are achromatic, F7 is doubly achromatic

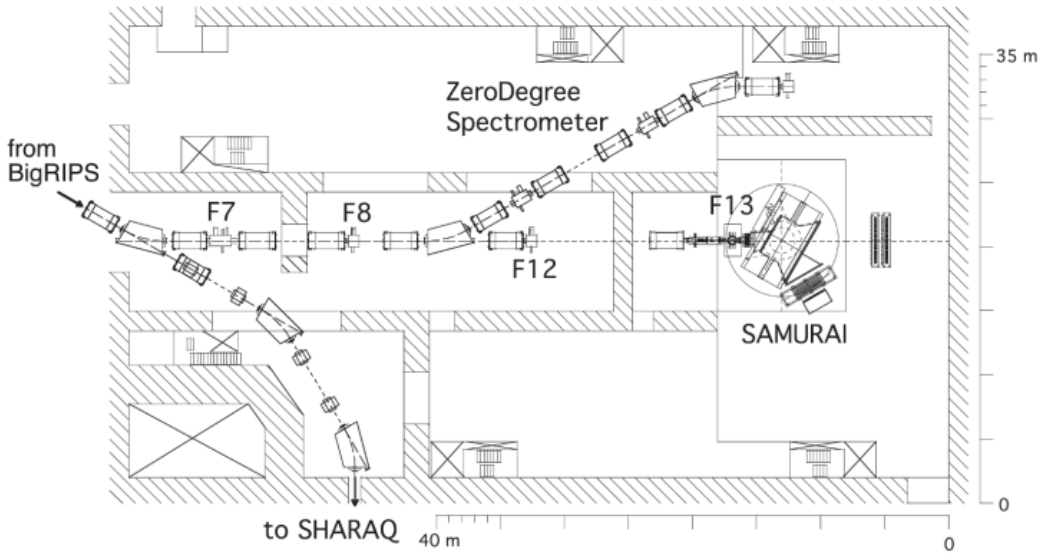


Figure 2.7: Schematic view of branching beamlines of BigRIPS (figure from [31]).

2.3 Beamline detectors

In order to accurately characterize the beam incident on the target for the experiment, a series of plastic scintillators and drift chambers were used to detect beam energy loss, time-of-flight, and position.

2.3.1 Beamline plastics

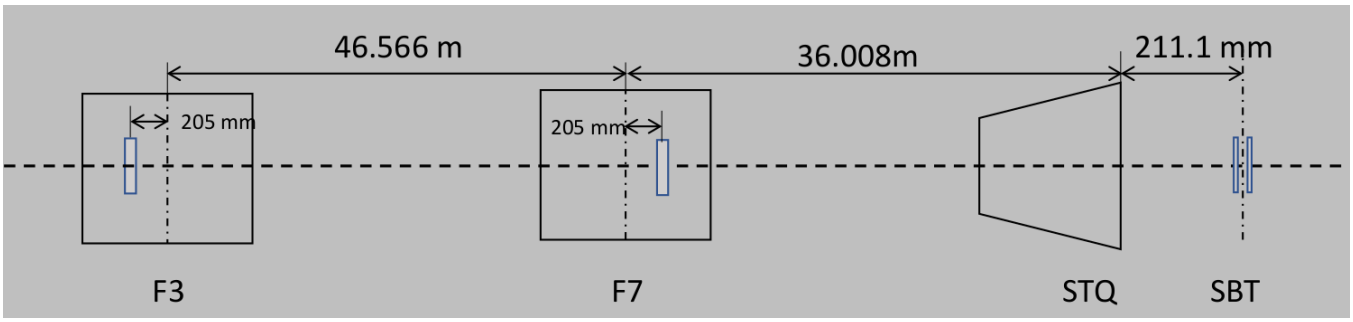


Figure 2.8: Distances between beamline plastics at focal points F3,F7, and F13.

The time-of-flight and energy loss information of the secondary beam measured by the plastics at different focal points of the BigRIPS beamline is used to determine the beam energy by ToF and PID using the $\Delta E - ToF$ method. This was achieved by two photomultiplier tubes (PMTs) coupled to both ends of each plastic scintillator, with the average signal from both PMTs used to determine time or energy. At F13, located downstream of STQ25, there are two plastic scintillators, SBT1 and SBT2, comprising the SBT detectors. The average signal from these plastics was used both as a beam trigger and as the start signal for the time-of-flight measurements. Figure 2.8 illustrates the relative distances between the plastics placed at focal points F3, F7, and F13, respectively.

2.3.2 Beamline Drift chambers

The **B**eamline **D**rift **C**hambers BDC1 and BDC2, which were used to determine the beam trajectory and reconstruct the position of the beam on target on an event-by-event basis, were positioned approximately 1 m apart. Precisely, BDC2 was placed 1.4 m upstream from the SHT. Both drift chambers are identical, and each one is composed of 8 layers spaced 4.8 mm apart, with each layer containing 16 wires placed 5 mm apart. They follow the configuration XX'YY'XX'YY' with every two adjacent layers shifted by 2.5 mm to improve spatial resolution. The effective area of each BDC is 80×80 mm^2, and the detailed parameter of the BDC can be seen in Table 2.2, while a schematic of the BDC can be seen in Fig. 2.9.

The ionization gas in the BDC is isobutane (C_4H_{10}) at 50 Torr. This gas is ionized when the beam particles pass through it. Under the effect of the electric field inside the drift chamber, the electrons drift towards the anode while the ions drift towards the cathode. This process produces electrical signals in the

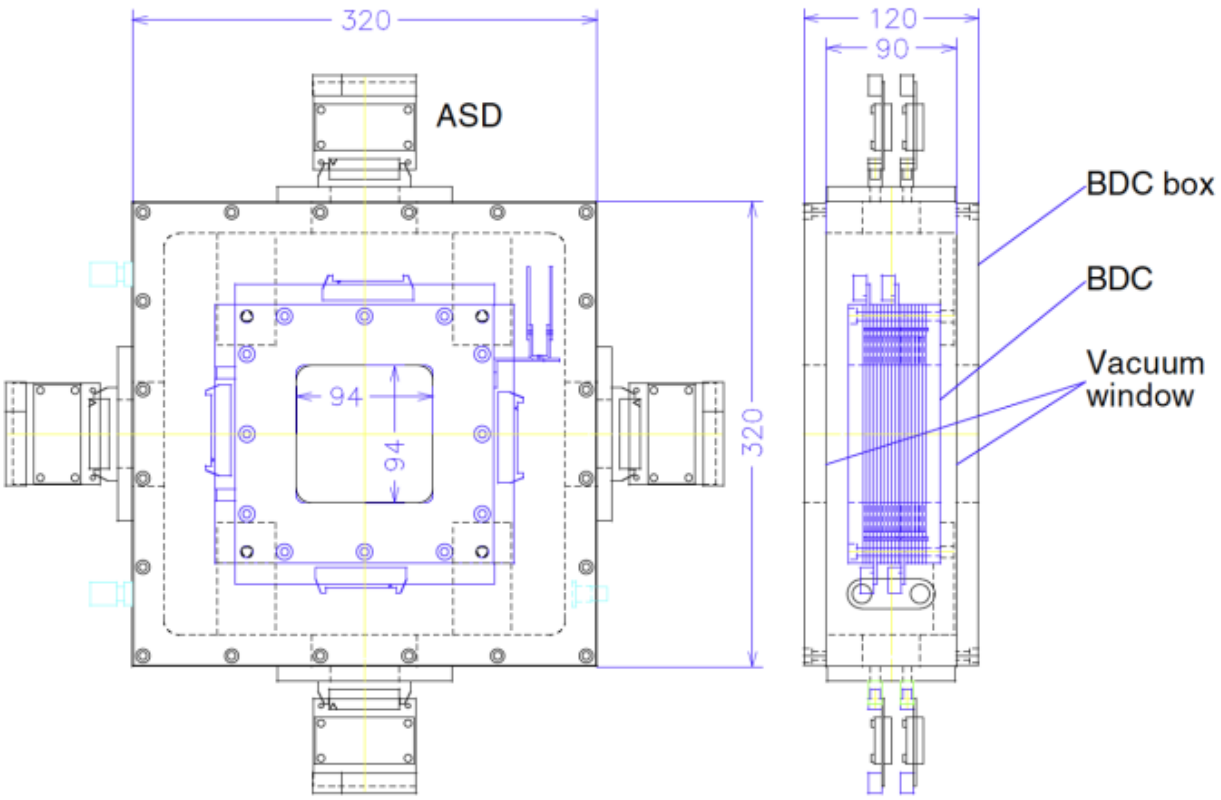


Figure 2.9: BDC schematic view [Front view(Left), Top view(right)](figure from [39]).

wires along the path of the particle, allowing the determination of its position. Calibration and trajectory reconstruction will be explained in section (3.2).

Table 2.2: BDC parameters

Drift length	2.5 mm
Pitch	5 mm
Anode	ϕ20 μm Au-W/Re
Potential wire	80 $\mu m\phi$ Au-Al
Cathode (gas window)	8 μm^t Al-Kapton $\times$ 9(2)
Wire configuration	XX'YY'XX'YY' (8 planes)
Effective area	80×80 mm^2
Readout	128 channels/chamber (16 wires/plane)
Operating gas	i-C4H10 at 100 (50) Torr
Vacuum window	80(16) μm^t Kapton $\times$ 2
Thickness	L/Lr = 0.9×10^{-3}

2.4 Solid Hydrogen Target

In order to perform our $(p, p\alpha)$ reaction in inverse kinematics, a proton target is needed. Typically, a hydrocarbon target, such as polyethylene (CH_2), is employed due to its ease of production and low cost. However, it can be associated with a relatively high background in high-momentum-transfer reactions due to the carbon present in the matrix.

Therefore, a target of pure solid hydrogen (SHT) has provided a better solution as it provides much less background for the same number of hydrogen nuclei, in addition to ten times more protons for the same thickness, and much lower angular straggling [53]. The solid hydrogen target has been developed for use in direct reaction experiments performed in inverse kinematics, which can utilize ESPRI since thin liquid hydrogen targets (LHT) do not have a uniform thickness due to differences in pressure inside and outside the target cell, which lowers missing mass resolution [55]. For compatibility with the $(p, p\alpha)$ reaction for this study, the reaction chamber has been modified to enable its coupling with ESPRI and allow the detection of protons around 60 degrees. The SHT was formed by allowing pure para-hydrogen ($p - H_2$) to grow on a 2-mm-thick copper plate covered by 2 layers of 6 μm thick Aramid on the front and back sides [53] as shown in Fig. 2.10(a). A mechanical press made of aluminum plates and a neodymium magnet was



(a) (b)

Figure 2.10: Schematic view of SHT chamber window materials (left). Picture of SHT with a hole highlighted by dashed line taken during the experiment (right)[51].

used to allow it to overcome problems from thermal radiation from outside sources and to prevent swelling of the target during solidification [56]. The SHT formed was 2-mm-thick, with a diameter of 30 mm and a density of 0.086 g/cm^3 (1.03×10^{22}/cm^2).

The SHT produced for the SAMURAI12 experiment by the SHT team can be shown in the picture in Fig. 2.10(b). The dashed ellipse highlights a small hole on the target, which was seen at the same position even after the end of the experiment. Accordingly, an effective area was determined during the analysis [51].

2.5 Recoil protons detection (ESPRI)

In order to detect recoil protons from the $(p, p\alpha)$ reaction, the ESPRI spectrometer has been exploited [57]. ESPRI is composed of two arms installed at the left and right sides of the SHT chamber windows, at a distance of about 1 m from the target. It consists of three types of detectors (recoil drift chamber (RDC), plastic, and NaI(Tl)) that enable the determination of the scattering proton energy and angle. To avoid energy loss by protons and multiple scattering in atmospheric air, a bag filled with helium (Fig. 2.11) at a pressure of 1 atm was placed between the SHT window and the RDC, which improves the missing mass

resolution.

2.5.1 RDC

Recoil **D**rift **C**hamber (RDC) is a multi-wire drift chamber designed to detect the position of the protons by reconstructing a track that allows the calculation of the scattering angle. Each RDC consists of 7 planes with configuration XY'XY'X'YX, and each plane consists of 32 wires with a drift length of 7 mm. The detector has an effective area of 436×436 mm^2 and covers a range of $(50^\circ - 70^\circ)$ in laboratory frame or $(40^\circ - 70^\circ)$ center of mass (CM) frame [57]. Due to a noise problem in the first layer (X layer), the track reconstruction algorithm was done with 6 layers only, and the noisy layer was excluded. The typical spatial resolution for both the X and Y layers was about 0.5 mm with an efficiency above 90%. Table 2.3 highlights the main aspects of RDC.

Table 2.3: RDC parameters

Drift length	7 mm
Pitch	14 mm
Anode wire	$\phi = 30\mu m$ Au-W/Re
Cathode wire	$\phi = 100\mu m$ Be-Cu
Wire configuration	XY'XY'X'YX' (7 planes)
Effective area	436×436 mm^2
Readout	224 channels/chamber (32 wires/plane)
Operating gas	$Ar - C_2H_6$(50%) at 1000 Torr

2.5.2 Plastic scintillator

Detection of proton ToF, as well as energy loss, was done by a large area plastic scintillator of the type BC-408 of dimensions 440(H) $\times$ 440(V) $\times$ 4(T) mm^3 on each arm. Each plastic scintillator was wrapped with 25 μm Al foil and a 200 μm polyethylene sheet. Typically, there are two photomultiplier tubes (PMTs) coupled to the top and bottom ends of the plastic, and the average of the two signals is taken. However, the upper PMT occasionally malfunctioned and an algorithm was employed to always select the bottom PMT except for events where the bottom PMT signal was noise and the upper PMT signal was good. The

trigger for ESPRI would fire if either the left or right arm had a hit in both up and down, following the logic L($U \times D$) || R($U \times D$).

2.5.3 NaI(Tl) scintillator

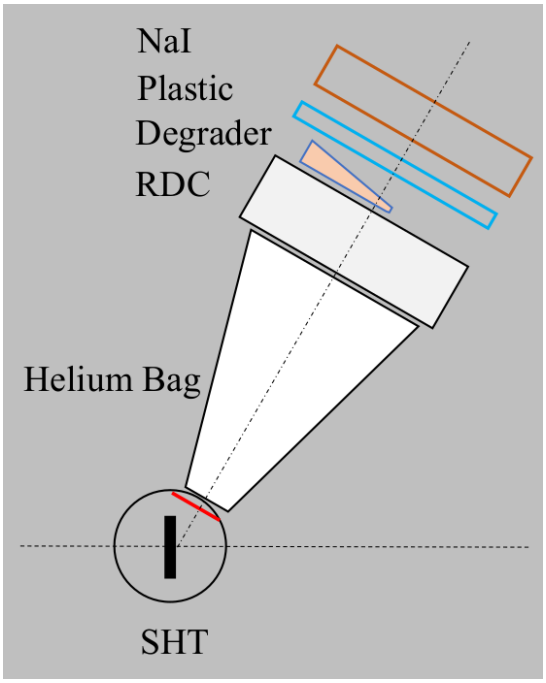


Figure 2.11: Schematic view of the layers of ESPRI.

The full energy reconstruction of the recoil protons was done by an array of 7 NaI(Tl) scintillators with dimensions of 431.8 × 45.72 × 50.8 mm^3 placed behind the plastic scintillator. Each NaI(Tl) scintillator can typically recover the full energy from protons up to 100 MeV; however, the kinematics allow proton energies up to 150 MeV in the NaI(Tl) detectors. To solve this problem, a wedge-shaped copper degrader of width 236.5 mm and thickness ranging 2-30 mm covering 55° – 62.5° angular region was placed between the RDC and the plastic to slow down high-energy protons to enable their full energy detection by the NaI(Tl). Figure 2.11 shows the shape of the degrader.

2.6 Cluster detection system (Telescope)

The energy and scattering angle of the alpha cluster resulting from the $(p, p\alpha)$ knockout reaction are measured using the cluster detection system Telescope, which is situated at forward angles covering

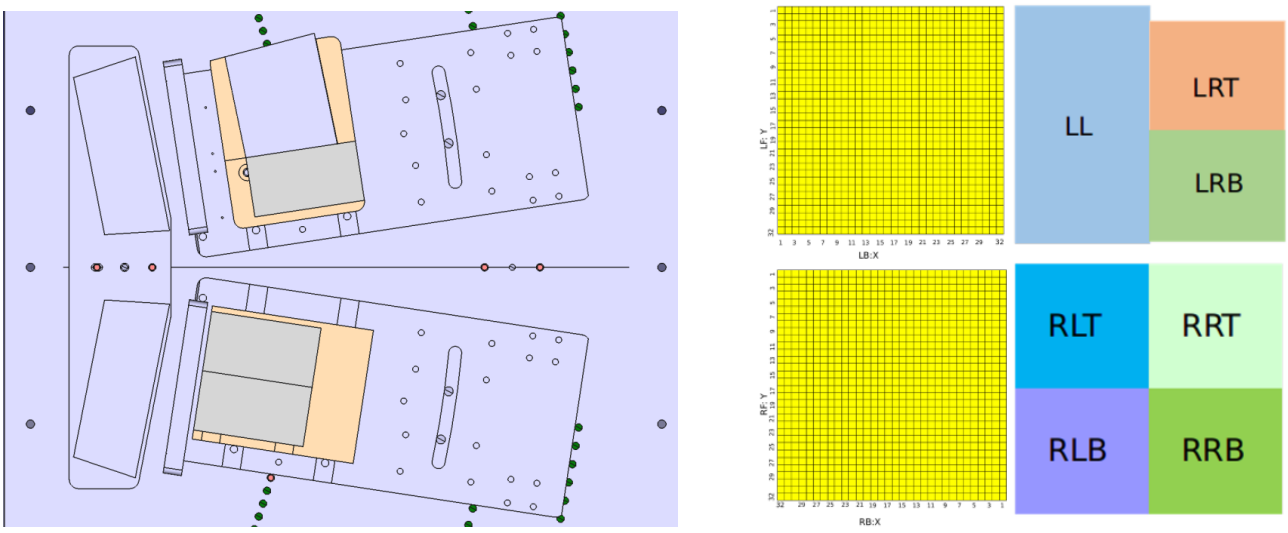


Figure 2.12: Top view of Telescope arms (left) and detector configuration scheme (right).

4° − 12°. Similar to ESPRI, Telescope is comprised of two arms; however, it consists of two detectors instead of three. The first detector is a **D**ouble-sided **S**ilicon **S**trip **D**etector (DSSD) of the type BB7 from Micron Semiconductor Ltd [58], which was used to detect the position and energy loss of the knock-out cluster with forward angle and projectile-like velocity. Following the DSSD, CsI(Tl) detectors are placed to detect the full energy of these clusters. The BB7 DSSD has 2 mm wide strips and an effective area of 64×64 mm^2 and was placed 35 cm downstream of the target. As for the CsI(Tl) detectors, there were two types present in the Telescope setup. The first type of detectors was from the FARCOS array [59] while the second-type detectors were from the CHIMERA array [60]. The right arm of the Telescope setup contained four identical CsI(Tl) crystals of the first type, while the left arm included two crystals of the first type placed on the right side and one large crystal of the second type placed on the left side, as shown in Fig. 2.12 (right). In order to guarantee that the energy range of Telescope is sufficient, a 25-mm-thick aluminum degrader was placed in front of each DSSD in each arm. The alpha energy straggling with beam velocity within the degrader was calculated to be 0.4 MeV/nucleon, which is smaller than the energy resolution of the modules by a factor of three. Details of the parameters of Telescope are shown in table 2.4

Table 2.4: Telescope parameters.

DSSD	Type	BB7 with kapton readout from Micron Semi. Ltd
	Pitch	2 mm
	Strips/Elements	32×32 (Junction + Ohmic Side)
	Active area	64×64 mm^2
	Thickness	1500 μm
CsI(Tl)	Left Array	2 (Type1) + 1 (Type2)
	Right Array	4 (Type1)
	Type1	$32 \times 32 \times 32$ mm^3
	Type2	$86.4 \times 61.2 \times 50$ mm^3

2.7 SAMURAI magnet

One of the major reasons behind the SAMURAI spectrometer's ability to separate and identify a myriad of nuclei is the existence of the SAMURAI magnet. When the beam-target interaction takes place, the beam-like nuclei and some of the other nuclei produced from the reaction go to the SAMURAI magnet, where they are separated by the high-intensity magnetic field according to their charge and momentum. The charged particles are detected after the magnet by FDC2 and the hodoscope, while the neutrons are tagged by NEBULA. The SAMURAI (**S**uperconducting **A**nalyzer for **MU**lti-particles from **RA**dio**I**sotope beams) magnet is an H-type dipole wide acceptance superconducting magnet with a 2 m cylindrical pole. It has a large opening (±5° vertically and ±10° horizontally) with a large vacuum chamber of an effective gap 80 cm and an opening area of 294 cm horizontally and 80 cm vertically. For each exit window of the magnet, a 3 mm stainless steel (SUS) is used for neutrons and a combination of 0.3-mm-thick Kevlar and 70 μm thick Mylar foil is used for the charged particle. This enables it to accept different types of particles arising from reactions in addition to projectile-rapidity neutrons [39].

The magnet is placed on a rotatable base capable of rotating from −5° to +95°; during the experiment, it was placed at +30° rotation. The magnetic rigidity of the SAMURAI magnet is up to 7.1 Tm while the maximum field is 3.1 T. During the SAMURAI12 experiment, there were three magnetic field settings corresponding to the three physics beam settings used. The main parameters of the SAMURAI magnet can be seen in Table 2.5, while Table 2.6 highlights the magnetic field setting for each beam of the experiment.

The values in Table 2.6 were chosen based on calculations of the trajectory of the fragments produced

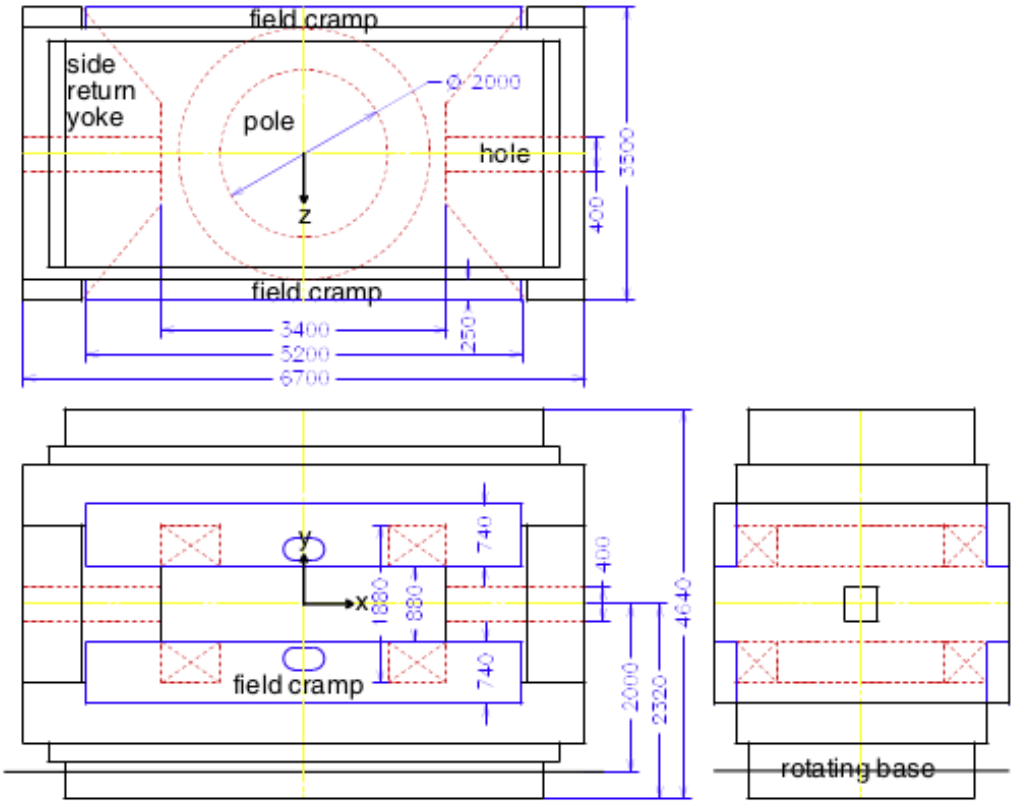


Figure 2.13: Schematic view of iron component of the SAMURAI magnet. X-Z plane view (top left), X-Y plane view (bottom left), Y-Z plane view (bottom right) (figure from [39])

Table 2.5: SAMURAI dipole magnet parameters [40]

Type	H-type
Pole	ϕ 2 m, 0.88 m (gap)
Maximum field	3.1 Tm
Maximum field integral	7.1 Tm
Number of turns	3414 turns/coil
Maximum current	563 A
Magneto motive force	1.9 MAT/coil
Stored energy	27.4 MJ
Coil cross section	180 mm $\times$ 160 mm
Current density	67 A/mm^2
Total weight	600 ton

Table 2.6: SAMURAI12 magnetic flux density settings.

^{10}Be beam	2.1 T
^{12}Be beam	2.7 T
^{14}Be beam	2.5 T

from the $(p, p\alpha)$ reaction to optimize the detection of the nuclei of interest. Figure 2.14 shows the trajectories calculations for the ^{14}Be beam and He residues at projectile-like velocity.

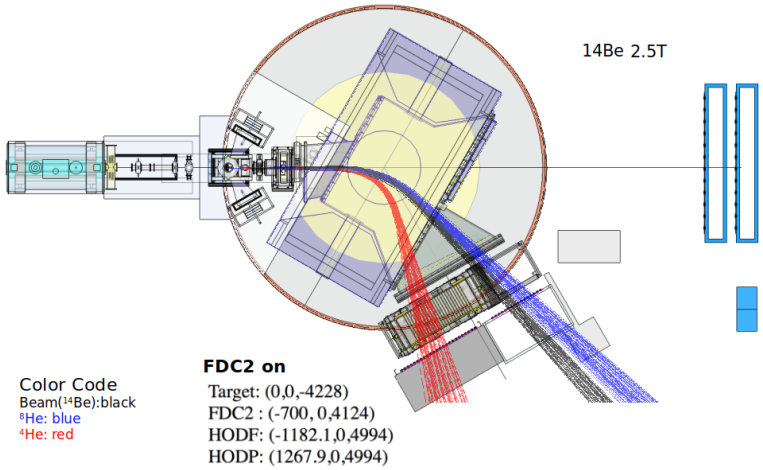


Figure 2.14: Trajectory calculations for beam and residues of interest in the case of ^{14}Be beam at 150 MeV/u. (Color code black:beam; red:^{4}He; blue:^{8}He).

2.8 Residual nucleus detection

After the $(p, p\alpha)$ reaction takes place at the target, the corresponding residue (^{6,8,10}He) needs to be detected to perform the missing mass calculations to extract the $6n$ spectrum. In order to achieve this goal, the scattering angle of the residue is detected via a Forward Drift Chamber (FDC0) placed perpendicular to the axis of the beamline, 0.8 m away from the target downstream. Afterward, the residue (or its charged decay components) is bent by the magnet, and a secondary forward drift chamber (FDC2) placed 3.7 m from the center of the magnet perpendicular to the 60° line, detects the position and scattering angle of these nuclei. Finally, these particles are identified by Hodoscope.

2.8.1 Forward drift chambers

2.8.1.1 FDC0

The first of the two forward drift chambers (FDC0), similar to the beam drift chambers, consisted of 8 layers with configuration XX'YY'XX'YY'. However, a key difference is the larger size of FDC0, which covers an effective area of 160×160 mm^2 with 32 wires per layer. The resolution of the reconstructed position was 100 μm with efficiency 99% [39]. The voltage and gas pressure of FDC0 were optimized for the detection of helium isotopes.

2.8.1.2 FDC2

The second forward drift chamber, FDC2, placed after the SAMURAI magnet, is crucial for the calculation of the energy of the decay alpha using its magnetic rigidity. FDC2 has dimensions of $2616(\mathrm{H}) \times 1156(\mathrm{V}) \times 876(\mathrm{T})$ mm^3 and is placed approximately 3.7 m away from the SAMURAI magnet perpendicular to the 60° line. Due to its large size, the FDC2 structure is quite different from that of the BDCs and FDC0. To avoid the bending of the horizontal wires, an XVU configuration was used with the U and V wires forming a $+30°$ angle and a $-30°$ angle with the vertical wires, respectively. The detector is composed of 14 layers, each containing 112 wires with a drift length of 10 mm in the configuration (sXX'-sUU'-sVV'-sXX'-sUU'-sVV'-sXX') with each double layer (XX',UU',VV') separated by 100 mm pitch with shield layer in between as shown in Fig. 2.15 [39]. During the ^{10}Be and ^{12}Be beam settings, FDC2 was turned off due to the beam's high intensity. For the analysis of FDC2, the U layers were not included in the track reconstruction algorithm due to higher noise (residue of U-layer always larger than the residue of neighboring X/V-layer by at least 20%) than that of the other layers which reduced the overall resolution when included (10 layers were considered).

.

2.8.2 Hodoscope

The particle identification of the residue (or its decay products) was done using two sets of plastic scintillators called Hodoscope, which measure the energy loss and time-of-flight. The first set is called

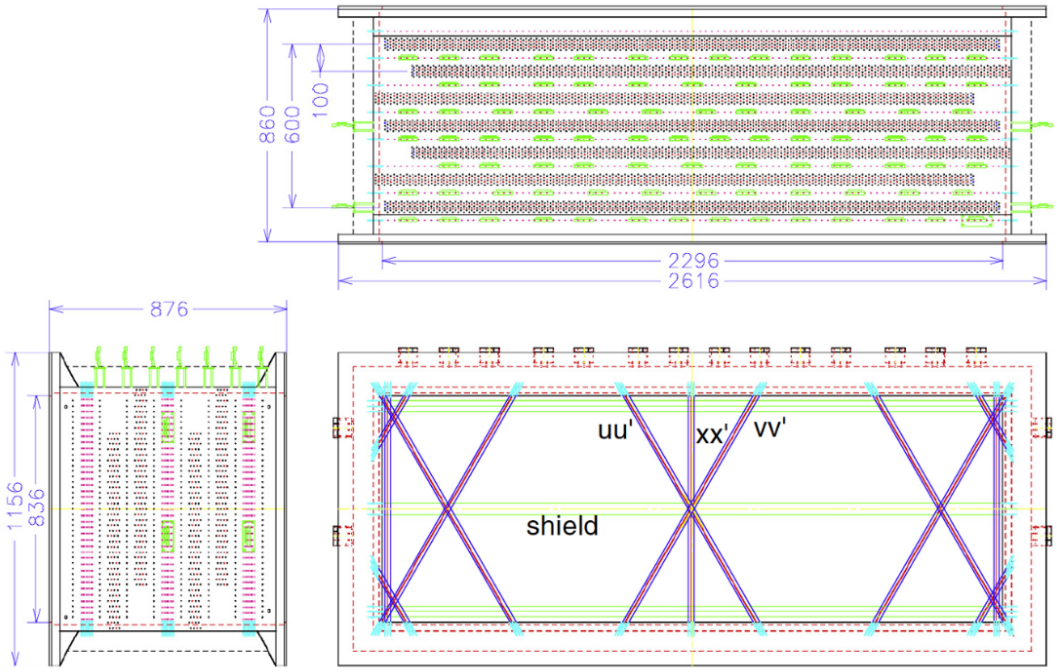


Figure 2.15: FDC2 schematic view [39].

Table 2.7: FDC2 parameters [39]

Drift length	10 mm
Pitch	20 mm
Anode wire	$\phi = 40\mu m$ Au-W/Re
Shield wire	$\phi = 80\mu m$ Au-Al
Layers	14 layers with 8 shield layers
Wire configuration	sXX'-sUU'-sVV'-sXX'-sUU'-sVV'-sXX' (14 planes)
Effective area	$2.2(H) \times 0.8(V) \times 0.8(T)$ m^3
Readout	1568 channels (112 channels/layer $\times$ 14)
Field (shield) wires	4788(328)
Operating gas	He + 50%C_2H_6(50%) at 1 atm
Gas, shield window	50 μm Mylar $\times$ 2, 12 μm Al-Mylar $\times$ 2
Thickness	L/Lr = 1.8×10^3

Hodoscope for fragments (HODF) which comprises 24 identical plastic bars of dimensions 10(H) × 120(V) × 1(T) cm^3 with an (R7195 Assy) PMT coupled to each of the two ends of the plastic. The second set is called Hodoscope for protons (HODP), and it consists of 16 plastic scintillators identical to the ones in HODF. Both HODF and HODP were placed after FDC2, 5 m downstream from the SAMURAI magnet exit window. There is a 20 cm gap between HODF and HODP. For the ^{10}Be and the ^{12}Be beam settings, the magnet was tuned so that most of the beam passes through that gap to avoid a high counting rate in the Hodoscopes.

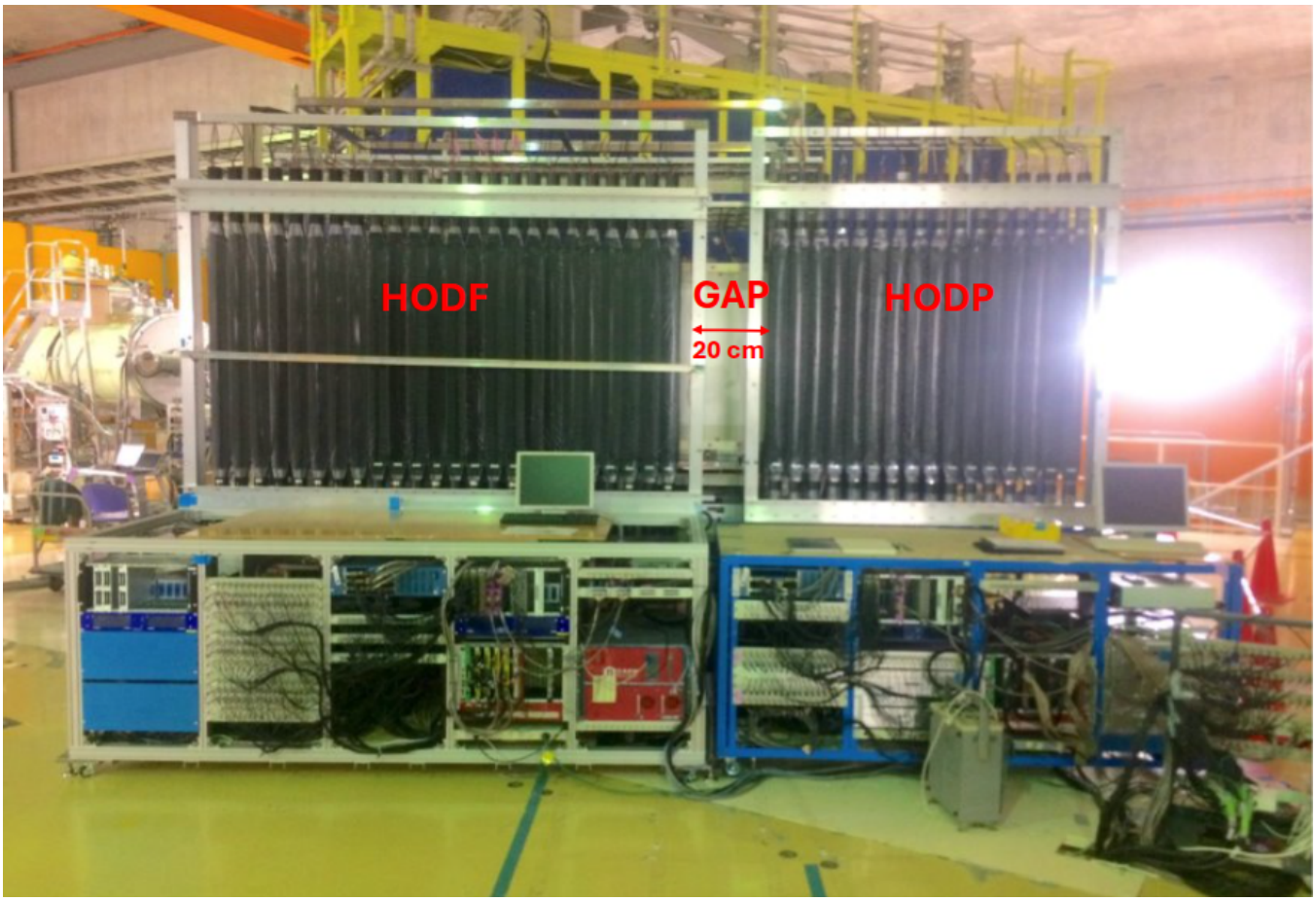


Figure 2.16: Hodoscope view of SAMURAI12.

2.9 Neutrons detection (NEBULA)

Neutrons produced by the $(p, p\alpha)$ reaction traverse through the SAMURAI magnet unaffected; however, they can be tagged by the NEBULA array. **NE**utron-detection system for **B**reakup of **U**nstable Nuclei with **L**arge **A**cceptance or NEBULA, for short, is a high-efficiency neutron detector with large acceptance that

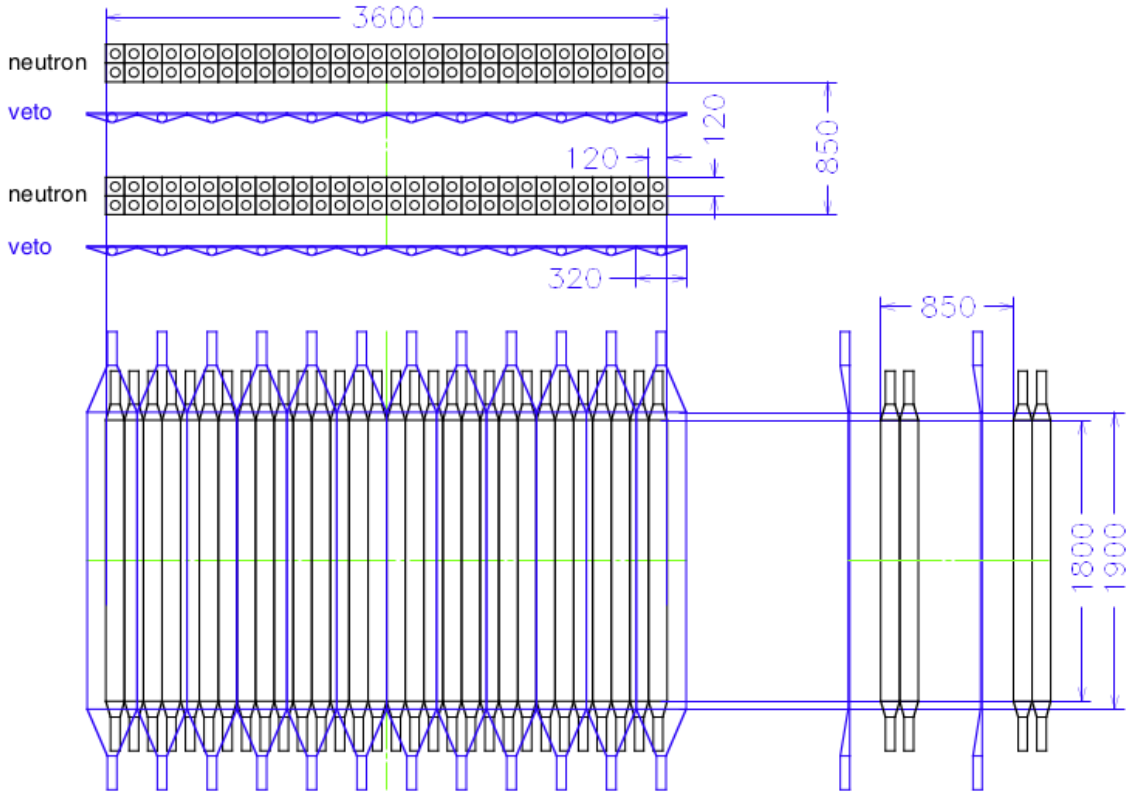


Figure 2.17: Schematic view of NEBULA [39].

is capable of detecting projectile-rapidity neutrons at 100-300 MeV. It is comprised of two walls of plastic scintillators placed around 11.6 m away from the target at 0° downstream from the SAMURAI magnet. There are 120 modules to detect the neutrons and 24 modules to detect charged particles that act as VETO detectors. The modules formed 6 layers (3 layers per wall), and each wall was organized into two layers of neutron detectors (black) followed by a layer of VETO detectors (blue) as shown in Fig. 2.17. Each layer of neutron detectors consisted of 30 plastic scintillators capable of neutron detection, while each layer of VETO detectors consisted of 12 modules of plastic scintillators. The plastic scintillators were placed vertically with PMTs connected to each end of the plastic. The effective area of the NEBULA was around 3.6 m (H) $\times$ 1.8 m (V) with angular acceptance of ±8.8° horizontally and ±4.4° vertically. Table 2.8 highlights key parameters of NEBULA. The intrinsic detection efficiency of NEBULA was estimated through simulation to be 40% for 1 neutron and 12% for 2 neutrons [39]. For the sake of the analysis done in this work, the NEBULA data were not analyzed; however, it was utilized as a trigger to reduce the background.

Table 2.8: NEBULA parameters [61]

Neutron detectors	
Module	BC408
Dimensions	12(H) × 180(V) × 12(T) cm^3
Configuration	30 modules/layer × 4 layers
Total thickness	48 cm
Efficiency	1n ≈ 40%, 2n ≈ 12%
VETO detectors	
Module	BC408
Dimensions	32(H) × 190(V) × 1(T) cm^3
Configuration	12 modules/layer × 2 layers
Photomultiplier Tubes	R7724 Assy × 288

2.10 Triggers

The data obtained from the different systems of the experiment, whether from RIBF or SAMURAI, is handled using the RIBF **D**ata **A**cquisition **S**ystem, or DAQ for short. The RIBF DAQ is a flexible and configurable system capable of handling large quantities of data with high frequency (up to 5 MB/s). The electronic modules (VME or CAMAC) of each detector system are connected to computers called front-end computers (FEC), these computers communicate via Ethernet connection and can access a common storage system located on a storage area network (SAN). Each detector system has its own event builder (slave event builder), and there is a master event builder that handles all of them. Figure 2.18 shows the typical configuration of RIBF DAQ; in this figure, "Status Data" represents a computer that relays data such as the magnetic field and high voltage (HV), while "Analyzer" is a computer that handles online analysis [62].

During the SAMURAI12 experiment, the beam trigger was defined as the coincidence between the beam plastics' (SBT1 and SBT2) signals, which was used as the start time for the ToF measurements. A factor of 1500 was used for downscaling the beam trigger for the DSB trigger, which recorded the total beam count. As for the Physics trigger, it required a coincidence between the triggers of Beam, ESPRI, and Telescope. Details of the triggers used in the experiments are shown in Table 2.9.

The intensity of the ^{14}Be beam setting used for the 6-neutron study was 2.5×10^5 pps corresponding to the full acceptance of the beamline; consequently, the duration of the physics beam time was 76 hours which was relatively longer than other beam settings. Additionally, a set of empty target runs was recorded

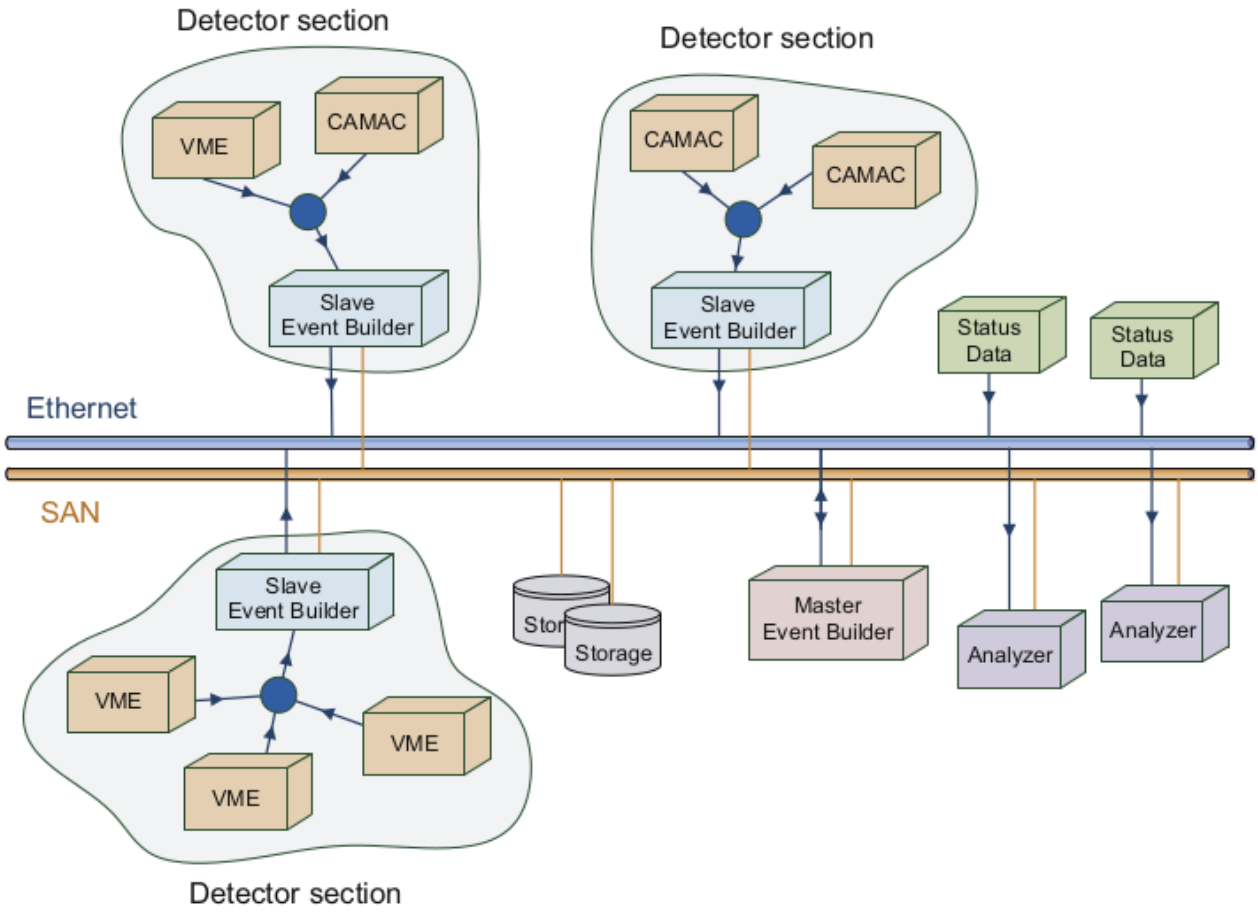


Figure 2.18: Typical configuration of RIBF DAQ (figure from [62]).

for background reduction and to improve analysis quality. Finally, two de-focused alpha beam settings were used for calibration purposes using beam energies of 150 MeV/u and 120 MeV/u. The purity of the beam for each setting was roughly 100%, and the SAMURAI magnetic field was optimized for the expected residue nuclei of interest. Details of the experiment run summary can be seen in Table 2.10.

Table 2.9: Trigger list of the S12 experiment.

Subsystem	Signal	Trigger list
Beam	SBT	DSB Beam(1500)
ESPRI	PMT $L(U \times D)\|\|R(U \times D)$	Beam x ESPRI
Telescope	DSSD	Beam x Telescope
NEBULA	PMT $(U \times D)$	Beam x NEBULA
Hodoscope	PMT $(U \times D)$	Beam x Hodoscope
Physics		Beam x ESPRI x Telescope

Table 2.10: S12 experiment run summary.

Beam	Run type	Intensity (pps)	Duration (hr)	Conditions
^{14}Be	Physics	200k-250k	76	B = 2.5T,FDC2 on
^{14}Be	Empty target	200k-250k	6.5	B = 2.5T,FDC2 on
^{4}He	Calibration	500	1.8	Defocused beam,150 MeV/u
^{4}He	Calibration	500	1	Defocused beam,120 MeV/u

Chapter 3

Analysis

In this chapter, the calibration process needed to convert raw data obtained from the various detectors' electronics into physical variables that can be used for the missing mass calculation, will be discussed. In order to perform this calculation, the four-momentum vectors for the secondary beam and the recoil protons and alpha of the quasi-free scattering reaction are needed. The calibration of the beamline plastic scintillators, beam energy determination and secondary beam particle identification will be discussed in section 3.1. Section 3.2 will describe the conversion of hits on wires inside the beamline drift chambers and their conversion to position using space time conversion (STC), trajectory reconstruction and determination of its resolution. In addition, the determination of beam position on target will be presented and related cuts will be shown. Subsequently, section 3.3 will discuss the calibration of ESPRI and determination of the recoil particle PID using $\Delta E - E$ and $\Delta E - ToF$ methods with the ToF correction. The alpha clusters measurement device Telescope will be calibrated in section 3.4 and the $\Delta E - E$ PID will be determined as well as the alpha cut. Section 3.5 will illustrate FDC2 calibration and position determination after the magnet. Finally, section 3.6 will explain the $B\rho$ calculation and section 3.6.1 will discuss the Hodoscope PID. Part of the calibrations presented in this document has been performed in [51]; they were checked in the present work.

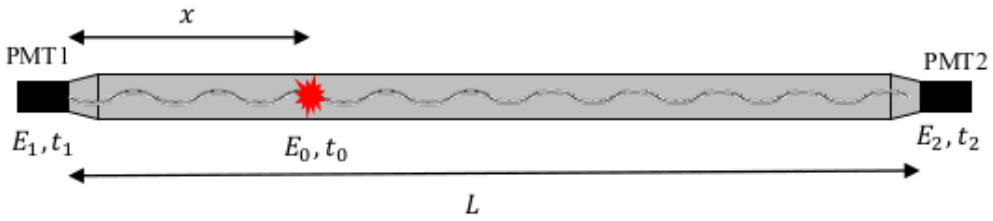


Figure 3.1: Scheme of plastic scintillator.

3.1 Beam Plastics

Each beamline plastic is connected to two photomultiplier tubes by its ends. When scintillation light is generated inside the plastic, its energy and time measurements are recorded by both PMTs. These values should be the same, only if the light is generated in the middle of the plastic. However, this is generally not the case. Accordingly, the energy and time measures of one PMT has a higher and lower value, respectively, than the other PMT depending on the original location of the scintillation light. In the case of the timing measurement, as shown in Fig. 3.1, assuming the light is generated at time t_0 and position x mm away from PMT1 when L is the length of the whole plastic scintillator, and v is the speed of light in the plastic, then we have

$$t_1 = t_0 + \frac{x}{v} \tag{3.1}$$

$$t_2 = t_0 + \frac{L - x}{v} \tag{3.2}$$

by combining equations 3.1 and 3.2, we solve for t_0

$$t_0 = \frac{t_1 + t_2}{2} - \frac{L}{2v} \tag{3.3}$$

since $(\frac{L}{2v})$ is a constant depending on the length of the plastic and the speed of light in it ($\sim$ 0.3 ns). Hence the timing information is proportional to the arithmetic mean of both PMT signals.

Similarly, the energy measurement of the scintillation detector is dependent on the position in which the light was generated because the light from the scintillation attenuates as it passes through the medium of the plastic. Assuming the energy is E_0, energy of PMT1 is E_1 and energy of PMT2 is E_2 then we have

$$E_1 = E_0 e^{-\lambda x} \tag{3.4}$$

$$E_2 = E_0 e^{-\lambda (L-x)} \tag{3.5}$$

then combining equations 3.4 and 3.5

$$E_0 = \sqrt{\frac{E_1 E_2}{e^{-\lambda L}}} \propto \sqrt{E_1 E_2} \tag{3.6}$$

as $(\frac{1}{\sqrt{e^{-\lambda L}}})$ is a constant depending on the length of the plastic and attenuation of light in the plastic, the energy information is the geometric mean of the energy of PMT1 and PMT2.

3.1.1 Time-of-flight calibration

The time-of-flight of the beam is calculated using the timing information obtained from the plastic scintillators. This is done using the Time to Digital Converter (TDC). TDC is an electronic module that depends on the digitization of two analog signals that are obtained from the PMTs of the plastic in this case. As mentioned in Chapter 2, the DAQ time start for the ToF measurement is the arithmetic mean of the time signal from SBT1 and SBT2 located at F13, and the time stop is the signal from the PMT corresponding to the focal point or detector of interest. The conversion of timing signal from channels to time (ns) is done using the linear equation 3.7.

$$ToF\ (ns) = \alpha T_{raw}\ (channel) + \beta \tag{3.7}$$

After converting the timing signal to represent actual time between the detectors, two corrections are needed for the time to be accurate; namely the slew correction and position correction.

3.1.1.1 Slew effect

In order for the TDC to convert an analog timing signal to a digital timing signal, it uses a leading-edge discriminator which utilizes a set threshold of the PMT voltage to initiate the time start (or stop). However, the main flaw of the leading-edge discriminator is the time walk or time slew. Suppose there are two analog signals **A** and **B** originating at the same time as shown in Fig. 3.2. Although signal **A** and signal **B** start

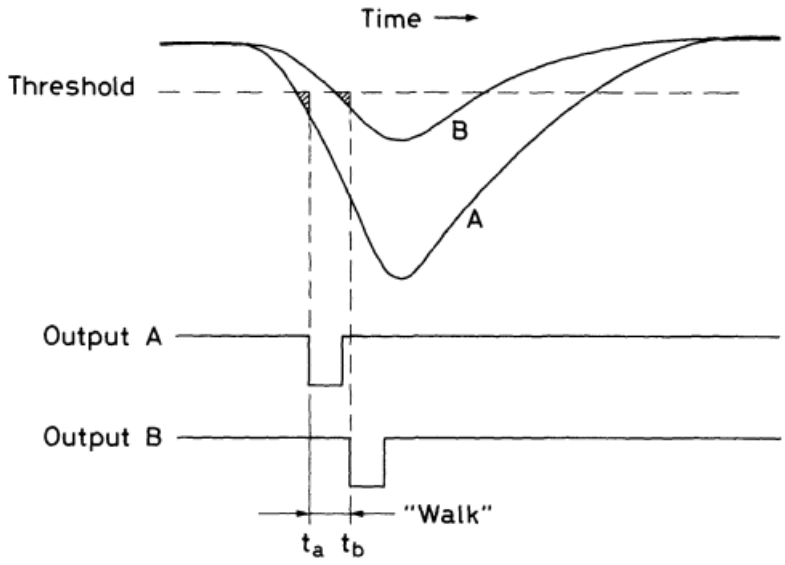


Figure 3.2: Illustration of the time walk effect (figure from [63]).

at the same time, the amplitude of pulse **A** is larger than that of pulse **B**, as the voltage threshold is fixed, the value of time (t_a) recorded for **A** will be smaller than the value of time (t_b) recorded for **B** and the difference between these two values will be proportional to the difference in the amplitude. Consequently, the time walk can be removed by applying a correction that accounts for the difference in amplitude; the correction used for this work can be seen in equation 3.8:

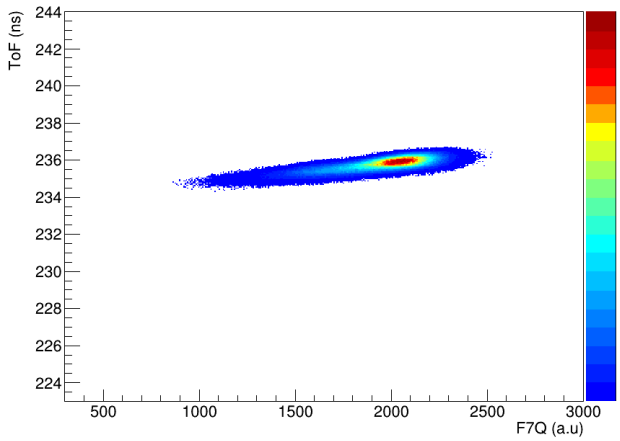
$$\Delta T_{walk} = p_0 + \frac{p_1}{\sqrt{Q}} \tag{3.8}$$

Figure 3.3a shows the ToF signal of plastic scintillator placed at F7 focal point in BigRIPS beamline vs charge of the ^{12}Be beam setting before applying the slew correction and Fig. 3.3b display the result after applying the correction. By comparing figures 3.3c and 3.3d that applying the correction improves the time resolution.

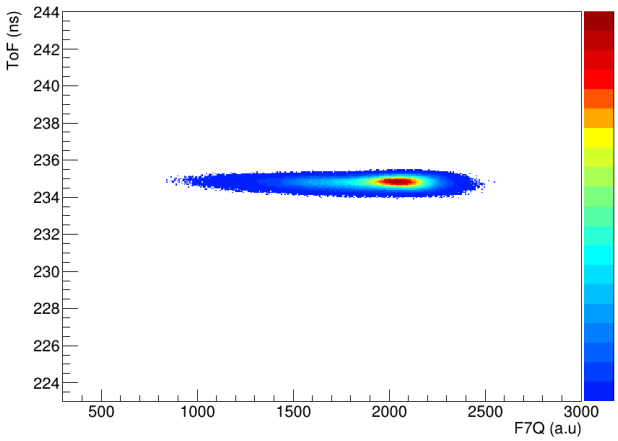
3.1.1.2 Position dependence

As mentioned in section 2.10, the starting signal of the DAQ system and beam trigger are taken from the timing signals of SBT1 and SBT2. Referring to equations 3.1 and 3.2, we can obtain

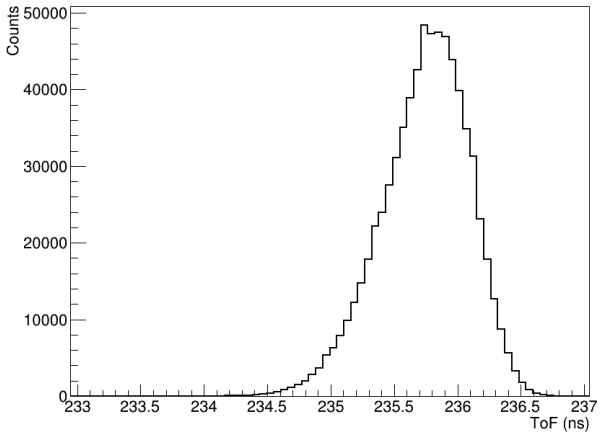
$$x = \frac{v}{2}(t_1 - t_2) + \frac{L}{2} \tag{3.9}$$



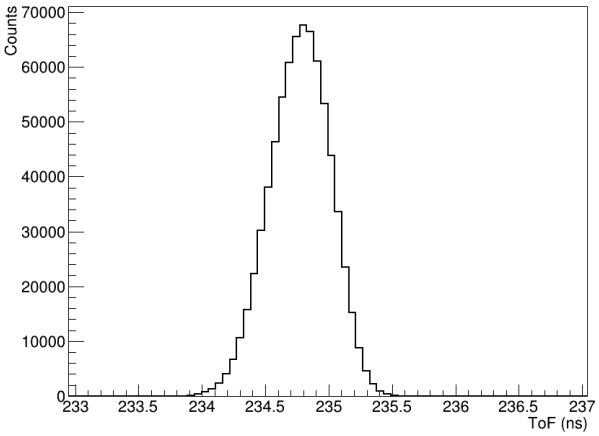
(a) F7 ToF vs charge before slew correction



(b) F7 ToF vs charge after slew correction



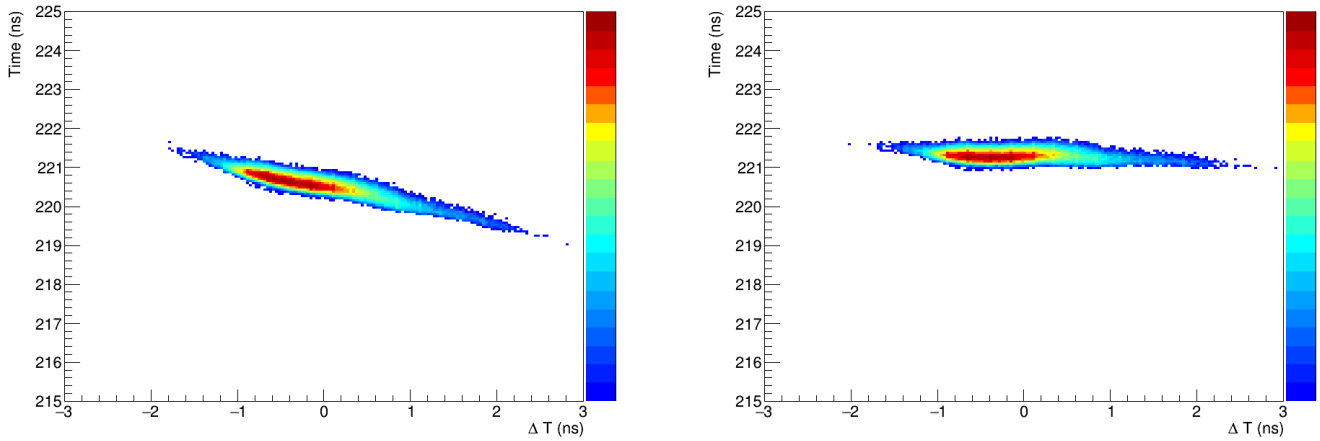
(c) Projection of ToF before slew correction



(d) Projection of ToF after slew correction

Figure 3.3: Correction of the slew effect on time-of-flight (ToF).

which demonstrates the position dependence of the time difference ΔT in each of the plastic detectors of F13 focal plane. Figure 3.4 shows the position dependence in the case of SBT1 which was corrected using a linear equation before and after the correction.



(a) SBT1 Time pre position correction (b) SBT1 Time post position correction

Figure 3.4: ^{12}Be SBT1 position correction in log Z scale.

3.1.2 Beam energy (ToF) and particle identification

The beam energy was determined from the ToF between F7 and F13 that can be determined using equation 3.10.

$$ToF_{F7-F13} = \frac{T_{SBT1} + T_{SBT2}}{2} - T_{F7} \tag{3.10}$$

The beam energy per nucleon was determined by knowing the ToF and distance between F7 and F13 and using the following formulae

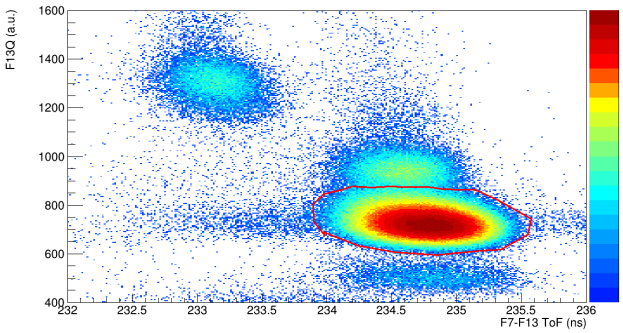
$$\beta = \frac{v}{c} = \frac{FL_{F7-F13}}{ToF_{F7-F13} \cdot c} \tag{3.11}$$

$$\gamma = \frac{1}{\sqrt{1-\beta^2}} \tag{3.12}$$

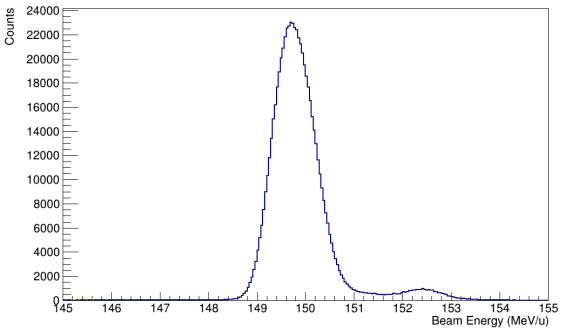
$$E_{beam} = (\gamma - 1) \cdot AMU \tag{3.13}$$

where $\boldsymbol{\beta}$ is the velocity, $\boldsymbol{FL}$ is the flight length between F7 and F13, $\boldsymbol{\gamma}$ is the Lorentz factor, and AMU is a conversion factor for atomic mass unit (MeV/c^2). The absolute time offset for the beam energy is determined using the $B\rho$ measurement of D6 dipole magnet which is located before F7. Lise++ code [64]

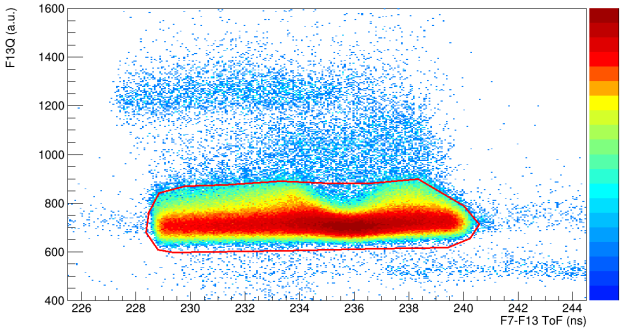
was used to determine energy losses in all elements up to the middle of the target. The beam energies and particle identifications (PID) of the three beam settings utilized during the SAMURAI12 experiment can be seen in Fig. 3.5. The red ellipses in the $\Delta E - ToF$ PID plots represent the beam cut utilized for the missing energy calculations. During the experiment, the beam purity of all the beam settings ($^{10,12,14}Be$) was above 90% with intensity of approximately 500 kHz for the $^{10,12}Be$ beam settings, and of approximately 200 kHz for ^{14}Be. For the ^{14}Be beam setting, the slits were fully opened allowing a much larger momentum acceptance. Consequently, the shape of the ^{14}Be PID is different from that of the $^{10,12}Be$ beam settings.



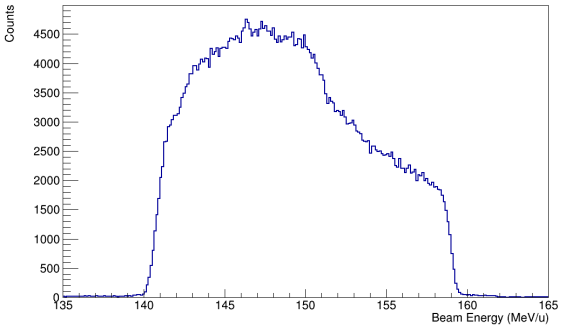
(a) ^{12}Be $\Delta E - ToF$ PID.



(b) ^{12}Be Beam Energy distribution.



(c) ^{14}Be $\Delta E - ToF$ PID.



(d) ^{14}Be Beam Energy distribution.

Figure 3.5: SAMURAI12 particle identification(Log Z scale) for three physics beam settings.

3.2 Beam Drift chambers

The trajectory of the beam is necessary to accurately determine the energy losses as well as properly aligning the trajectory of the different products of the $(p, p\alpha)$ reaction. This trajectory was obtained by properly calibrating the beam drift chambers BDC1 and BDC2 to convert the drift time to drift length and

using trajectory reconstruction algorithm to determine the track of the particle inside the drift chamber and obtain a position and direction for the ^{10,12,14}Be nuclei at the target. Due to the great similarities between FDC0 and BDC1/2 as mentioned in section 2.3, the same calibration procedure and tests were utilized for both species of detectors. This section will explain the calibration procedures, track reconstruction, and determination of the position of the beam on target.

3.2.1 Calibration

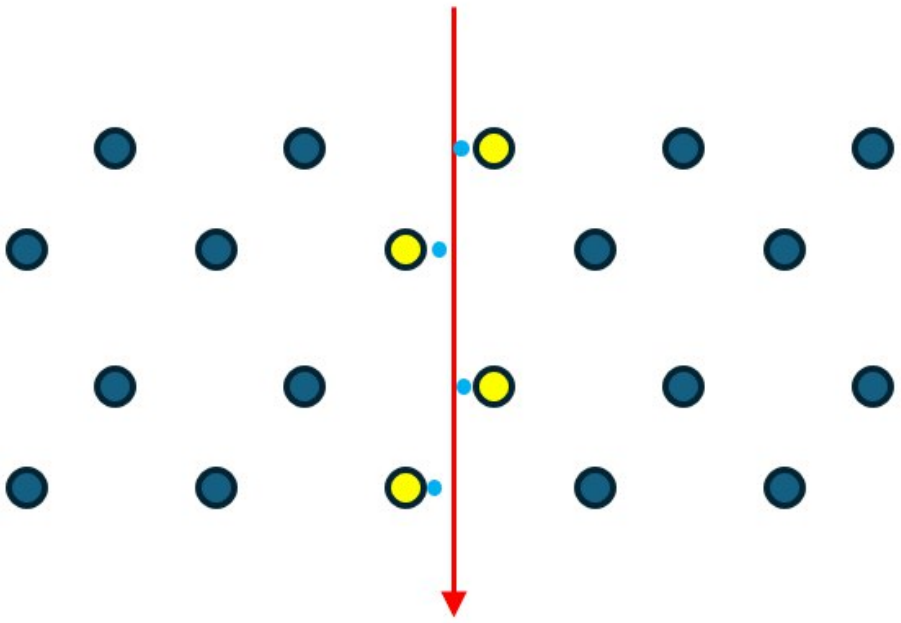


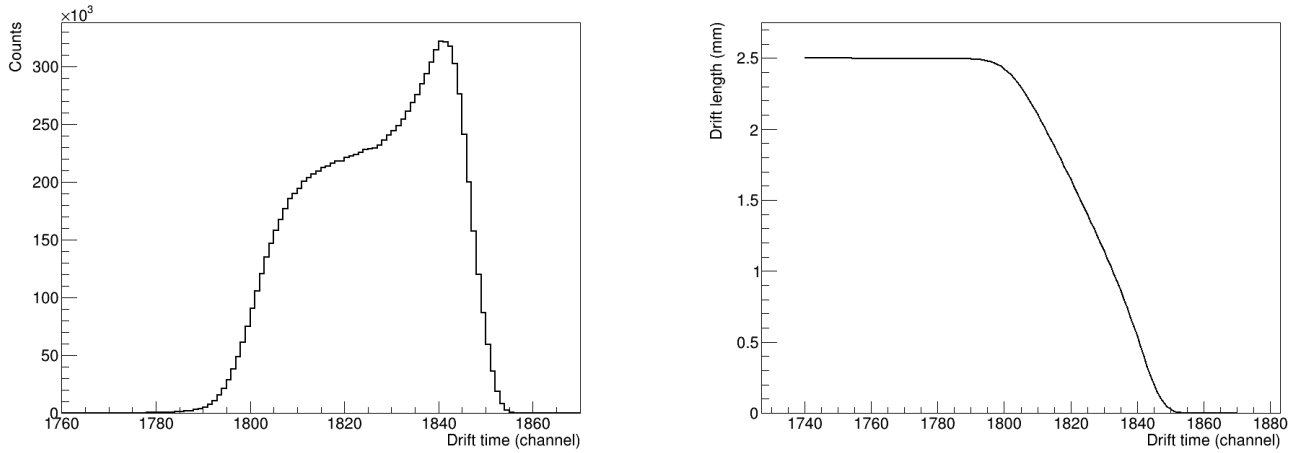
Figure 3.6: Scheme of the tracking process in the drift chamber.

When a charged particle passes through the gas inside the drift chamber, it continuously ionizes the gas medium along the path of the particle. The electrons produced from this ionization process drift to the wires of the drift chamber and drift time is measured. The calibration process depends on the conversion of this drift time to drift length in a process called Space-Time Conversion (STC). The STC process provides the position on each XY-plane relative to the wires, then the least square method (LSM) for fitting can be used to reconstruct a track enabling the attainment of the position and direction at the center of BDC as mentioned in [65]. To elaborate, looking at Fig. 3.6, the distance between two adjacent wires is 2d with each layer of wires shifted by distance of 1d from its adjacent layer. Consequently, the maximum distance an electron can travel from its generation to the anode is 1d. A uniform distribution in the range [0,d]

is assumed for the possible hit position of the beam particle referenced to [51]. Function 3.14 has been utilized to convert the drift time to drift length

$$\frac{L(t)}{d} = \frac{\int_{t_{min}}^{t} f(t)}{\int_{t_{min}}^{t_{max}} f(t)} \tag{3.14}$$

In this function, **L(t)** is the drift length, **t** represents the raw TDC signal from the drift chamber and f(t) the TDC distribution. Fig. 3.7 represents a typical TDC spectrum with the corresponding STC spectrum representing the drift length.



(a) BDC1 TDC. (b) BDC1 space-time conversion

Figure 3.7: Example of BDC1/2 and FDC0 STC.

3.2.2 Track reconstruction and residue

As mentioned in section 2.3, the wire configuration of BDC1, BDC2, and FDC0 is very similar. Accordingly, the same treatment was done for all three of them to reconstruct the track. The hit position in each layer is determined using the position of the wire(s) and performing the STC to determine how far the hit position is from the wire. Equation 3.15 demonstrates how the hit position for each layer is obtained.

$$Pos_{x/y} = Pos_{wire} + Drift\ Length \tag{3.15}$$

As for the trajectory of the beam, the positions tracked through 4 layers are used to perform least-square fitting in the xoz and xoy planes and obtain a possible track. In a perfect scenario, only one wire is fired

when a particle passes near it, however, multiple wires are fired in a practical situation. To properly perform the fitting, different possible combinations of wires hit positions are considered, and the χ^2 for each track is calculated with the most probable track having the minimum χ^2 value of the fitting. Suppose a particle

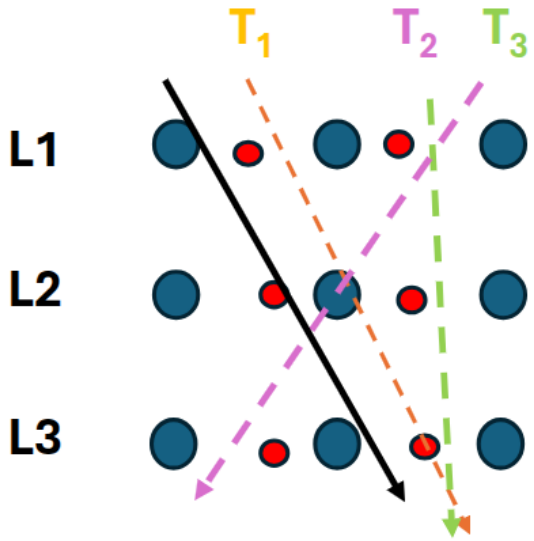
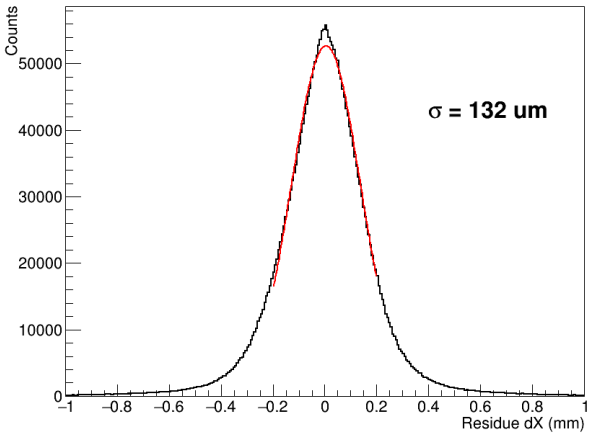


Figure 3.8: Example of the reconstruction of a track.

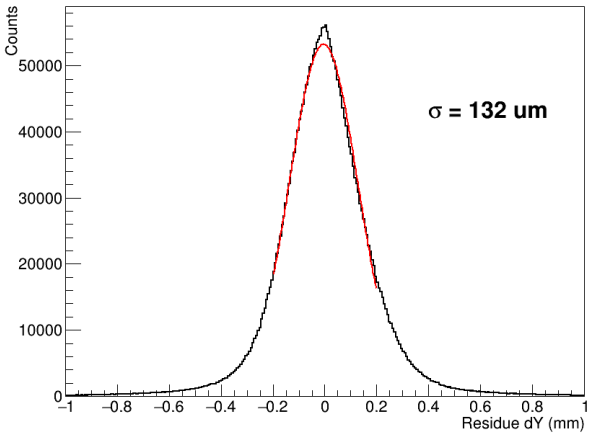
passes through the drift chamber as indicated by the black arrow in Fig. 3.8. As the particle ionizes the gas, electrons will drift to the closest wire and we would have a hit position, however, the hit could be on either side of the wire as shown by the red dots. Therefore, multiple possible tracks can be considered (T_1, T_2, T_3). The χ^2 value of each track is determined and the track with the least χ^2 will be considered (T_1 in this example) assuming no angular straggling. The difference between position deduced from the track (x_{track}) and the position of the hit (x_{hit}) is defined as the fit residue ($dx = x_{track} - x_{hit}$) of the fit. The goodness of the fit is estimated by the χ^2 which can be defined as

$$\chi^2 = \sum (dx)^2 = \sum (x_{track} - x_{hit})^2 \tag{3.16}$$

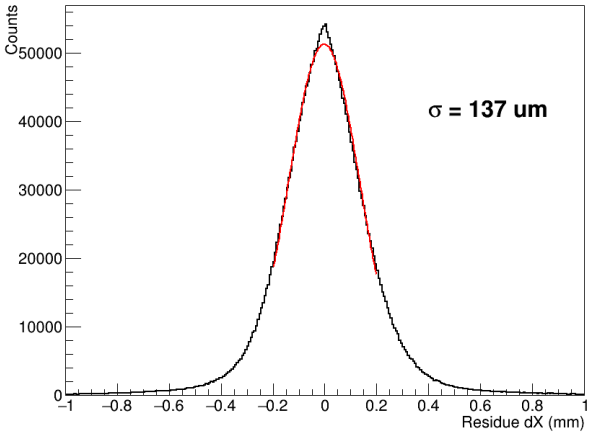
The residue in X and Y for BDC1, BDC2, and FDC0 can be shown in Fig. 3.9. As can be seen, the resolution of all three detectors is around 120 um as all three of them have a pitch of 5 mm and they all have a similar layer structure. As reported in [51], the overall detection efficiency of the BDC1/2 and FDC0 for each beam used in the experiment was found to be larger than 99%.



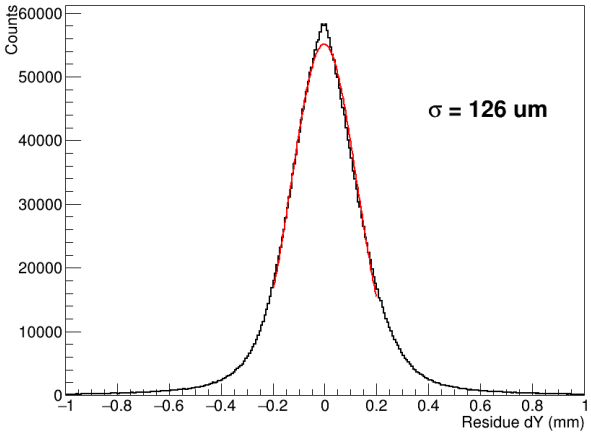
(a) BDC1 X



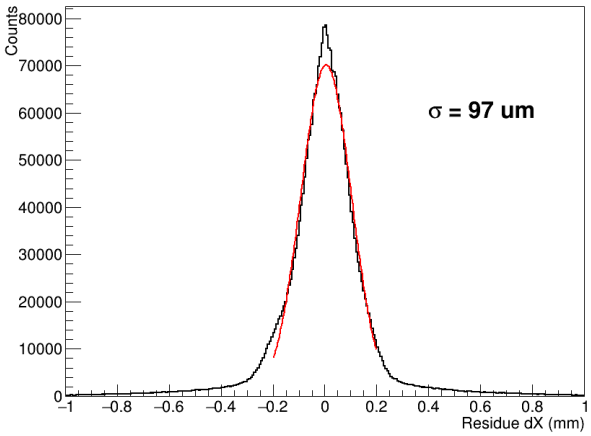
(b) BDC1 Y



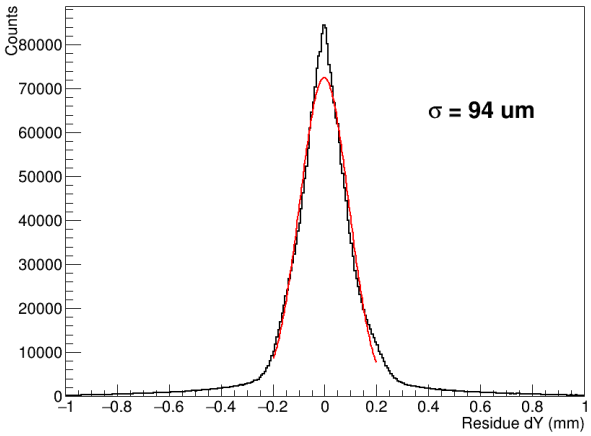
(c) BDC2 X



(d) BDC2 Y



(e) FDC0 X



(f) FDC0 Y

Figure 3.9: BDC1, BDC2, and FDC0 residue in X and Y.

3.2.3 Beam profile on target

The position of the beam nuclei on the target is essential for the determination of the reaction vertex and the determination of the beam angle that will be used to determine the thickness traversed in the target and to correct the angles of protons and alpha relative to that of the beam. As BDC1 and BDC2 lie before the target, the positions obtained from both these detectors are used to extrapolate the position of the beam on the target as shown in Fig. 3.10. Formulae 3.17 and 3.18 were used to reconstruct the beam angle while formulae 3.19, and 3.20 were used for the target position.

$$tan\theta_x = \frac{X_{BDC2} - X_{BDC1}}{Z_{BDC2} - Z_{BDC1}} \tag{3.17}$$

$$tan\theta_y = \frac{Y_{BDC2} - Y_{BDC1}}{Z_{BDC2} - Z_{BDC1}} \tag{3.18}$$

$$X_{target} = tan\theta_x(Z_{target} - Z_{BDC2}) + X_{BDC2} \tag{3.19}$$

$$Y_{target} = tan\theta_y(Z_{target} - Z_{BDC2}) + Y_{BDC2} \tag{3.20}$$

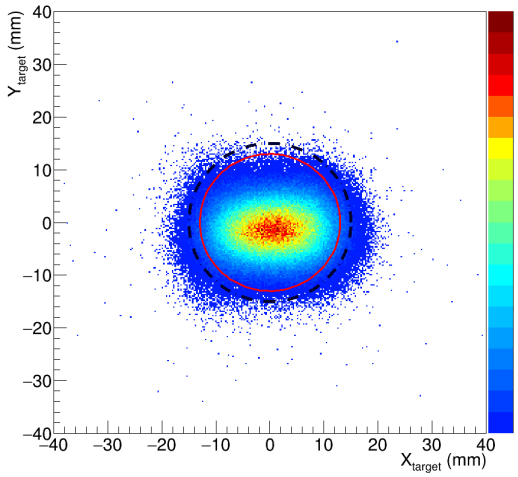
Figure 3.10 shows the beam profile for the ^{12}Be and ^{14}Be beam settings. The black circle represents the target frame of 15 mm radius while the red circle represents a cut used in the analysis that requires the events of interest to be in a circle of radius 13 mm in order to ensure the events considered are coming from interaction with the target. The majority of the events of the beam lie inside the beam cut on the target and some characteristics of the beam spots can be found in table 3.1. The ^{10}Be and ^{12}Be beam settings had a smaller beam spot than that of ^{14}Be beam setting. The vector positions of the beam and residues were determined using the following equations:

$$\overrightarrow{V}_{beam} = \overrightarrow{V}_{BDC2} - \overrightarrow{V}_{BDC1} \tag{3.21}$$

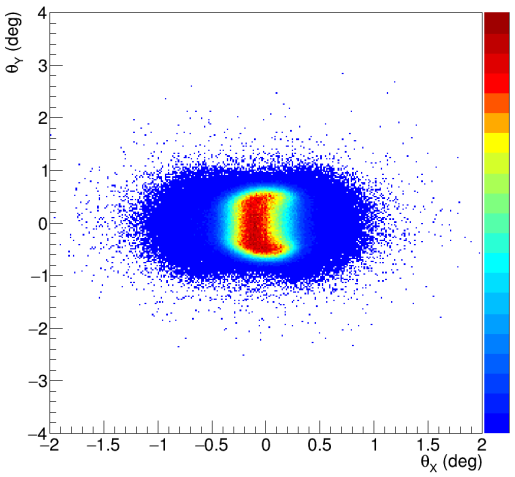
$$\overrightarrow{V}_{residue} = \overrightarrow{V}_{FDC0} - \overrightarrow{V}_{target} \tag{3.22}$$

$$cos(\theta_{residue}) = \frac{\overrightarrow{V}_{beam} \cdot \overrightarrow{V}_{residue}}{\left|\overrightarrow{V}_{beam}\right| \left|\overrightarrow{V}_{residue}\right|} \tag{3.23}$$

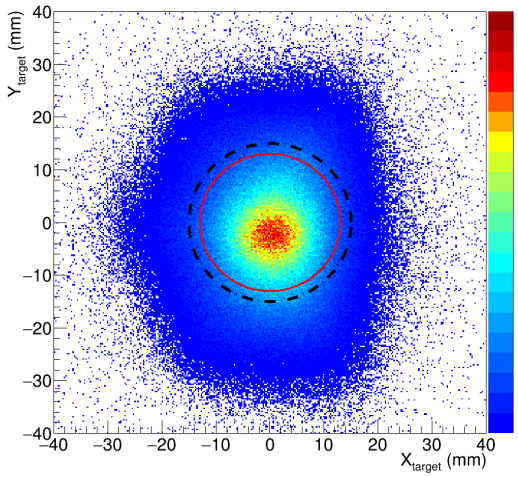
Where the $\overrightarrow{V}_{BDC1/BDC2}$ are defined from the center of the target to the position of BDC1/2 respectively, $\overrightarrow{V}_{beam}$ is the unit vector of direction of beam, $\overrightarrow{V}_{target}$ is the vector from BDC1 to the target, and $\overrightarrow{V}_{residue}$ is the vector of FDC0.



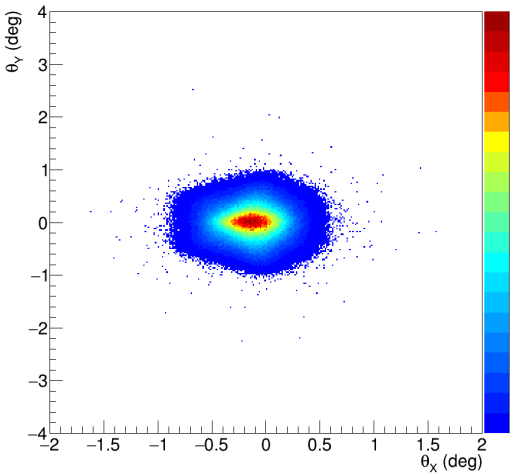
(a) ^{12}Be beam position on target with the target area cut highlighted in red circle.



(b) ^{12}Be reconstruction of beam angle on target.



(c) ^{14}Be beam position on target with the target area cut highlighted in red circle.



(d) ^{14}Be reconstruction of beam angle on target.

Figure 3.10: Beam position and angle reconstruction on target for ^{12}Be beam (a, b) and ^{14}Be beam (c, d).

Table 3.1: Beam spot characteristics.

Beam	$\sigma_x(mm)$	$\sigma_y(mm)$	$\sigma(\theta_x)(deg)$	$\sigma(\theta_y)(deg)$
^{12}Be	7.0	4.5	0.18	0.50
^{14}Be	8.0	10.5	0.24	0.31

3.2.4 Position resolution

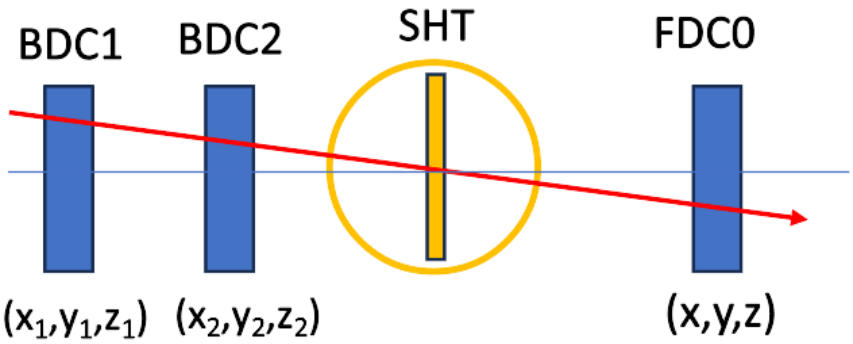


Figure 3.11: Scheme of BDC1, BDC2, SHT, and FDC0 to illustrate reconstruction of beam position on target.

In order to confirm the resolution of the reconstruction of the beam spot, the 3D positions of BDC1, and FDC0 are used to interpolate the position at BDC2. As shown in Fig. 3.11, assuming the position at BDC1 is (x_1, y_1, z_1), the position at BDC2 is (x_2, y_2, z_2), and the position at FDC0 is (x, y, z), then the position (x_2, y_2) can be interpolated using x, y, z, x_1, y_1, z_1, and z_2. The interpolated position can then be compared to the measured position. Considering the interpolated x value of BDC2 as X_2 and measured value as X_{BDC2} then

$$X_2 = X_{BDC1} + \frac{Z_{BDC2} - Z_{BDC1}}{Z_{FDC0} - Z_{BDC1}}(X_{FDC0} - X_{BDC1}) \tag{3.24}$$

and defining the constant C as ($C = \frac{Z_{BDC2}-Z_{BDC1}}{Z_{FDC0}-Z_{BDC1}}$) and subtracting the interpolated position from the measured position then equation 3.24 becomes

$$X_2 - X_{BDC2} = (1 - C)X_{BDC1} + CX_{FDC0} - X_{BDC2} \tag{3.25}$$

then the position resolution can be determined using error propagation of equation 3.25 using

$$\sigma^2(X_2) = (1 - C)^2\sigma^2(X_{BDC1}) + C^2\sigma^2(X_{FDC0}) + (-1)^2\sigma^2(X_{BDC2}) \tag{3.26}$$

If we assume constant position resolution (σ_{DC}) for BDC1, BDC2, and FDC0, then the position resolution would be

$$\sigma_{DC} = \frac{\sigma(dX_{BDC2})}{\sqrt{(1-C)^2 + C^2 + 1}} \tag{3.27}$$

Figure 3.12 shows the difference between interpolated and measured values of BDC2 X (left) and Y(right). Both figures were fitted with a Gaussian function and the sigma obtained was then used in equation 3.27 where the X and Y resolution values were $\sigma_{DC}(X)$ = 347.94 um and $\sigma_{DC}(Y)$ = 344.05 um respectively. The drawbacks of using the interpolation method to estimate the position resolution of the drift chambers are that it does not take into account the angular straggling in the different materials as well as the fact that BDC1/2 were tuned to a different Z value than that of FDC0 because they are expected to detect different nuclei (Be and He respectively).

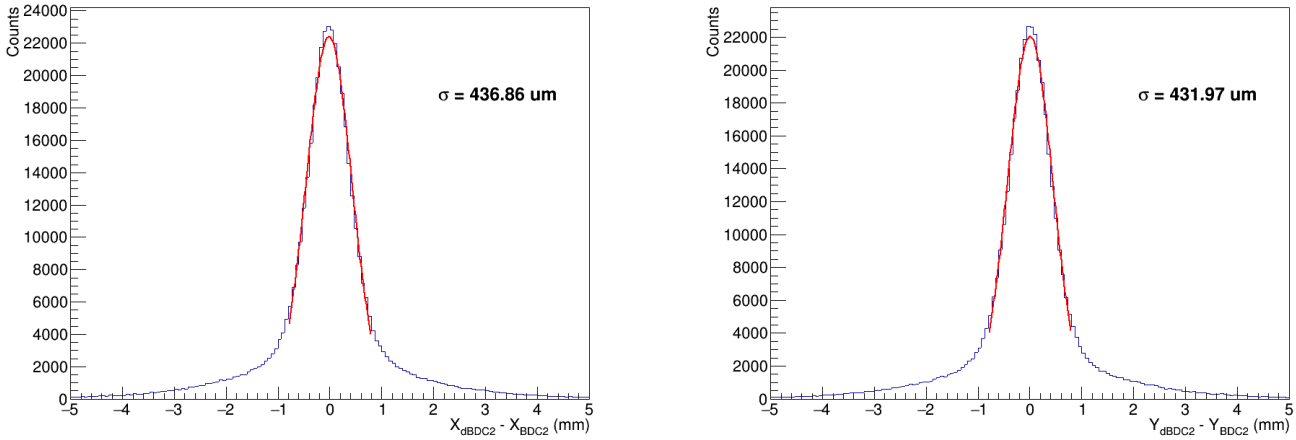


Figure 3.12: Difference between measured and interpolated BDC2 position. BDC2 X(left). BDC2 Y(right).

3.3 ESPRI

The energy and scattering angle of the recoil proton can be determined using the ESPRI setup. The RDC detects the position of the recoil particles while the plastic determines energy loss and ToF, and, eventually, the NaI(Tl) reconstructs the full energy thus providing four-momentum vectors of the recoil protons. The scattering angle was determined relative to the beam direction by performing rotations and translations on the plane of RDC. The total energy of the recoil proton was determined initially using plastic and NaI(Tl) scintillators, then ToF from the plastic scintillator was used as a secondary method.

The punchthrough energy of the plastic is 24 MeV, corresponding to the minimum energy to measure the proton energy using the NaI(Tl). In the previous work [51], the protons of interest were the high energy protons, accordingly, using the first method to determine the proton energy was sufficient. However, for this work, including the low energy protons was essential as it would significantly increase the statistics by improving the geometrical efficiency with respect to NaI(Tl) bars. In order to improve the resolution of the energy deduced from ToF, a correction was tested and implemented to the plastic ToF. In this section, both methods of energy determination will be discussed, highlighting previous work improvements in addition to this work's improvements alongside the particle identification using $\Delta E - E$ and $\Delta E - ToF$.

3.3.1 RDC calibration

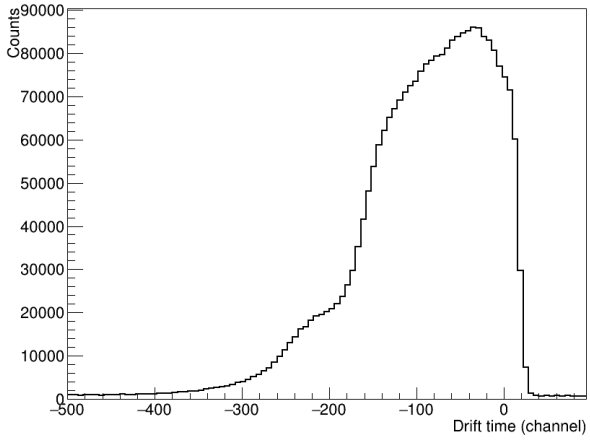
The structure of the RDC is very similar to that of the beamline drift chamber with minor differences being the number of wires and channels utilized as well as a larger drift length. However, a major difference between the two is the fact that the uniform drift length distribution assumption (section 3.2) is no longer valid. This is due to the proton scattering angle being related to the physics reaction channels. Accordingly, the space-time conversion function used was that of a high order polynomial as shown in equation 3.28. This polynomial was determined during a previous experiment.

$$DL = p_0\sqrt{TDC} + p_1 TDC + p_2 TDC^2 + p_3 TDC^3 + p_4 TDC^4 \tag{3.28}$$

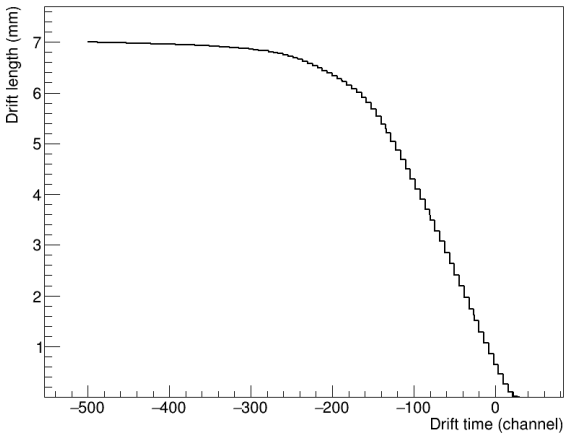
Figure 3.13 shows the typical drift time of RDC and the corresponding drift length using the STC.

The same tracking algorithm was used for the RDC as the one used for BDC and FDC0 where the track with least χ^2 was selected. The residue of the reconstruction for the right arm of ESPRI can be seen in Fig. 3.14. The sigma of the RDC residue was found to be 100 um with a relatively narrow peak and large tail extending from both sides.

In order to determine the scattering angle of the recoil protons, a position transformation of the RDC was done using the position of the target in order to calculate the scattering angle with respect to the beam in a similar manner to formulae 3.22 and 3.23.

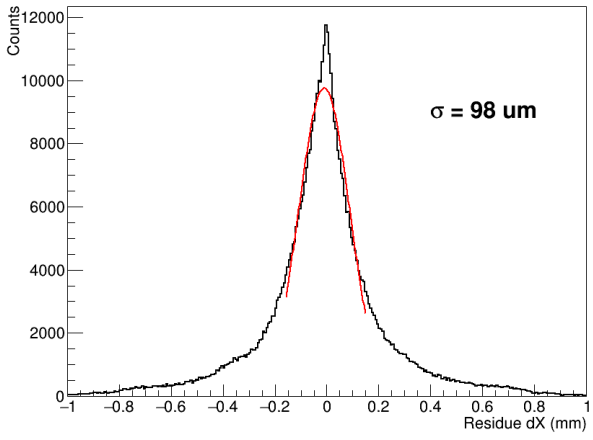


(a) RDC TDC

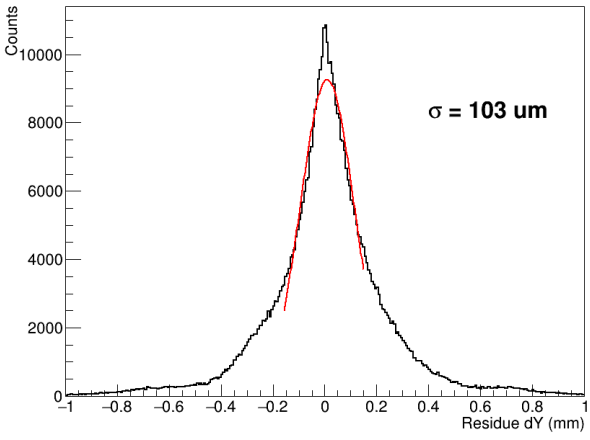


(b) RDC space-time conversion

Figure 3.13: Example of RDC STC.



(a) RDC X layers residue



(b) RDC Y layers residue

Figure 3.14: Right arm ESPRI RDC residue.

3.3.2 NaI(Tl) energy calibration

The calibration of the NaI(Tl) scintillation detectors used to detect the recoil protons was done using the inelastic scattering reaction of ^{10,12,14}Be(p, p') while utilizing different excitation energies. Firstly, the kinematic line of the proton energy vs. proton angle was determined for the elastic scattering and inelastic scattering with different excitation energies considering energy loss through different materials using Lise++ kinematic calculator as shown in Fig. 3.15.

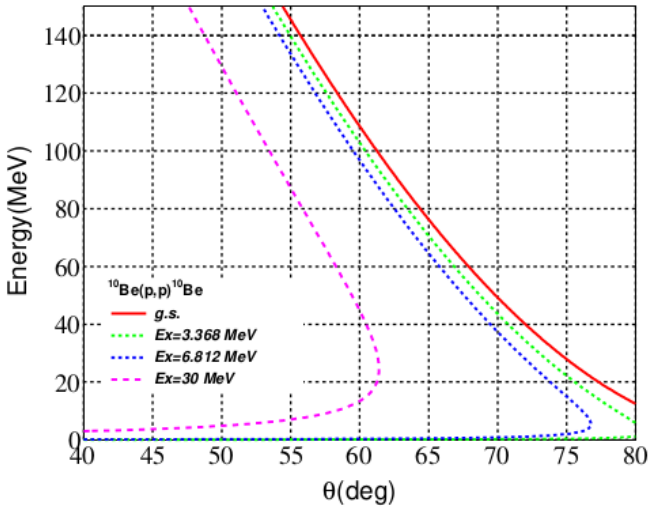


Figure 3.15: ^{10}Be proton energy vs angle from Lise++ (figure from [51]).

Afterwards, the proton angle was calculated using the RDC such that each event correlates to an angle. Using the energy-angle correspondence from the kinematic line, several points of ADC vs. energy were chosen by considering several bins in angle using the ADC vs. angle 2D spectrum and determining the mean value of the projection of each angle (Fig. 3.16 [left]). Finally, the points of the ADC vs. energy spectrum were fitted using the Birks formula (formula 3.29)[63] (α and β are constants) and the energy of the NaI(Tl) was calibrated (Fig. 3.16 [right]).

$$E_{NaI} = \frac{\alpha ADC}{1 + \beta ADC} \tag{3.29}$$

This calibration process was repeated for each bar and each beam setting due to the effect of the magnetic field of the SAMURAI magnet on the PMTs of the NaI(Tl) detectors. In order to reconstruct the total energy of the protons, the energy loss of protons determined by the plastic scintillators was disregarded

due to their poor energy resolution. Instead, the energy loss in a plastic scintillator material was calculated and accounted for.

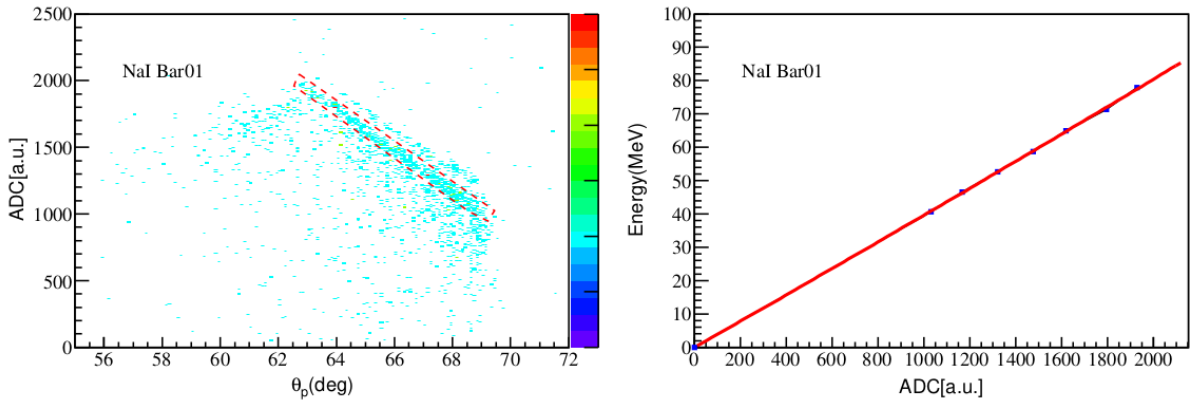


Figure 3.16: NaI(Tl) ADC vs proton angle (left); NaI(Tl) energy calibration fit (right) figures obtained from [51].

3.3.3 Plastic time-of-flight

The plastics in ESPRI were used for particle identification and the determination of proton energy by ToF. This increases geometrical efficiency of protons with respect to using NaI(Tl) detectors as it permits the detection of protons that would otherwise end up passing through the gaps between the NaI(Tl) bars. More importantly, it recovers events for which protons stop in the plastic detector which is placed before the NaI(Tl) detectors.

As mentioned in chapter 2, each plastic detector of ESPRI was coupled to two PMTs, one from above and the other from below. However, during the experiment, there were some issues with the upper PMT whose data were not valid for most events. To solve this problem, a procedure comparing the time obtained by the upper and lower PMT is utilized. It selects the upper PMT only in the condition that the lower PMT signal is not noisy and the upper PMT is working well, otherwise, only the lower PMT is used for the timing.

3.3.3.1 Time calibration

In a first step, we recall the initial time calibration performed by [51]. The time calibration of the ESPRI plastic utilizes information about the trajectory and energy of the protons from the RDC and NaI(Tl) respectively. To calibrate the ESPRI plastic ToF and determine the ToF of the protons, the following

equation is employed.

$$ToF_p = \alpha TDC + \beta + T_{pos} + T_{slew} \tag{3.30}$$

Where α is a term for the conversion of TDC from channel to ns ($\alpha = 0.025\ ns/channel$), β is an offset calculated depending on energy of proton measured by the NaI(Tl), T_{pos} is the position correction determined using the RDC position, and T_{slew} is the slew correction treated in the same way as in section 3.1.

The total proton energy reconstructed from NaI(Tl) can be used as a time reference to check the corrections done to the ToF. The proton energy can be related to its ToF using the following formulae

$$T_p = (\gamma - 1)M_p \tag{3.31}$$

$$\gamma = \sqrt{\frac{1}{1-\beta^2}} \tag{3.32}$$

$$\beta = \frac{L}{cToF_p} \tag{3.33}$$

$$ToF_p = \frac{L}{c\beta} \tag{3.34}$$

Where T_p is the proton kinetic energy, γ is the Lorentz factor, β is the velocity, and L is the flight length between the target and the plastic. L is determined by extrapolating the trajectory from RDC to the plastic.

3.3.3.1.1 Position correction As mentioned above, during the experiment the upper PMT was not functioning properly, hence, there is a notable position dependence for the ToF. This dependence can be seen in Fig. 3.17 (left), the red line shows the deviation of ToF depending on the position that was obtained from the RDC. The segmentation in the 2D plot arises from the gaps between the NaI(Tl) bars. The correction to the ToF was done using the formula 3.35 where the constants were obtained using a linear fit of the 2D histogram of Fig. 3.17 (left) and Fig. 3.17 (right) show the same plot after the correction. Figure 3.18 shows ΔT before and after the correction.

$$\Delta T = ToF_p^{NaI} - (\alpha TDC + \beta + aY_{RDC} + b) \tag{3.35}$$

Where **a** and **b** are obtained from the linear fit and $\mathbf{ToF_p^{NaI}}$ is deduced from the calibrated NaI(Tl) energy (equations 3.31-3.34).

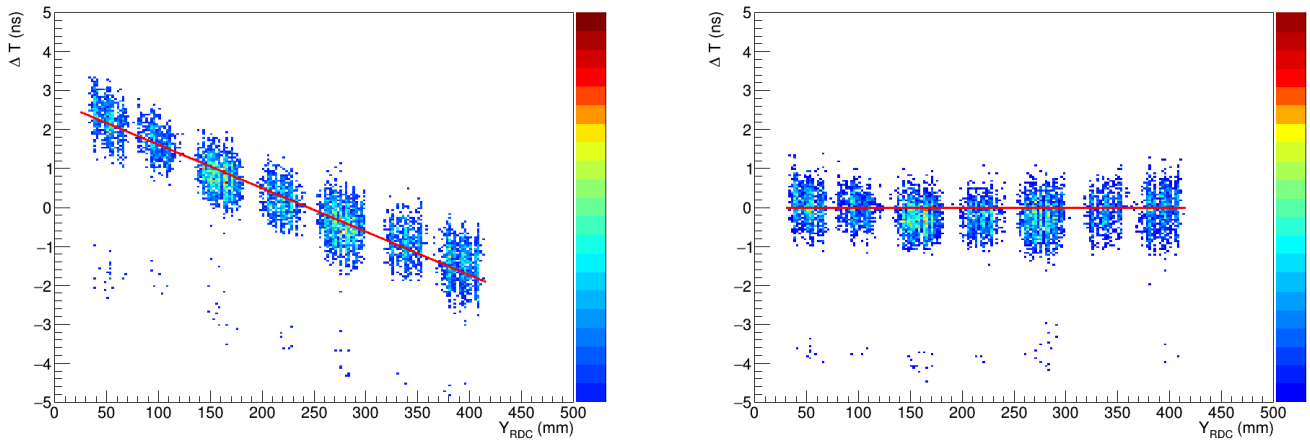


Figure 3.17: ESPRI plastic ΔY vs ΔT plot before (left) and after (right) position correction.

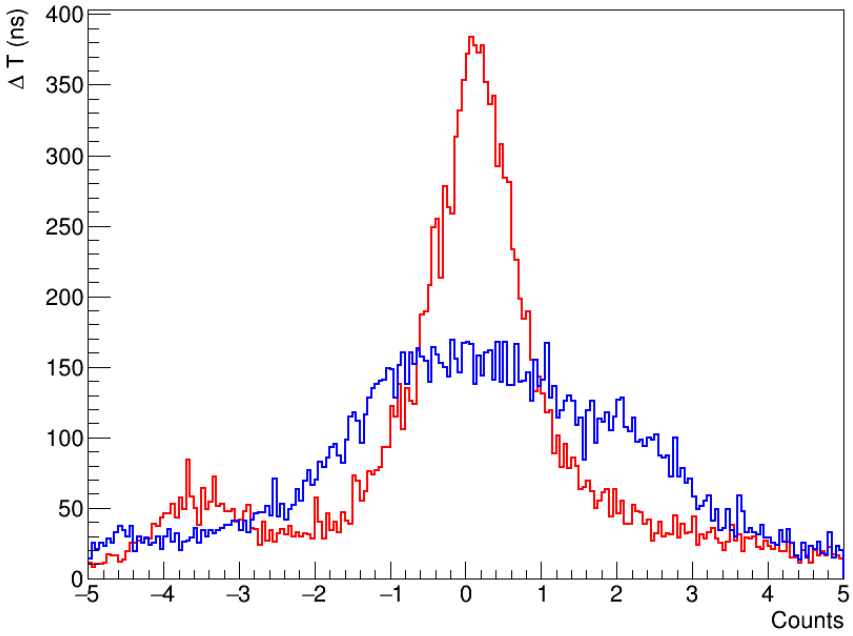


Figure 3.18: ESPRI plastic ΔT plot before (blue) and after (red) position correction.

3.3.3.1.2 Slew correction As in section 3.1, a time walk correction is an important part of the ToF calibration of the plastic. Figure 3.19 (left) shows the charge dependence of the time signal of the plastic. Although the charge dependence is small compared to the position dependence, a time walk correction was done as shown in Fig. 3.19 (right). Figure 3.20 shows ΔT before and after the correction.

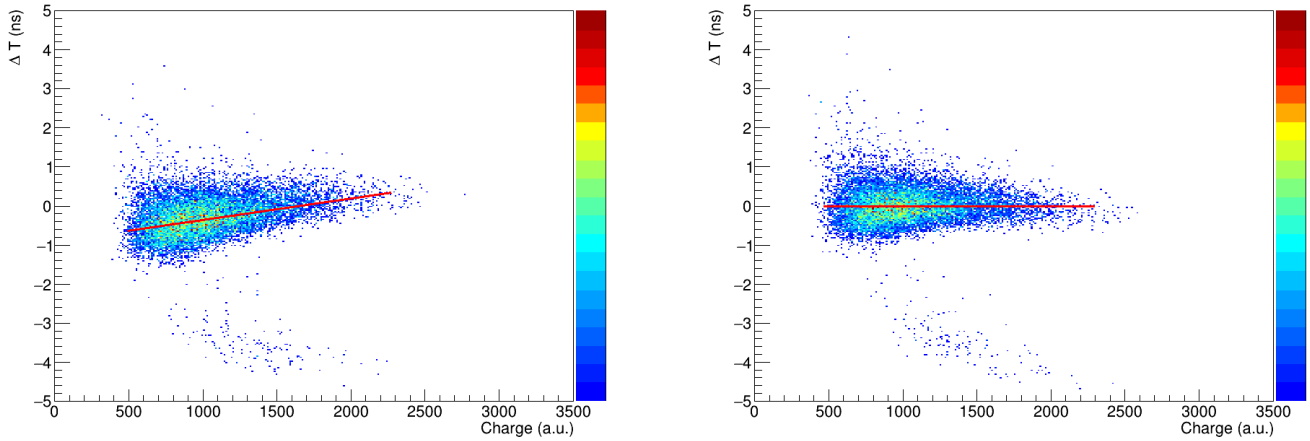


Figure 3.19: ESPRI plastic ΔT vs Charge plot before (left) and after (right) time walk correction.

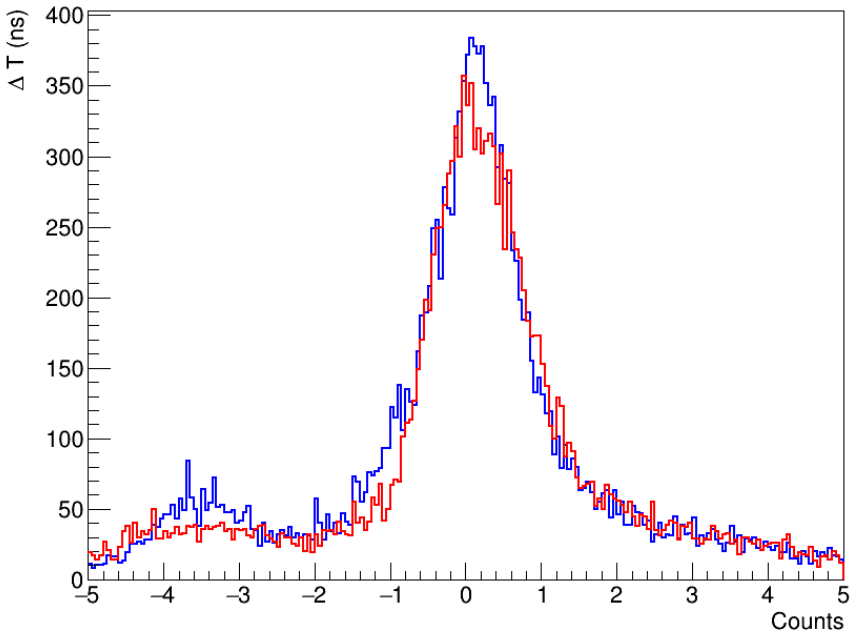


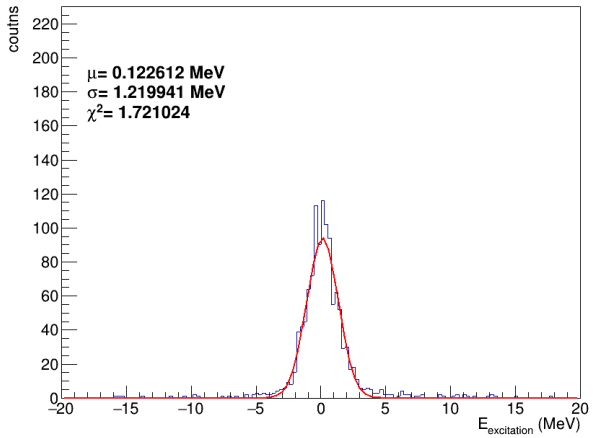
Figure 3.20: ESPRI plastic ΔT plot before (blue) and after (red) slew correction.

3.3.3.2 Excitation energy

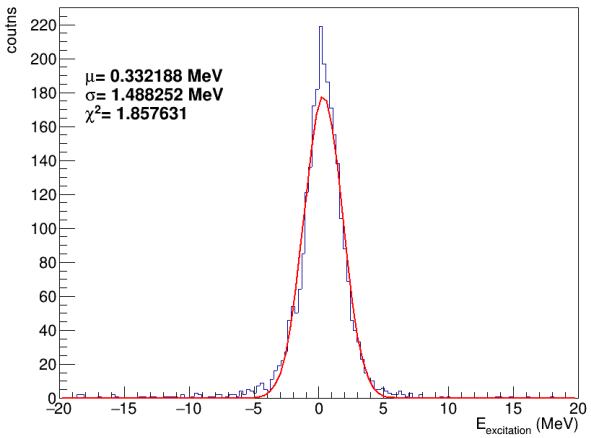
In order to improve the time-of-flight calibration, we checked its correlation with the excitation energy of ^{8}He from the ^{12}Be$(p, p\alpha)$ reaction. This reaction was chosen because in ^{8}He, only the ground state is bound. Consequently, when selecting the ^{8}He residue in hodoscope, there is only one state populated. The excitation energy of ^{8}He was calculated using the conservation of energy and momentum.

$$E_{^{12}\mathrm{Be}} + E_H = E_p + E_\alpha + E_{^{8}\mathrm{He}} \tag{3.36}$$

$$\overrightarrow{P}_{^{12}\mathrm{Be}} = \overrightarrow{P_p} + \overrightarrow{P_\alpha} + \overrightarrow{P}_{^{8}\mathrm{He}} \tag{3.37}$$



(a) ^{12}Be beam ^{8}He excitation energy using proton energy from NaI(Tl).



(b) ^{12}Be beam ^{8}He excitation energy using proton energy from plastic ToF.

Figure 3.21

Where E_i, and $\overrightarrow{P_i}$ are the energy and momentum vector of each component i. By combining these formulae, the momentum and energy of ^{8}He can be obtained with $cos\theta_{p-\alpha}$ expressed in formula 3.40.

$$P_{^{8}\mathrm{He}} = \sqrt{P^2_{^{12}\mathrm{Be}} + P^2_p + P^2_\alpha - 2P_{^{12}\mathrm{Be}}P_p cos\theta_p - 2P_{^{12}\mathrm{Be}}P_\alpha cos\theta_\alpha + 2P_pP_\alpha cos\theta_{p-\alpha}} \tag{3.38}$$

$$E_{^{8}\mathrm{He}} = E_{^{12}\mathrm{Be}} + E_H - E_p - E_\alpha \tag{3.39}$$

$$cos\theta_{p-\alpha} = cos\theta_p \cdot cos\theta_\alpha + sin\theta_p \cdot sin\theta_\alpha \cdot cos(\phi_\alpha - \phi_p) \tag{3.40}$$

Where θ and ϕ are the polar and azimuthal angles respectively and E and P are the energy and momentum

respectively. Finally, the excitation energy in the residue can be expressed by equation 3.41.

$$E_{ex.}(^{8}\mathrm{He}) = \sqrt{E^2_{^{8}\mathrm{He}} - P^2_{^{8}\mathrm{He}}} - m_{^{8}\mathrm{He}_{g.s}} \tag{3.41}$$

Where $m_{^{8}\mathrm{He}}$ is the rest mass of ^{8}He. Figure 3.21a shows the excitation energy of ^{8}He using proton energy from NaI(Tl) while Fig. 3.21b shows the excitation energy using plastic ToF. As can be seen, the resolution using NaI(Tl) is better than the one using ToF, however, the statistics is doubled when using proton energy from plastic ToF. We now discuss the implementation of an additional ToF correction.

3.3.3.3 Time of flight correction

When plotting the correlation between the excitation energy of ^{8}He from the ^{12}Be beam with the energy of the recoil proton deduced from the ToF as shown in Fig. 3.22 (left), it can be seen that at lower energies, there is a deviation in the excitation energy from the expected value of 0 MeV.

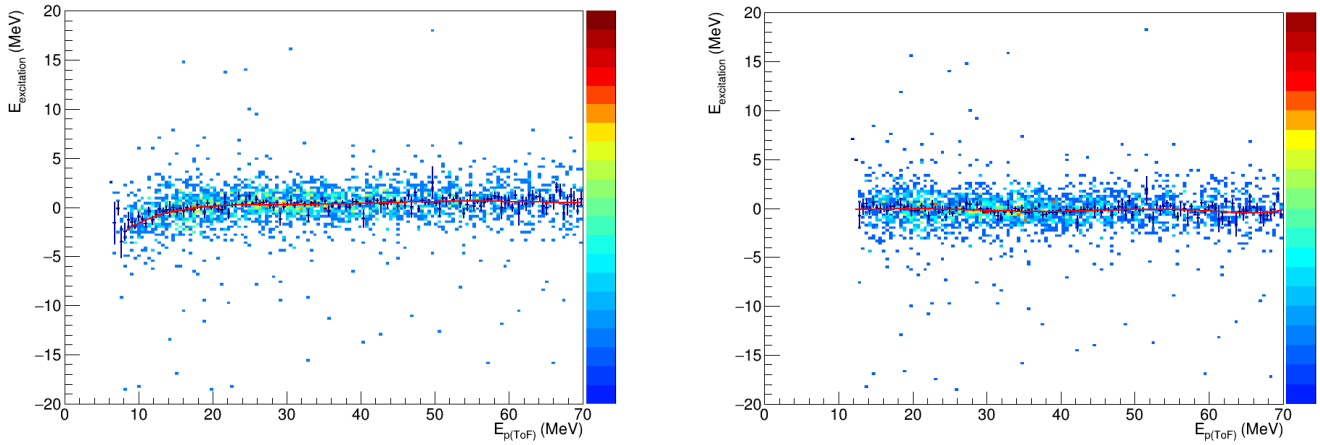


Figure 3.22: ^{12}Be beam ^{8}He excitation energy vs. proton energy deduced from ToF pre ToF correction (left), and post ToF correction (right).

In order to correct for this deviation, a value for the ToF, that was non-dependent on the plastic ToF, was calculated using other variables such as the scattering angles of the alpha, proton, and residue in addition to the energy of the alpha. Afterwards, considering that the vector of momentum of the beam is the sum of the proton, alpha, and residue momentum vector, then using the conservation of momentum, a value of

momentum for the proton is calculated using the following formulae

$$0 = P_p sin\theta_p cos\phi_p + P_\alpha sin\theta_\alpha cos\phi_\alpha + P_{res} sin\theta_{res} cos\phi_{res} \tag{3.42}$$

$$0 = P_p sin\theta_p sin\phi_p + P_\alpha sin\theta_\alpha sin\phi_\alpha + P_{res} sin\theta_{res} sin\phi_{res} \tag{3.43}$$

$$P_{beam} = P_p cos\theta_p + P_\alpha cos\theta_\alpha + P_{res} cos\theta_{res} \tag{3.44}$$

Where P is the momentum, θ, ϕ are the polar and azimuthal angles. Since the scattering angles of the proton, alpha, and residue are set up with respect to the beam, then the beam momentum is only around the Z-axis. Then the momentum of the protons can be deduced from

$$P_p = \frac{P_{beam} + P_\alpha(\frac{B}{C} cos\theta_{res} - cos_\alpha)}{cos\theta_p - \frac{A}{C} cos\theta_{res}} \tag{3.45}$$

Where $A = sin\theta_p cos\phi_p$, $B = sin\theta_\alpha cos\phi_\alpha$, and $C = sin\theta_{res} cos\phi_{res}$. Afterwards, using 3.45, the kinetic energy of the proton can be obtained through

$$T_p = \sqrt{P_p^2 + m_p^2} - m_p \tag{3.46}$$

Finally, the ToF can be deduced from formula (3.34)

Figure 3.23 shows the proton ToF deduced from formula 3.34 with that measured by the plastic with a 45° line in green and polynomial fit in red with different energies highlighted with black dotted lines (in MeV). The deviation seen at ToF corresponding to energies smaller than 25 MeV indicates the need for correction. This is somewhat expected as these events were not considered in the previous analysis. This deviation was fitted with multiple degrees of polynomial functions to check which correction provided the best improvement in the energy resolution. It was found that the best improvement was obtained by a second degree polynomial.

Figure 3.22(right) shows the effect of the ToF correction. Figures 3.24a and 3.24b show a comparison between the excitation energy spectrum of ^{8}He with a Gaussian fit before and after the ToF correction respectively. A slight improvement to the sigma can be observed with the mean value closer to the

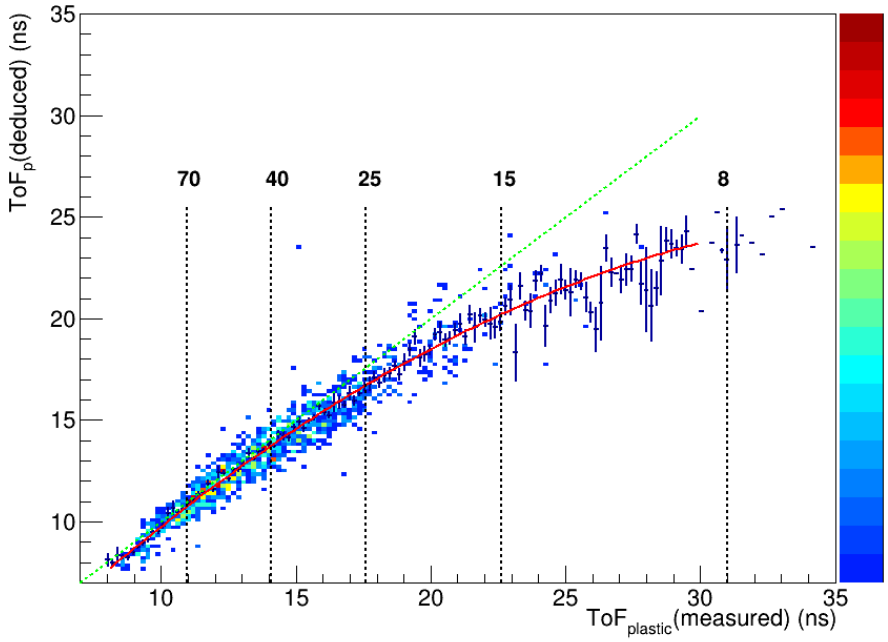
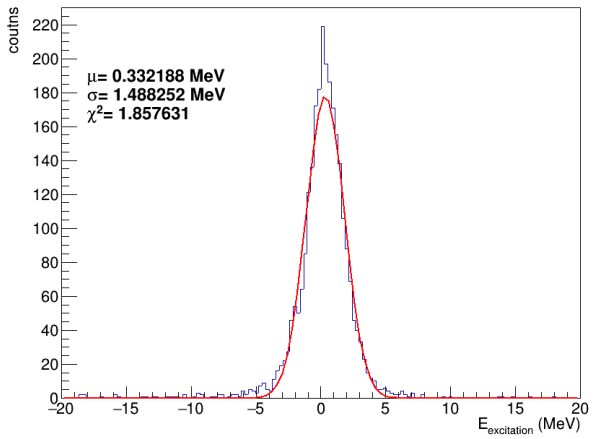
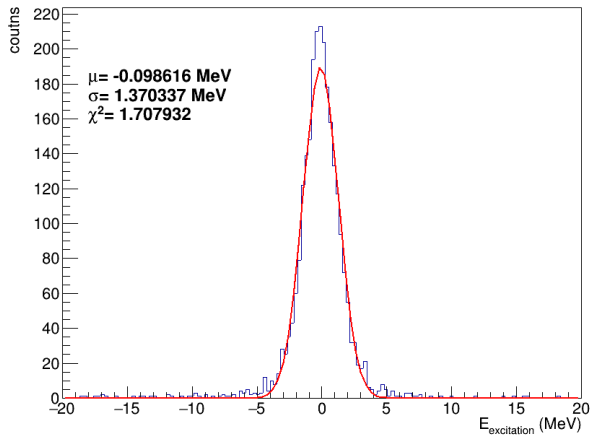


Figure 3.23: Proton ToF deduced vs measured by the plastic with fit (red), 45° line (green) and black dotted lines corresponding to proton energy in MeV of different ToF.



(a) ^{12}Be beam ^{8}He excitation energy pre ToF correction.



(b) ^{12}Be beam ^{8}He excitation energy post ToF correction.

Figure 3.24

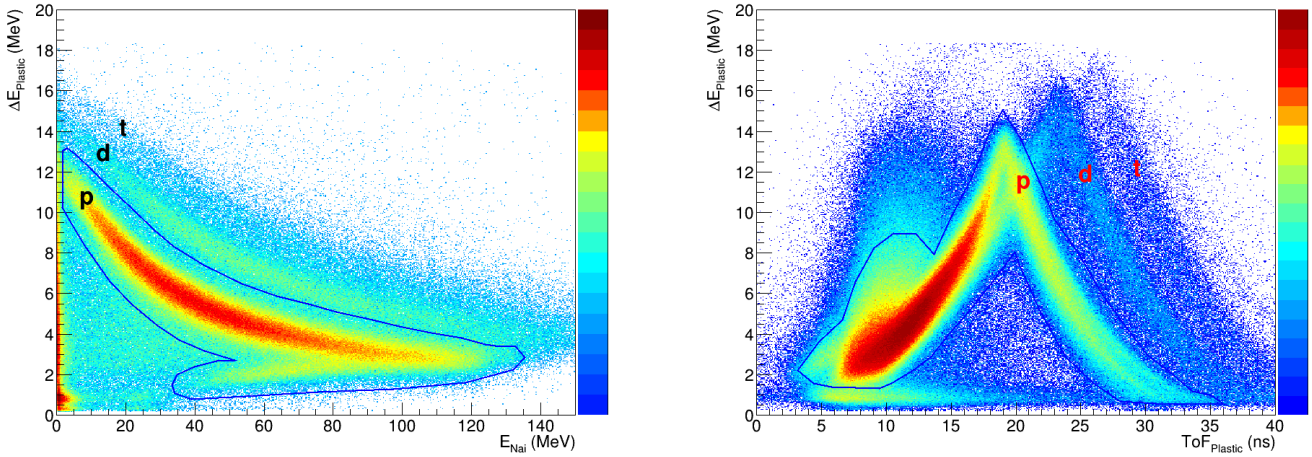
expected value. The sigma value using the corrected ToF is still larger than the case using NaI(Tl), however, doubling the statistics and recovering lower energy protons is worth the reduction in resolution.

3.3.3.4 ESPRI particle identification

The particle identification for ESPRI using $\Delta E - E$ with the help of the NaI(Tl) energy and $\Delta E - ToF$ using the plastic ToF is presented in figures 3.25a and 3.25b respectively. For the case of $\Delta E - E$, the energy of the plastic was not used to determine the total energy **E**. This is due to the low energy resolution for the high energy protons, instead, the energy loss in all the materials between the target and the NaI(Tl) such as the windows of the target chamber, the wedge and the plastic scintillator was calculated using energy loss tables and the trajectory of the proton in the different material (determining the effective thickness), then these values were added to the energy detected by the NaI(Tl) to determine the total energy of the proton. As for the PID using $\Delta E - ToF$, the energy loss of the plastic as well as ToF between the target and the plastic were used for the PID. The ToF between the target and the plastic was determined by subtracting the ToF of the beam from F13 to the target. Figure 3.25a shows a clear separation between the protons, deuterons, and tritons and the proton cut is highlighted in blue. Figure 3.25b shows the $\Delta E - ToF$ PID, it can be seen that at large value of ToF corresponding to low proton energy, there is a clear discrimination between the protons deuterons and tritons, however, at lower ToF, the events from each species cannot be separated; additionally, some events with larger energy loss in the plastic form a bump shape in the low ToF regime. The events inside this bump correspond to events in the physical region in the $\Delta E - E$ plot with a majority of protons and a few deuterons and tritons. As for the deuterons and tritons contained in the cut highlighted in blue, ^{8}He excitation energy spectra presented in Fig. 3.21b indicate that they do not contribute to the $(p, p\alpha)$ channel. In the following, the proton PID is implemented using the blue cut of Fig. 3.25b.

3.4 Telescope

The alpha nuclei of the $(p, p\alpha)$ reaction were detected using Telescope which determined their four-momentum. The position of the alpha was determined using the DSSD detector which provided the 2D



(a) ^{14}Be $\Delta E - E$ PID plot (b) ^{14}Be $\Delta E - ToF$ PID plot

Figure 3.25: ^{14}Be ESPRI PID plots.

position depending on the strips fired in the front and back of the detector. Additionally, the energy lost in the DSSD was measured to provide the ΔE for the $\Delta E - E$ particle identification as well as total energy reconstruction of the alpha. An array of CsI(Tl) detectors placed downstream from the DSSD was used for the full energy determination of the alpha nuclei as well as the particle identification. The Telescope calibration was done using two de-focused secondary alpha beams of energies 157 MeV/u and 121 MeV/u respectively. The detectors were placed along the beamline during the calibration process to intercept the alpha beam. Table 3.2 highlights the energy loss in each detector type for each alpha beam setting.

Table 3.2: Telescope energy loss for each beam setting

Beam	ΔE_{DSSD} (MeV)	E_{CsI} (MeV)
157.52 MeV/u	7.02	495.04
121.06 MeV/u	9.79	311.02

3.4.1 DSSD energy calibration

The DSSD calibration is done by using the two alpha beam settings for the energy calibration of the ADC of each strip. As the active area of the DSSD exceeds the target cell by a factor of approximately 9, less than half of the DSSD strips can be irradiated by the de-focused alpha beam. This problem can be solved by invoking the unique characteristics of the DSSD detector using the so-called self-calibration method

(SCM) [66]. The basic principle behind this method is that as a charged particle passes through the DSSD, the same amount of energy is deposited in both front and back strips as they are fired simultaneously. Suppose a charged particle passes through a pixel **(i,r)** where **i** is a front strip and **r** is a back strip as shown in Fig. 3.26, assuming linearity of pre-amplifiers, there is a correlation between the amplitude of the signal from the front strip and the back strip as expressed in equation 3.47 referenced to [66].

$$R_{i,r} = a_{i,r} + b_{i,r}F_{i,r} \tag{3.47}$$

Where $a_{i,r}$, $b_{i,r}$ are constants for stable signal processing and $F_{i,r}$, $R_{i,r}$ are the amplitudes of the signal of front strip and back strip respectively. This leads to a situation where all back strips can be aligned to a single front strip and vice versa.

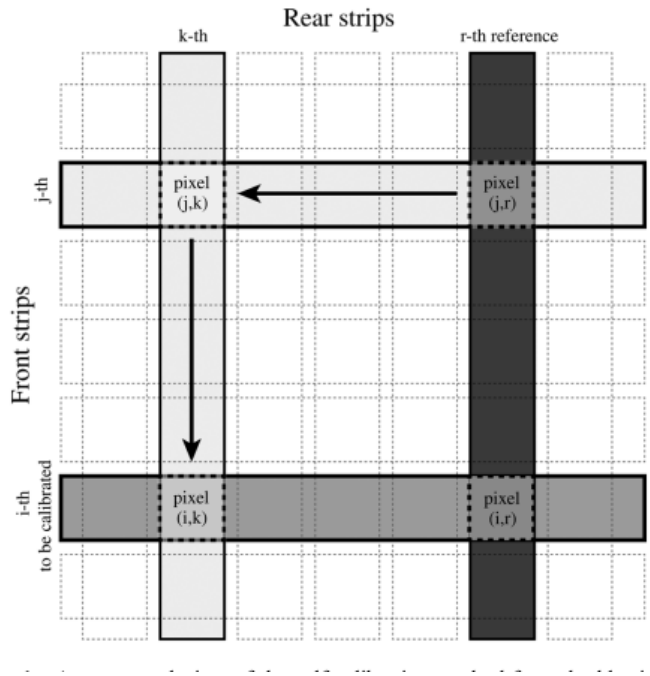


Figure 3.26: Illustration of DSSD SCM figure obtained from [66].

The alignment of the strips was done using the SCM by normalizing a uniform gain for all 32 front strips using a single perpendicular back strip such that each front strip and the back strip have been hit by the same particle simultaneously. Figure 3.27 illustrates the ADC of the 14th front strip and 13th back strip, before (left) and after (right) the alignment.

As the gain of all the strips of the DSSD are aligned using the SCM, the calibration in energy can be done using the energy deposited in the DSSD using the two energy settings of the alpha calibration beam

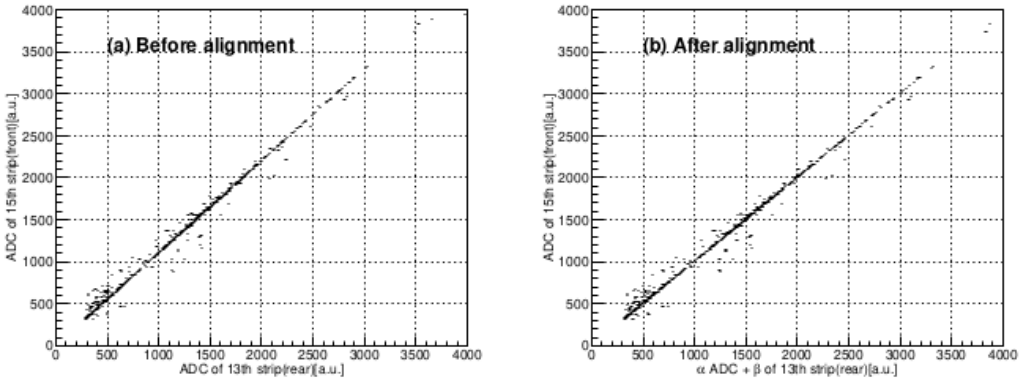


Figure 3.27: ADC correlation between 13th back strip and 14th front strip before (left) and after (right) alignment figures obtained from [51].

mentioned in table 3.2. Figure 3.28 illustrates the two energy calibration curve and the corresponding energy deposited in the DSSD after calibration.

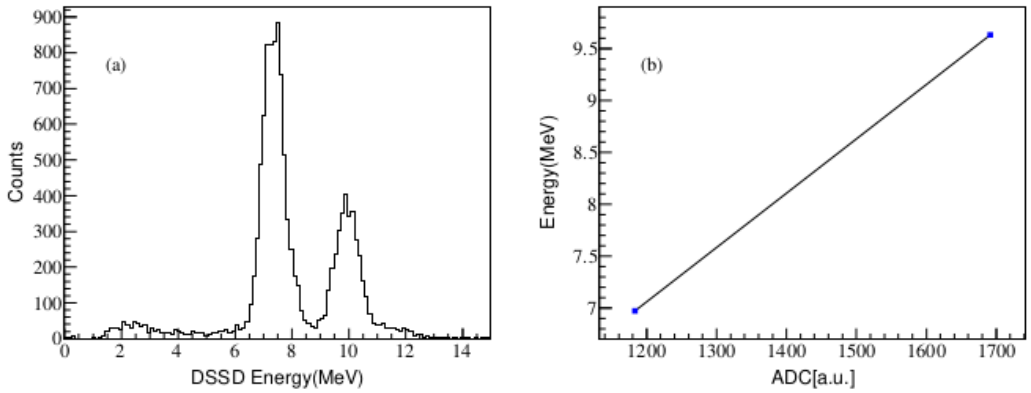


Figure 3.28: DSSD energy spectrum (left) and corresponding calibration plot with two points (right) figures obtained from [51].

3.4.2 CsI(Tl) energy calibration

The calibration of the CsI(Tl) is essential for the full energy reconstruction of the alpha particles as full energy absorption of these alphas is done by the CsI(Tl). Due to the unique composition of the target frame, the energy loss in the target and its frame can vary depending on five different cases. Figure 3.29 illustrates different scenarios of the alpha crossing the target which leads to different energy loss that manifests as multiple peaks in the raw ADC spectrum of the CsI(Tl).

When the alpha passes through the target frame, depending on which case takes place, it can pass



Figure 3.29: SHT copper frame interactions with beam.

through 1mm, 2mm, or 1mm of copper corresponding to front shield, target frame, and back shield respectively. This leads to attenuation by 0-4 mm of copper depending on how many layers of the frame it passes through. Table 3.3 highlights the different cases with thickness of copper encountered and energy of alpha calculated by Lise++. The calibration of the CsI(Tl) was done using the energies detected by

Table 3.3: Telescope CsI(Tl) energy for each case.

Beam	Case	Front	Target	Back	Total Cu (mm)	E_{CsI} (MeV)
157.52 MeV/u	1	X	X	X	0	500.21
	2	✓	X	X	1	485.27
	3	X	✓	X	2	469.97
	4	X	✓	✓	3	454.34
	5	✓	✓	✓	4	438.29
121.06 MeV/u	1	X	X	X	0	318.27
	2	✓	X	X	1	297.24
	3	X	✓	X	2	275.03
	4	X	✓	✓	3	251.38
	5	✓	✓	✓	4	225.87

CsI(Tl) due to the alpha attenuation by the target frame in both beam settings. Each peak was fitted to determine the mean value and correlated to a specific ADC value and as in the case of the NaI(Tl), the Birks' formula (equation 3.29) was used to fit each CsI(Tl) crystal individually. Figure 3.30 (left) shows the energy calibration spectrum using Birks' formula for different crystals (names defined in section 2.6) while Fig. 3.30 (right) shows the corresponding CsI(Tl) energy spectra. It can be noted that due to the long range of high energy alpha particles ~ 500 MeV, which has a range of 4.5 cm in CsI(Tl), the high energy peaks appear to be broader than the low energy peaks. This effect is more pronounced in the Type 2 LL crystal as its length is 5 cm.

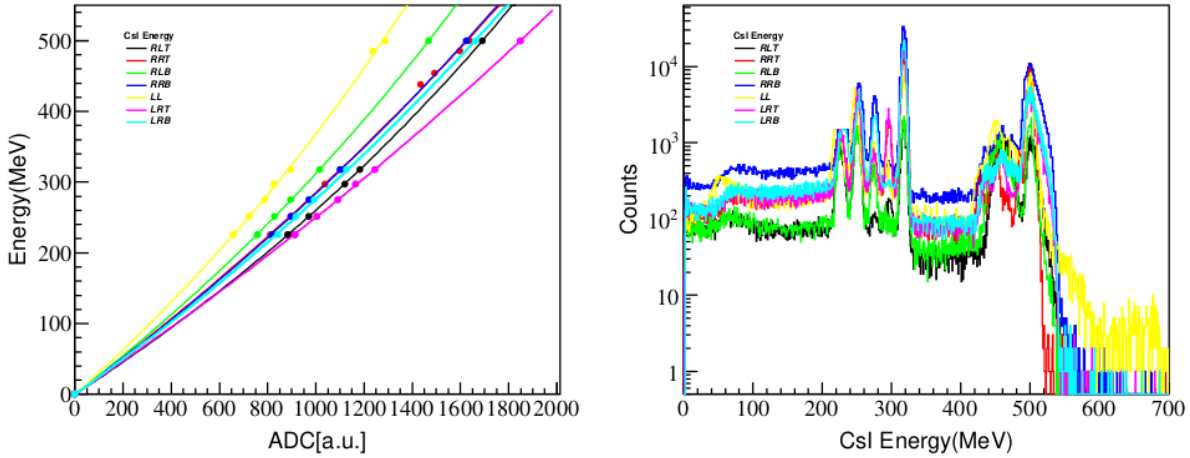


Figure 3.30: Telescope CsI(Tl) calibration (left) and energy spectrum (right) figures obtained from [51].

3.4.3 Alpha particle identification

After the determination of the full energy of the alphas, the particle identification was done using the $\Delta E - E$ method. Figure 3.31 shows the clear identification and separation of ^{3}He, ^{4}He, and the alpha cut used is highlighted in red.

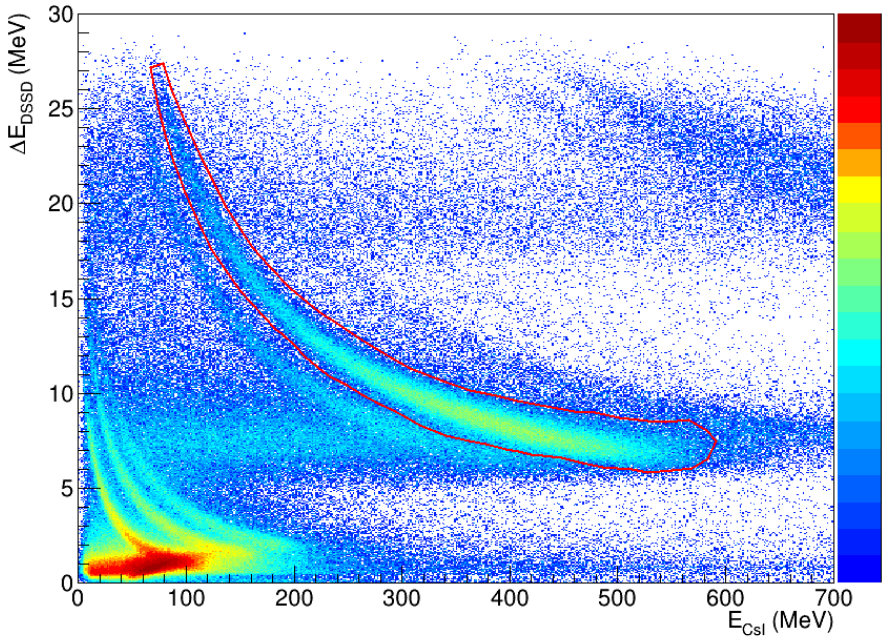


Figure 3.31: Telescope particle identification with alpha cut in red.

3.5 Hodoscope

The particle identification of the $(p, p\alpha)$ reaction residues was done by two Hodoscope walls made of plastic scintillators and placed downstream from the magnet and FDC2, named HODF and HODP, for the low $B\rho$ nuclei and high $B\rho$ nuclei respectively.

3.5.1 Particle identification

After the determination of the pedestals for the plastics electronics and conversion of the raw data, a calculation code was used to determine the positions of different species of nuclei on the $\Delta E - ToF$ plot and particle identification was done by comparing the two plots. Figure 3.32 demonstrates an example of the ^{14}Be beam residue particle identification for HODF and HODP respectively.

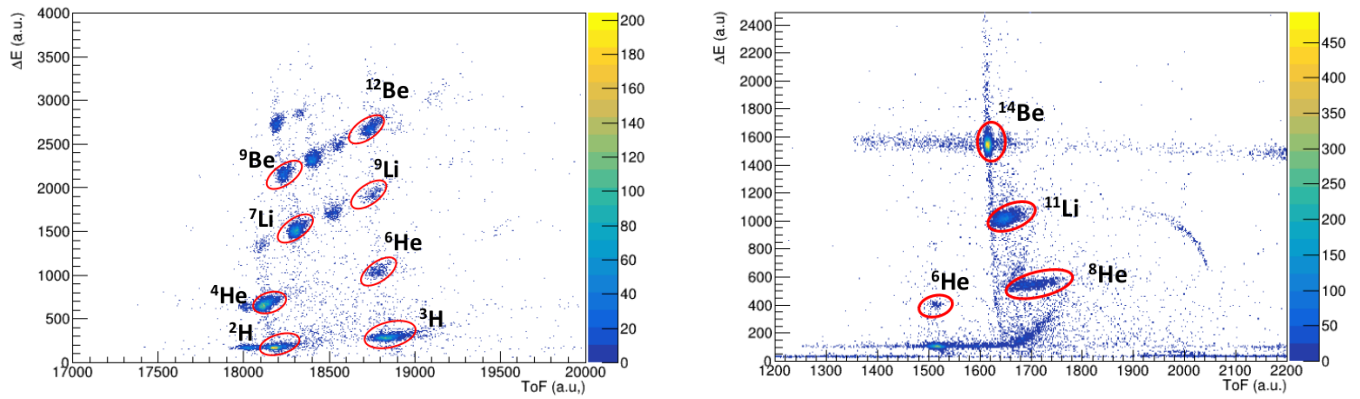


Figure 3.32: Hodoscope particle identification for a single bar. HODF(left), HODP(right).

3.6 Magnetic rigidity ($B\rho$) of decay alpha

In order to obtain the missing mass spectrum of the $6n$ system produced from the resonances in ^{10}He decaying through the alpha + $6n$ channel, the momentum of the beam velocity-like alpha particles is needed with sufficient precision. In this section, the method used to extract the $B\rho$ of the alpha residues detected using SAMURAI and its standard detectors will be presented starting from the detection of the decay alpha using FDC2 and then the subsequent extraction of the $B\rho$ and its resolution.

3.6.1 FDC2

The determination of the trajectory of residue nuclei after the SAMURAI magnet is essential for the $B\rho$ calculation. Although the track reconstruction of FDC2 shares the same principle as FDC0 (using the LSM), the implementation differs due to the extra complexity of FDC2 (X,U,V configuration of wire planes). The process of track construction starts by converting the TDC of each wire of FDC2 to a position using STC method. Figures 3.33a and 3.33b show a typical TDC spectrum of FDC2 layer and the corresponding STC of that layer respectively.

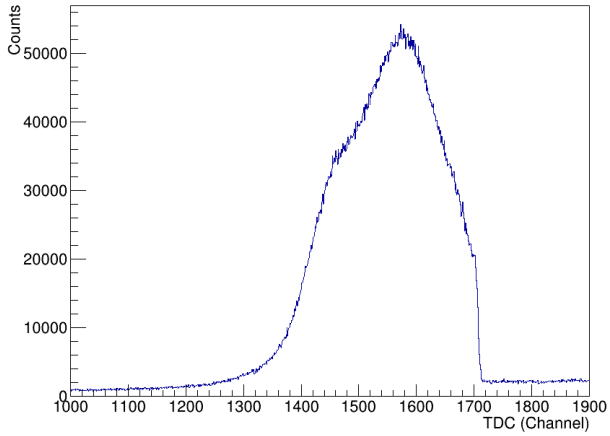
During the experiment, it was found that two U-layers (layers 11 and 12) did not function properly which can be seen in figures 3.33c and 3.33d, therefore, these two layers have been excluded from the analysis.

The (x,y) position of the FDC2 can be obtained through the X wire and the projection of the U and V wires on the X-Z, and Y-Z planes. The slope and intercept of the LSM in the X and Y directions can be determined using formula 3.48 where a and x_0 represent the slope and intercept in the X direction while b and y_0 represent the slope and intercept in the Y direction and p is an index for X, U, or V layers. A^{-1} can be defined in matrix 3.49.

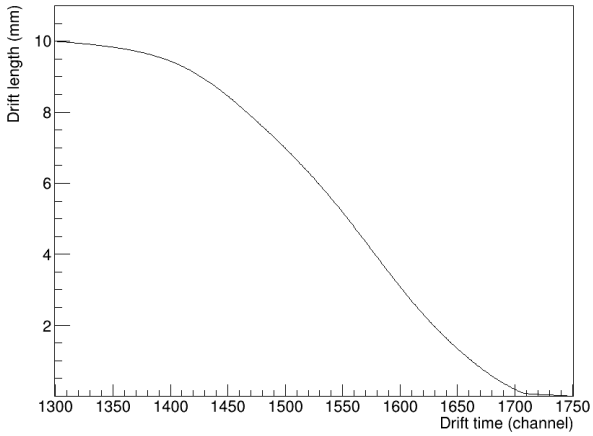
$$\begin{pmatrix} x_0 \\ a \\ y_0 \\ b \end{pmatrix} = A^{-1} \times \begin{pmatrix} \sum_{nhit_p} (\cos\theta_p) X \\ \sum_{nhit_p} (\cos\theta_p) ZX \\ \sum_{nhit_p} (\sin\theta_p) X \\ \sum_{nhit_p} (\sin\theta_p) ZX \end{pmatrix} \tag{3.48}$$

$$\begin{pmatrix} \sum_{nhit_p} (\frac{1}{2} + \frac{\cos 2\theta_p}{2}) & \sum_{nhit_p} (\frac{1}{2} + \frac{\cos 2\theta_p}{2})\, Z_p & \sum_{nhit_p} (\frac{\sin 2\theta_p}{2}) & \sum_{nhit_p} (\frac{\sin 2\theta_p}{2})\, Z_p \\ \sum_{nhit_p} (\frac{1}{2} + \frac{\cos 2\theta_p}{2})\, Z_p & \sum_{nhit_p} (\frac{1}{2} + \frac{\cos 2\theta_p}{2})\, Z_p^2 & \sum_{nhit_p} (\frac{\sin 2\theta_p}{2})\, Z_p & \sum_{nhit_p} (\frac{\sin 2\theta_p}{2})\, Z_p^2 \\ \sum_{nhit_p} (\frac{\sin 2\theta_p}{2}) & \sum_{nhit_p} (\frac{\sin 2\theta_p}{2})\, Z_p & \sum_{nhit_p} (\frac{1}{2} - \frac{\cos 2\theta_p}{2}) & \sum_{nhit_p} (\frac{1}{2} - \frac{\cos 2\theta_p}{2})\, Z_p \\ \sum_{nhit_p} (\frac{\sin 2\theta_p}{2})\, Z_p & \sum_{nhit_p} (\frac{\sin 2\theta_p}{2})\, Z_p^2 & \sum_{nhit_p} (\frac{1}{2} - \frac{\cos 2\theta_p}{2})\, Z_p & \sum_{nhit_p} (\frac{1}{2} - \frac{\cos 2\theta_p}{2})\, Z_p^2 \end{pmatrix} \tag{3.49}$$

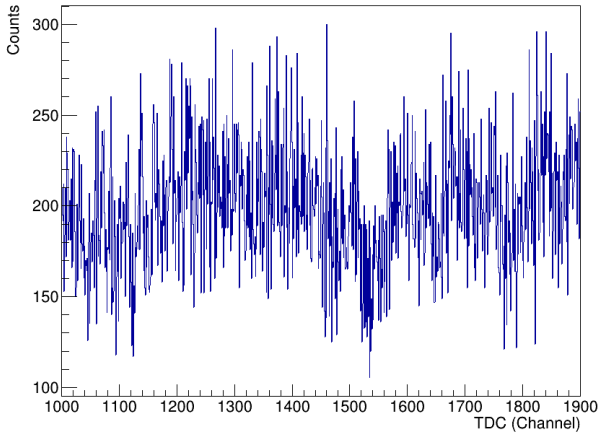
In the case of the X wires, equations 3.48, and 3.49 simplify to the standard LSM formulae while the



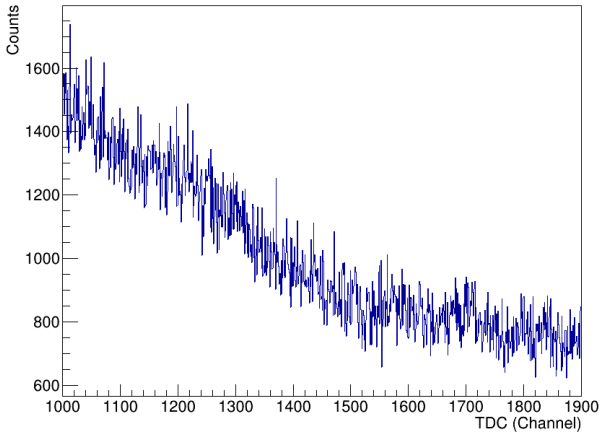
(a) FDC2 layer 1 (X layer) TDC.



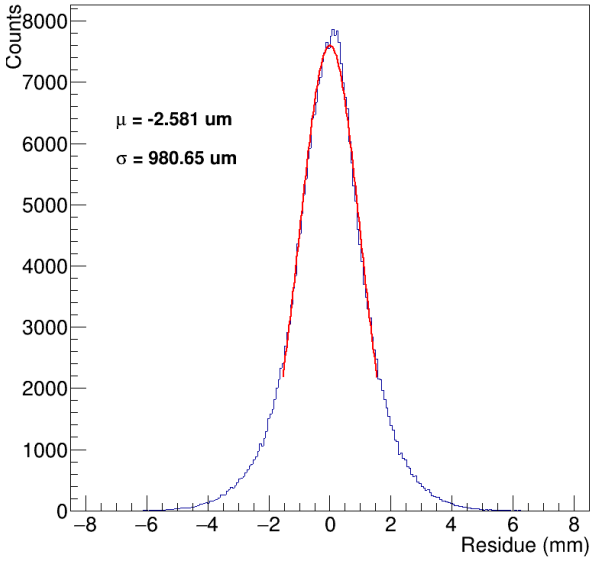
(b) FDC2 layer 1 (X layer) STC.



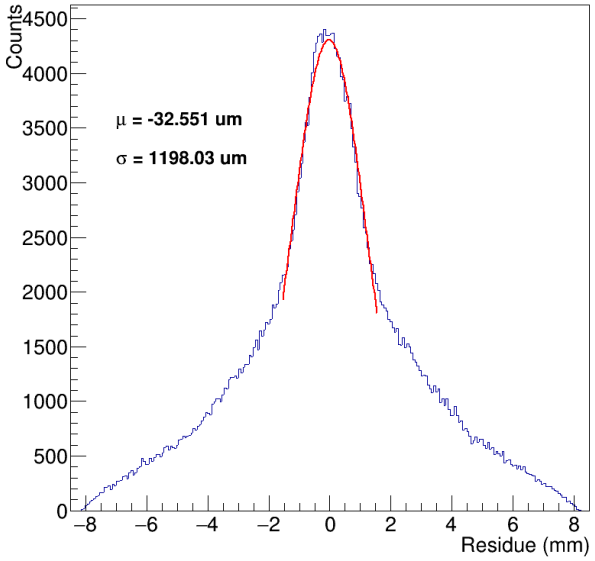
(c) FDC2 layer 11 (U layer) TDC.



(d) FDC2 layer 12 (U layer) TDC.



(e) FDC2 layer 4 (V layer) residue.



(f) FDC2 layer 5 (U layer) residue.

Figure 3.33

U and V follow the form shown above. Then the residue can be determined using equation 3.50 [67].

$$R_p = X_p - [(aZ_p + x_0) \cdot cos(\theta_p) + (bZ_p + y_0) \cdot sin(\theta_p)] \tag{3.50}$$

During the analysis of FDC2, the residue of each layer excluding the two faulty layers was determined. However, as figures 3.33e and 3.33f show, the residue of the remaining U layers was noticeably larger than that of the X and V layers. To further investigate, a comparison of the residue of the remaining 10 layers was done to determine the effect of removing the last two U layers. Figure 3.34 illustrates the residue of each X and V layer of the FDC2 when including the U layers (black line) and when removing them (red line). It can be seen that excluding the U layers significantly improves the overall residue of all other layers signifying an overall improvement in the reconstruction of the position in FDC2.

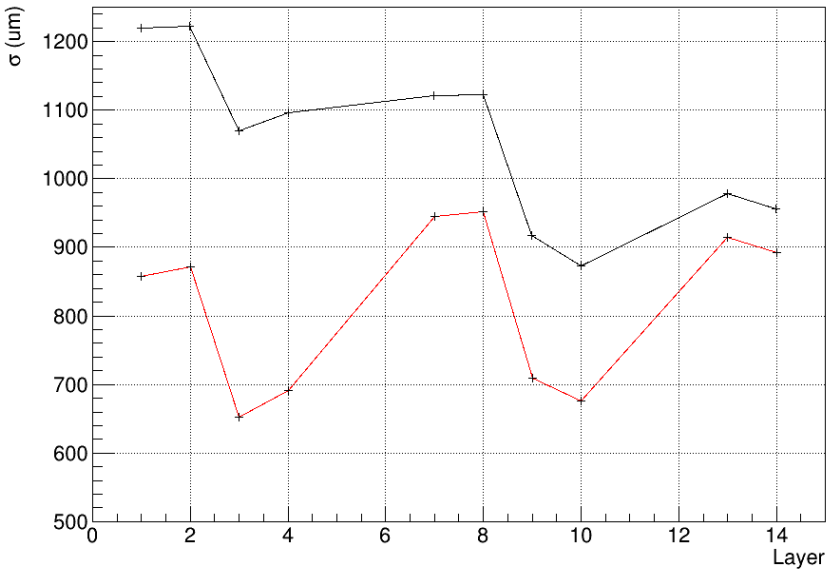


Figure 3.34: FDC2 X and V layers residue when including U layers (black) vs when excluding U layers (red).

Finally, Fig. 3.35 (left) shows the XY position of FDC2 while Fig. 3.35 (right) shows XY position for decay alpha.

3.6.2 FDC2 alignment with hodoscope

The calculation of the $B\rho$ depends on the position at the entrance of the magnet (FDC0) and the position at the exit of the magnet (FDC2) in addition to proper selection of the ^{4}He in hodoscope. This requires

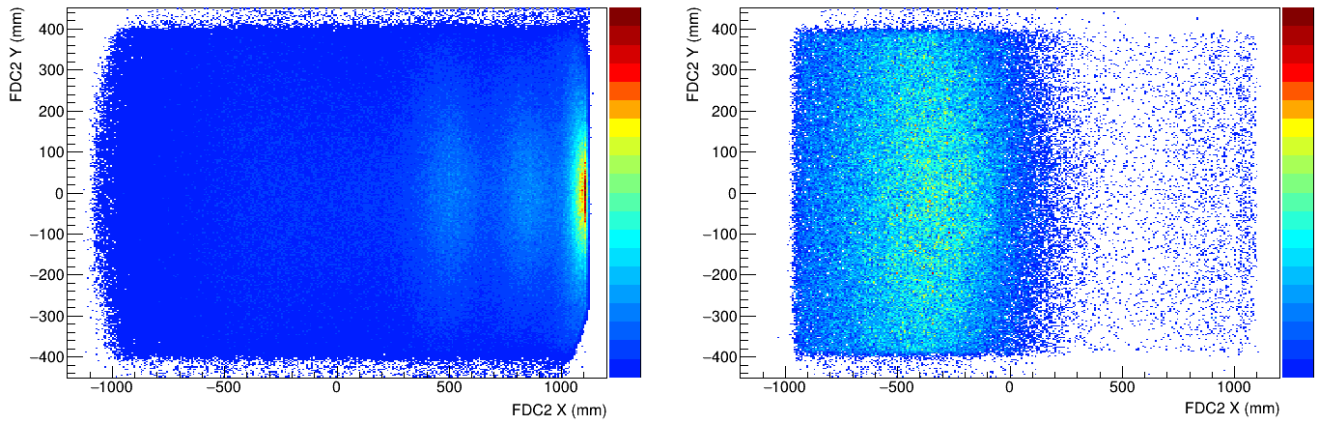


Figure 3.35: FDC2 XY position plot with target area and beam PID conditions (left). FDC2 XY position plot with target area, beam PID, and ^{4}He HOD gate conditions (right).

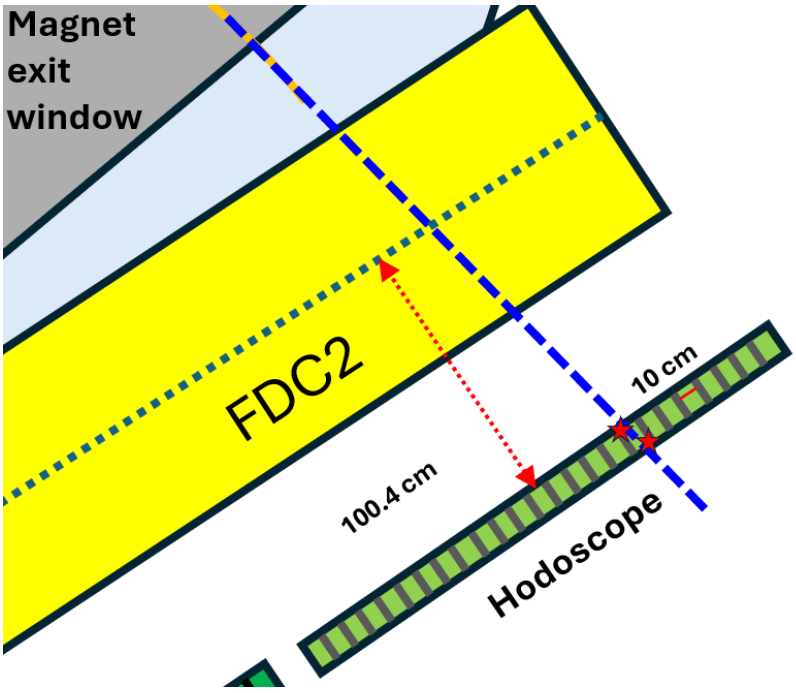


Figure 3.36: Schematic diagram illustrating FDC2 and hodoscope placement. The blue dashed line represents a nucleus exiting the magnet and hitting two adjacent hodoscope bars.

proper alignment between FDC2 and hodoscope. In order to check for the alignment, the X position of FDC2 is extrapolated to hodoscope such that two scintillator bars of hodoscope have been tagged by the same particle as shown in Fig. 3.36. In this figure, the blue dashed line represents a nucleus exiting the SAMURAI magnet and tagging two adjacent hodoscope bars as highlighted by red stars.

Figure 3.37 (left) shows the extrapolation of FDC2 X to the hodoscope with the condition that two adjacent hodoscope bars have been hit. The peaks corresponding to different pairs of bars have been fit with a Gaussian and the difference between the mean values was calculated to be $\sim$ 10 cm which corresponds to the width of each hodoscope bar. Figure 3.37 (right) shows a zoom in as an example of two peaks to demonstrate the process.

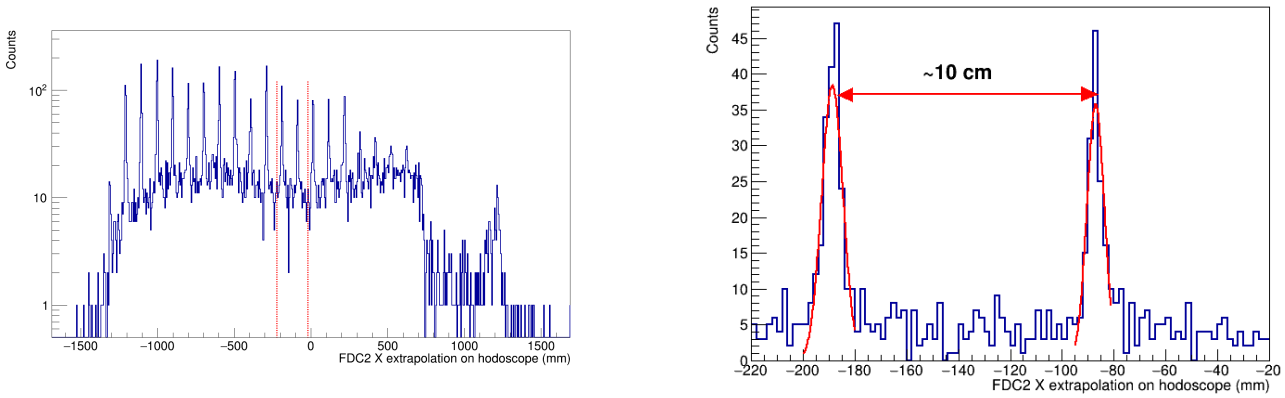


Figure 3.37: Extrapolation of FDC2 on Hodoscope bars when two adjacent bars have been tagged (left). Zoom in of left figure with a fitted Gaussian (right).

3.6.3 Magnetic field map

Precise information on the magnetic field in SAMURAI is essential to enable accurate extraction of the $B\rho$ of alpha residue. The magnetic field map of the SAMURAI magnet was obtained from the RIKEN website. The magnetic field map was generated using OPERA-3D/TOSCA finite-element electromagnetic solver and making use of hall probes used to measure the magnetic field at certain points in the magnet. Due to symmetries in the magnetic field, the map was constructed by dividing the magnet into four quadrants. The field map is provided for the quadrant covering region in cartesian coordinates of $(x, y, z) = (0, -400, 0) \rightarrow (3000, 400, 3000)$ with step size of 10 mm, which was elaborated in [31]. The map provided (B_x, B_y, B_z) corresponding to (x, y, z). The NPTool library [68] made use of the symmetries of the magnetic field to

reconstruct the full magnetic field map of the SAMURAI magnet from the one quadrant information.

3.6.4 $B\rho$ reconstruction

The $B\rho$ value of each alpha nucleus of interest is determined from the initial trajectory for the alpha before the magnet deduced from BDC and FDC0, and its trajectory after the magnet determined by FDC2. In order to extract the $B\rho$ value, the alpha nucleus with an initial $B\rho$ is propagated through the magnet using Lorentz's formulae and a final position at the exit window of SAMURAI is obtained. This final position obtained through the propagation is then extrapolated to the FDC2 position and compared with the measured value of FDC2. This process is then repeated to scan over all possible $B\rho$ values within a range and the $B\rho$ value selected is the one that minimizes the difference between the final position obtained through the propagation and the measured final position. The propagation inside the magnet is done using the Runge-Kutta method of the 4^{th} order discussed in [69] which is used to solve differential equations with high accuracy to determine the new trajectory parameters $(x', y', z', p'_x, p'_y, p'_z)$ from the initial trajectory parameters (x, y, z, p_x, p_y, p_z).

3.6.4.1 Propagation in the magnetic field

When a charged particle traverses an electro-magnetic field, its motion is determined by the Lorentz force affecting it which can be expressed (assuming negligible effect from other forces such as gravity) as

$$\boldsymbol{F}_{Lorentz} = \frac{d\boldsymbol{p}}{dt} = q(\boldsymbol{E} + \boldsymbol{v} \times \boldsymbol{B}) \tag{3.51}$$

Where **p** is the impulse vector, q is the charge, **E** is the electric field, **v** is the velocity vector, and **B** is the magnetic field. Since there is no external electric field applied to the SAMURAI magnet, only the magnetic field component is applied in formula 3.51. Then using the field map mentioned above, the x,y,z components of the impulse on the charged particles can be expressed using formulae 3.52, 3.53, and 3.54.

$$\frac{dp_x}{dt} = q(v_y B_z - v_z B_y) \tag{3.52}$$

$$\frac{dp_y}{dt} = q(v_z B_x - v_x B_z) \tag{3.53}$$

$$\frac{dp_z}{dt} = q(v_x B_y - v_y B_x) \tag{3.54}$$

First, the velocity is needed to determine the x,y,z components of the position. This can be accomplished using relativistic energy (equation 3.55), and momentum (equation 3.56).

$$E = \sqrt{m^2c^4 + \boldsymbol{p}^2c^2} = \gamma mc^2 \tag{3.55}$$

$$\boldsymbol{p} = \gamma m v \tag{3.56}$$

$$\boldsymbol{v} = \frac{\boldsymbol{p}c^2}{E} = \frac{\boldsymbol{p}c^2}{\sqrt{m^2c^4 + \boldsymbol{p}^2c^2}} \tag{3.57}$$

With ($\gamma = \frac{1}{\sqrt{1-\frac{v^2}{c^2}}}$), m is the particle mass, and c is the speed of light. Then the x,y,z components of the velocity can be expressed by

$$\frac{dx}{dt} = \frac{p_x c^2}{\sqrt{m^2c^4 + \boldsymbol{p}^2c^2}} \tag{3.58}$$

$$\frac{dy}{dt} = \frac{p_y c^2}{\sqrt{m^2c^4 + \boldsymbol{p}^2c^2}} \tag{3.59}$$

$$\frac{dz}{dt} = \frac{p_z c^2}{\sqrt{m^2c^4 + \boldsymbol{p}^2c^2}} \tag{3.60}$$

With $\boldsymbol{p}^2 = (p_x^2 + p_y^2 + p_z^2)$. Then we can plug in equations 3.58, 3.59, and 3.60 in equations 3.52,3.53, and 3.54 respectively to obtain the relativistic values of the impulse in the x,y,z direction as

$$\frac{dp_x}{dt} = q(\frac{p_y c^2}{\sqrt{m^2c^4 + \boldsymbol{p}^2c^2}} B_z - \frac{p_z c^2}{\sqrt{m^2c^4 + \boldsymbol{p}^2c^2}} B_y) \tag{3.61}$$

$$\frac{dp_y}{dt} = q(\frac{p_z c^2}{\sqrt{m^2c^4 + \boldsymbol{p}^2c^2}} B_x - \frac{p_x c^2}{\sqrt{m^2c^4 + \boldsymbol{p}^2c^2}} B_z) \tag{3.62}$$

$$\frac{dp_z}{dt} = q\left(\frac{p_x c^2}{\sqrt{m^2c^4 + \boldsymbol{p}^2c^2}}B_y - \frac{p_y c^2}{\sqrt{m^2c^4 + \boldsymbol{p}^2c^2}}B_x\right) \tag{3.63}$$

Therefore, formulae 3.58-3.63 define the time derivative of the six-component vector (x, y, z, p_x, p_y, p_z) of the alpha residue which is propagated through the magnet using RK4 method from its initial position at the entrance of the magnet to its final position at the exit of the magnet and determining the six-component vector at the exit [70].

3.6.4.2 NPTool logic

The **"SamuraiFieldMap.hh"** library of the NPTool framework was utilized for the Bρ calculation. The code starts by using the symmetry of the SAMURAI magnet to extrapolate the magnetic field provided by the field map file of one quadrant to the whole magnet. Afterwards, using the entry position of the alpha nucleus provided by FDC0 position (Fig. 3.38 red star), it is propagated throughout the magnet using the Runge-Kutta method (known as RK4 [69]) with the formulae mentioned above assuming a range of initial energies corresponding to different Bρ values. The time step used for the RK4 method was 1 ns while the range of $B\rho$ scanned was 1-10 T.m. The step size of the scan was tested with different step sizes and the result with the best $B\rho$ resolution corresponded to a step size of 0.01 T.m. Then the position of the alpha particles at the exit of the magnet after the propagation is determined and extrapolated to FDC2 center (blue star) as shown in Fig. 3.38 . The Bρ value selected is the value that minimizes the difference between the extrapolated position at FDC2 and the measured position from FDC2 center.

3.6.5 $B\rho$ extraction and resolution

In order to verify the Bρ reconstruction and determine the resolution, the data obtained with a secondary alpha beam of a narrow momentum width that was prepared for the energy calibration of the CsI(Tl) and DSSD modules of the Telescope array was utilized. The first step is to check how well calibrated the $B\rho$ calculation is relative to the measured beam energy. This can be done utilizing the energy of the alpha beam determined through ToF, then comparing the $B\rho$ value of that energy with the one obtained from the calculation. Figure 3.39 shows the alpha beam energy distribution which is determined by the ToF

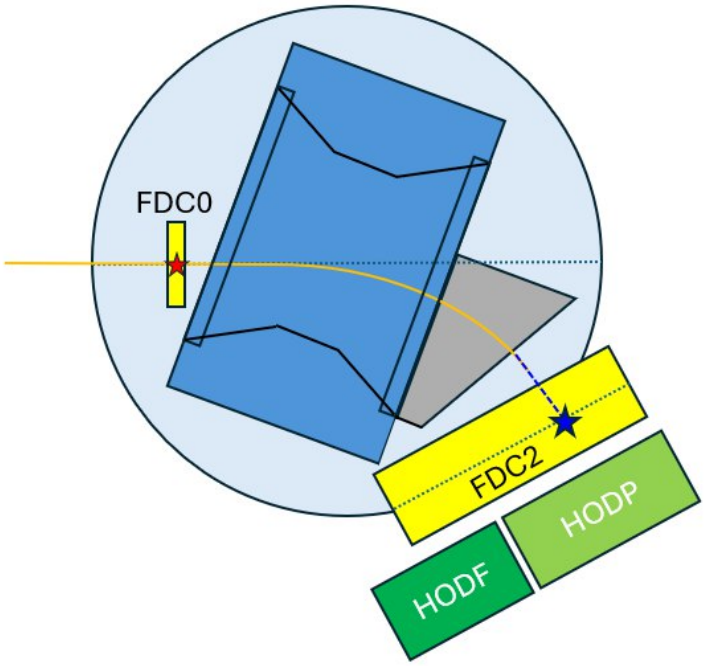


Figure 3.38: Schematic diagram of the SAMURAI magnet showing entry position detection with FDC0 (red star) and extrapolated position at FDC2 (blue star).

between F7 and F13 plastic detectors. It was fit with a Gaussian where the mean value of this fit is ~ 156.9 MeV/u. This value was then input in Lise++ simulation as the value of alpha energy at F13 plastic detector and propagated through all layers of detectors, windows, and air to determine the remaining energy at the entrance of the SAMURAI magnet. The mean value of the energy was found to be ~ 155.7 MeV/u which corresponds to a $B\rho$ of 3.7412 T.m. This value was then compared with the mean of the Gaussian fit of Fig. 3.40 which shows the calculated $B\rho$ distribution of the ^{4}He beam. The mean value of the $B\rho$ from the fit is 3.741 T.m which agrees very well with the measured.

Using the sigma of the Gaussian fit of Fig. 3.40 (σ = 0.0324 T.m), the width in $B\rho$ obtained was 0.866% in sigma. This value is a convolution of the width of the resolution of the $B\rho$ calculation and beam momentum distribution as shown in formula 3.64. The $B\rho$ acceptance is needed for the determination of the $B\rho$ resolution due to calculation.

$$(\frac{\Delta B\rho}{B\rho})^2 = (\frac{\Delta B\rho_{acceptance}}{B\rho})^2 + (\frac{\Delta B\rho_{calculation}}{B\rho})^2 \tag{3.64}$$

Recalling Fig. 3.39, the Gaussian fit of the beam energy distribution of the ^{4}He beam which was determined using the ToF between F7 and F13 had a mean of 156.87 MeV/u and a sigma of 0.6 MeV/u, this

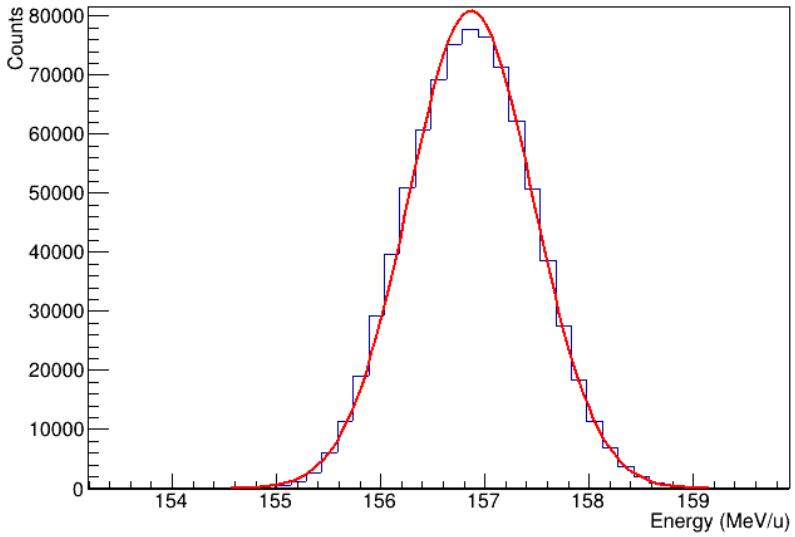


Figure 3.39: ^{4}He beam energy distribution measured with the plastic detectors placed at F7 and F13.

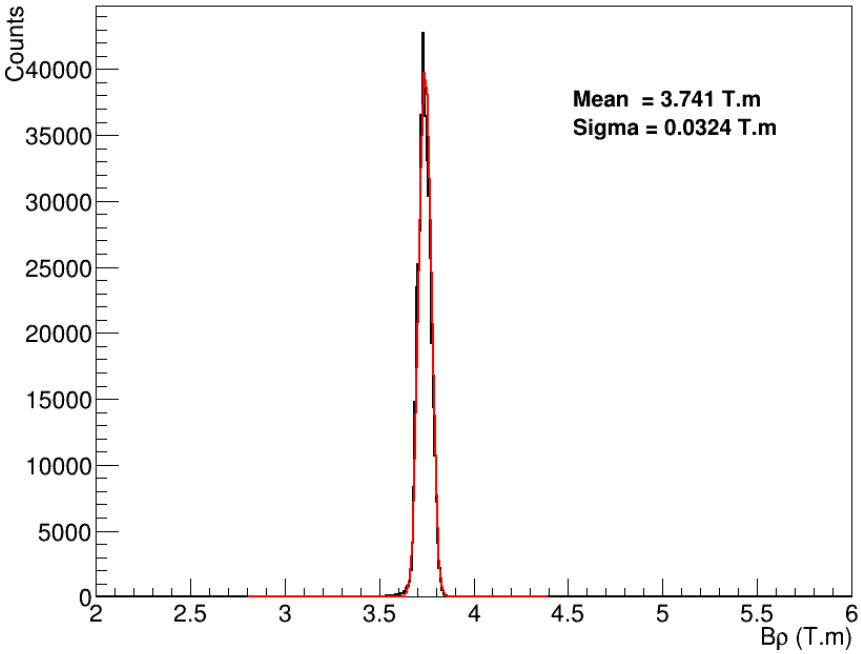


Figure 3.40: $B\rho$ reconstruction of ^{4}He beam with a Gaussian fit in red.

corresponds to an energy resolution of ~ 0.382%. This energy resolution is a convolution of the momentum width of the beam and the resolution of the plastic detectors at F7 and F13. The latter was determined by fitting the time signal from SBT1 and SBT2 as shown in Fig. 3.41. The respective resolutions of each plastic were then summed as the beam energy is obtained through the average timing of these two plastic scintillators. The time resolution was determined to be 0.089% which corresponds to ~ 0.179% in energy. Then using formula 3.65, the sigma of the distribution corresponding to the momentum acceptance of the beam line is ~ 0.34%.

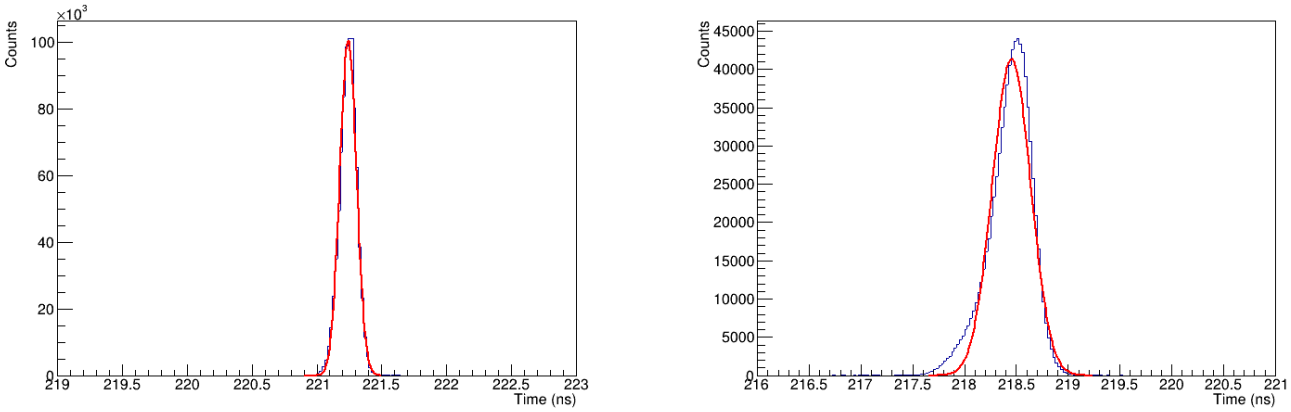


Figure 3.41: SBT1 time (left), SBT2 time (right) both with a Gaussian fit.

$$\frac{\Delta E_{acceptance}}{E} = \sqrt{(\frac{\Delta E_{beam}}{E})^2 - (\frac{\Delta E_{plastic}}{E})^2} \tag{3.65}$$

Recalling the relation between energy and $B\rho$, the $B\rho$ acceptance can be expressed as

$$\frac{\Delta B\rho}{B\rho} = \frac{1}{2}\frac{\Delta E}{E} \tag{3.66}$$

which leads to a $B\rho$ resolution due to beam acceptance of ~ 0.169%. Substituting the values for beam acceptance and overall $B\rho$ resolution in formula 3.64, the effect of the calculation on the overall $B\rho$ resolution was determined to be ~ 0.849%.

The $B\rho$ resolution will be used in the following to simulate the 6 neutrons resolution to better understand the 6 neutrons spectrum.

Chapter 4

Results and Discussion

After calculating all the energy and scattering angles of all the particles of the $(p, p\alpha)$ reaction, the missing mass formula can now be used to study the ^{10}He nucleus and identify its ground and excited states. Furthermore, the 6-neutrons system spectrum can be obtained. In this chapter, the fit and discussion of the ^{10}He ground state and excited state(s) will be discussed in addition to the determination of the 6-neutron system spectrum and the corresponding background reduction and phase-space calculation.

4.1 Status of ^{10}He spectroscopy

The nucleus of ^{10}He is an extreme nuclear system with one of the largest N/Z ratios. According to the standard shell model, with Z=2 and N=8, it would be expected to be doubly magic but was first observed as a largely unbound resonance in 1994 by Korsheninnikov et al. at RIKEN [71]. Theoretically, it is studied as a ^{8}He + n + n three-body system but its description is complicated by the limited knowledge on the ^{8}He + n interaction. The true nature of its ground state has been a subject of debate since its discovery. Multiple experiments have been performed using different reactions to populate the resonances in ^{10}He with varying results about its ground state energy. Different invariant mass spectroscopy experiments were performed to measure the ^{8}He + n + n relative energy using knockout reactions. A typical spectrum obtained in a knockout reaction experiment is shown in Fig. 4.1.

The ground state energy from the knockout reaction experiments can be determined to be 1.5(1) MeV and a width $\Gamma \sim 1-2$ MeV by using the weighted average from ^{11}Li$(-p)$ experiments ($E_{g.s.}$ = 1.2(3) MeV, $\Gamma \leq$

1.2 MeV [71], $E_{g.s.}$ = 1.7(4) MeV [72], and $E_{g.s.}$ = 1.54(11) MeV, Γ = 1.91(41) MeV [73]), and ^{14}Be($-2p2n$) reaction with $E_{g.s.}$ = 1.60(25) MeV with Γ = 1.8(4) MeV [74]. The ^{11}Li(d,^{3} He) transfer reaction experiment performed afterwards found a ground state energy of $E_{g.s.}$ = 1.4(3) MeV with $\Gamma \sim 1.5(2)$ MeV [75].

At variance with the results of the above studies, the two-neutron transfer reaction suggested a ground state energy $E_{g.s.}$ = 2.1(2) MeV with $\Gamma \sim 2$ MeV [76]. This discrepancy has been partly attributed to initial-state effects associated with the halo structure of ^{11}Li and ^{14}Be, which may shift the observed energy to lower values in knockout reactions [77, 78]. Calculations including such effects qualitatively reproduce the invariant mass spectrum from the ^{11}Li($-p$) reaction [78], but fail to describe the spectrum observed in the ^{14}Be($-\alpha$) or ($-2p2n$) reactions [79], suggesting that this mechanism alone cannot fully account for the experimental observations. According to Sharov et al., the ^{10}He ground state lies near $\sim$ 2 MeV, with a dominant $[p_{1/2}]^2_{0^+}$ configuration [78].

Alternatively, three-body ^{8}He + n + n model calculations predict the existence of two low-lying 0^+

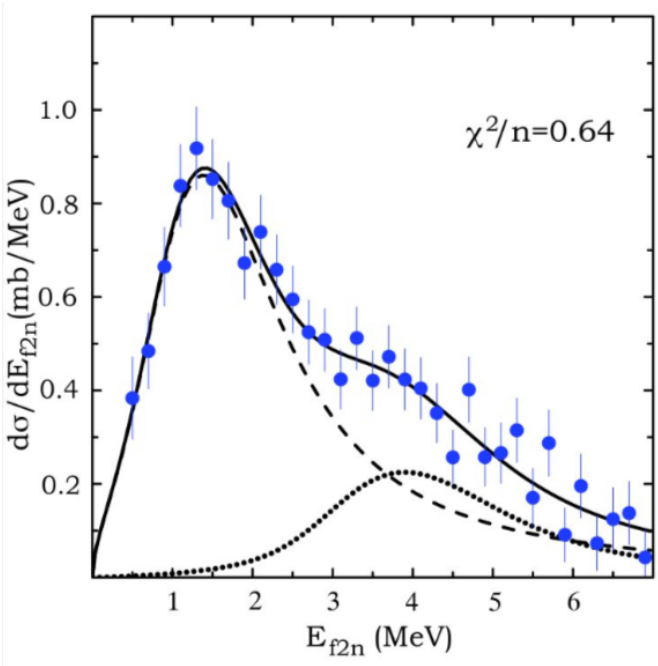


Figure 4.1: Relative energy spectrum of the ^{8}He+2n system from the ^{1}H(^{11}Li,^{8} He+2n) reaction. Experimental data are shown as filled circles with error bars. The dashed and dotted lines describe Breit–Wigner shaped resonances. The solid line is the sum of these two components. (Fig. from [73]).

states with $[s_{1/2}]^2_{0^+}$ and $[p_{1/2}]^2_{0^+}$ valence neutron configurations, built on different ^{9}He core states [77, 80]. In this framework, the observed variation in ground state energy may arise from the population

of two overlapping 0^+ states with different strengths in knockout and transfer reactions [77, 81]. In the following we present the decomposition of the ^{10}He spectrum from the ^{14}Be$(p, p\alpha)$ reaction obtained by missing mass. The energy resolution obtained in such experiments is significantly larger than in invariant mass measurements. Possible contribution of resonances at energies beyond 2 MeV is also discussed in comparison with previous works.

4.1.1 ^{10}He excitation energy spectrum

In a similar way to section 3.3.3.2, the excitation energy can be computed using formulae 3.36-3.40 (replacing ^{12}Be with ^{14}Be and ^{8}He with ^{10}He). The ^{10}He energy is usually determined with respect to ^{8}He + $2n$ threshold such as

$$E_{ex.}(^{10}\mathrm{He}) = \sqrt{E^2_{^{10}\mathrm{He}} - P^2_{^{10}\mathrm{He}}} - (m_{^8He_{g.s.}} + 2m_n) \tag{4.1}$$

where m_n is the mass of a neutron and $E_{ex.}(^{10}$He) is the excitation energy of ^{10}He relative to the threshold of $2n$ emission. Figure 4.2 shows the ^{10}He excitation energy relative to the threshold of $2n$ emission with ^{8}He HOD gate in black and ^{4}He HOD gate in red. It can be seen that the background for the case with ^{8}He HOD gate is minimal while using the ^{4}He gate which is used for the 6-neutron system energy calculation has significantly more background. Considering that the acceptance for ^{8}He and ^{4}He is similar, one observes that the structure, previously assigned to the ground state of ^{10}He, decays predominantly to ^{8}He + $2n$ even above ^{4}He + $6n$ threshold, but becomes comparable at energies above 6 MeV. We note that the present data allow to extract for the first time the ^{8}He and ^{4}He branching ratios for the decay of ^{10}He resonances, which provides useful information on their structure, e.g., their three-body nature or beyond. It should be noted that the spectrum in coincidence with ^{6}He residues could not be obtained because most of the ^{6}He nuclei were lost in the gap between the two Hodoscope walls (HODF and HODP). In the following we present fits of our spectrum obtained for the ^{8}He + $2n$ channel, in order to compare the extracted resonances properties to previous results, which were obtained exclusively for this channel.

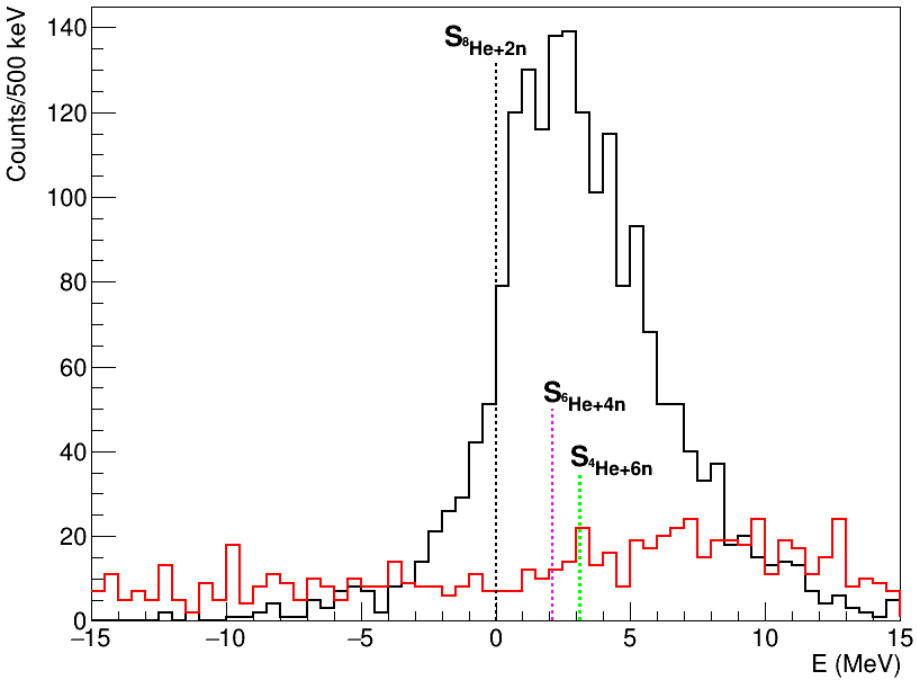


Figure 4.2: ^{10}He excitation energy relative to the threshold of $2n$ emission with ^{8}He HOD gate in black and ^{4}He HOD gate in red.

4.1.2 Voigt fit

The energy spectrum of ^{10}He for the ^{8}He+2n channel has been fit with the Voigt function which is a convolution of a Gaussian and a Breit-Wigner function as shown in the following equation

$$F_{Voigt}(E) = \int_{-\infty}^{+\infty} dE' \cdot F_{Gauss} \cdot F_{BW} \tag{4.2}$$

The Gaussian component is related to the energy resolution of the apparatus and is determined from simulation as described below. The sigma values of the Gaussians are obtained from figure 4.4 (σ = 1.37 MeV at 0 MeV). The main parameters to determine from the fit are the mean value of the energy and the width (Γ). The Breit-Wigner distribution has an energy-dependent Γ of the following form

$$\Gamma(E) = \frac{2\gamma_0}{(\pi M \rho_{ch}^2)[J_{k+2}^2(\chi\rho_{ch}) + N_{k+2}^2(\chi\rho_{ch})]} \tag{4.3}$$

where $\chi = \sqrt{2ME}$ and ρ_{ch} is the channel radius of the decay, fixed at 40 fm, M is the nucleon mass, and

K the hyper momentum of the neutron pair while J and N are the regular and irregular Bessel functions, respectively, and γ_0 is the reduced width (free parameter) [75].

4.1.3 Resolution determination from simulation for the ^{10}He spectrum

The simulation code is based on the principles of relativistic kinematics and a data-driven Monte Carlo sampling procedure. Events are sampled from experimental data and used to generate new kinematically consistent events derived from the measured distributions. The general schematic of the simulation consists of randomly sampling events satisfying conditions in the hodoscope and within a selected range of proton angles in order to constrain the proton kinematics. For these events, a set of proton and alpha energies and angles $(T_1, \theta_1, \phi_1, T_2, \theta_2, \phi_2)$ is obtained from the data. For the reaction

$$a + b \rightarrow 1 + 2 + 3 \tag{4.4}$$

where **a** is the beam, **b** is the target, **1** is the proton, **2** is the alpha particle, and **3** corresponds to the ^{10}He system, the following steps are performed:

1. Build the initial state of the reaction:

$$\boldsymbol{P}_{CM} = \boldsymbol{P}_a + \boldsymbol{P}_b \tag{4.5}$$

   where $\boldsymbol{P}$ denotes the four-momentum.

2. Construct the recoil system R_{23} in the center-of-mass frame. Using invariant kinematics (see Appendix A), the four-momentum $\boldsymbol{P}_2$ is obtained by solving a quadratic equation. This leads to three possible cases: (1) one physical solution, (2) no physical solution, or (3) two physical solutions. In case (3), the solution with T_2 closest to the sampled value is selected.

3. Reconstruct particle 3 using

$$\boldsymbol{P}_3 = \boldsymbol{P}_{CM} - \boldsymbol{P}_1 - \boldsymbol{P}_2 \tag{4.6}$$

4. Perform a Lorentz boost to the beam frame.

5. Determine the excitation energy of particle **3**.

Subsequently, for each excitation energy generated in the previous step, we make use of the fact that each event is defined by an ensemble of observables $(T_1, \theta_1, \phi_1, T_2, \theta_2, \phi_2)$. Each observable has an associated experimental resolution; therefore, it is possible to generate a new set of observables by applying Gaussian smearing to the initial values within their respective resolutions and recomputing the excitation energy.

For example, considering an event with excitation energy $E_{ex.}$ corresponding to a set of variables E_{beam}, (T_1, θ_1, ϕ_1), and (T_2, θ_2, ϕ_2), which was obtained as mentioned above. The following steps are then applied:

1. A new set of observables is generated by applying random Gaussian variations to the initial values according to the corresponding detector resolutions.

2. The smeared observables are used to reconstruct a new excitation energy using the same kinematic relations.

3. This process is repeated for many events to build up statistical distributions.

This procedure allows the accumulation of events with reconstructed ^{10}He excitation energy, which can then be grouped according to their true excitation energy. For each 1 MeV bin from 0 MeV to 20 MeV, the reconstructed excitation energy distribution is fitted with a Gaussian function, as shown in Fig. 4.3.

From these fits, the centroid and width (σ) are extracted. The width represents the experimental resolution of the reconstructed excitation energy. For the sigma values utilized in the analysis, the same method was used in a slightly different manner, where instead of generating the phase-space from solving the quadratic formula as mentioned in the second step in the procedure above, all information about particle 2 (alpha) was obtained from the data and particle 3 is constructed from equation 4.6. This method provides a better description of the resolution because the data offer a more realistic distribution of kinematic correlations of the outgoing p–α pairs than those obtained from scanning the phase space with fixed kinematic steps. Consequently, it was used in the following analysis. A plot of excitation energy versus σ is then constructed, as shown in Fig. 4.4. The negative slope of the resolution can be mostly attributed to the alpha resolution changing with energy.

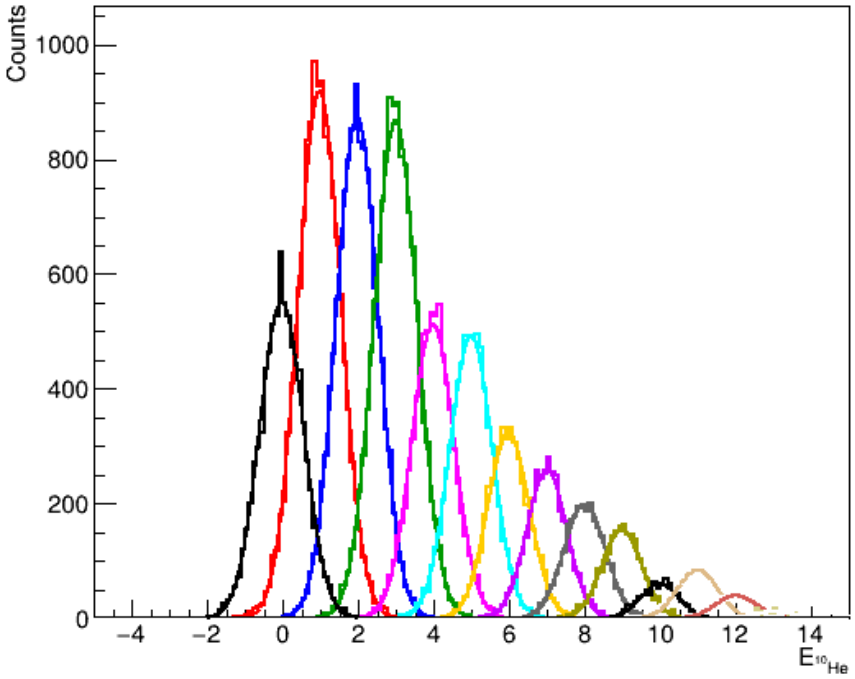


Figure 4.3: ^{10}He simulation with a Gaussian fit for each 1 MeV excitation energy bin.

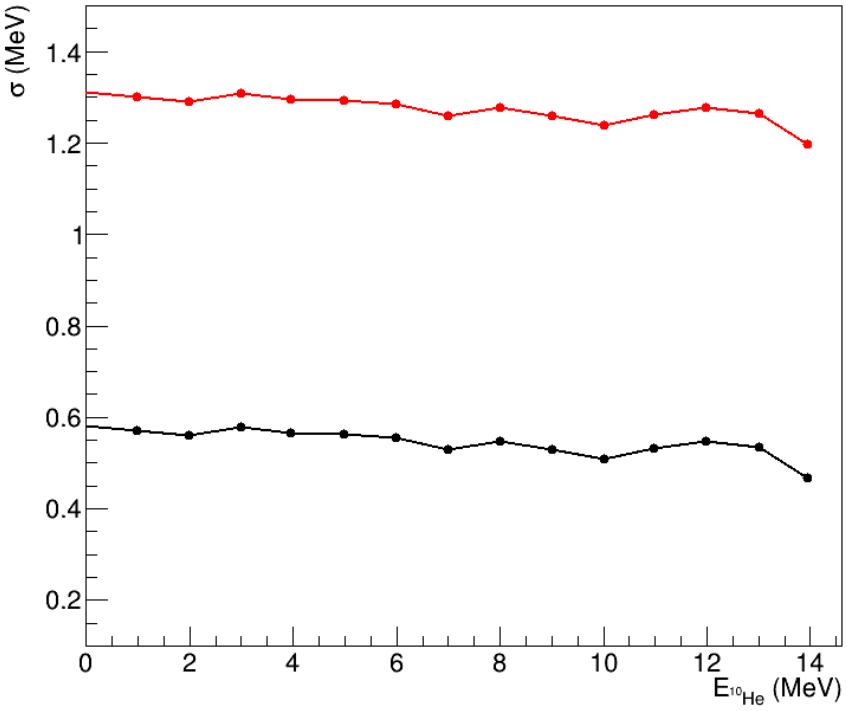


Figure 4.4: Excitation energy versus resolution (σ) obtained from Gaussian fits to each 1 MeV bin (Black:pre correction, Red:post correction).

Since the σ values obtained from the simulation are slightly lower than those extracted from Fig. 3.24b (at 0 MeV), a systematic correction is applied such that the resolution at 0 MeV matches the experimental value of 1.37 MeV. The offset was determined by using the simulation for ^{8}He then applying the same factor to the ^{10}He simulation. The σ values used in the Voigt fits are then obtained by evaluating this energy-dependent resolution function at the corresponding excitation energy.

4.1.4 Decomposition of the ^{10}He spectrum in ^{8}He channel

The missing mass spectrum of ^{10}He gated by the ^{8}He HOD gate was fit with one, two and three resonances as presented below with the sigma of the Gaussian function varying according to Fig.4.4.

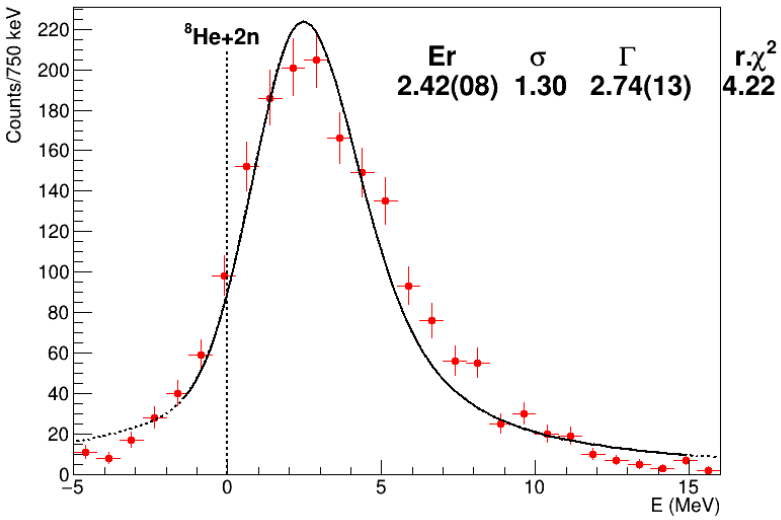


Figure 4.5: ^{10}He energy spectrum from ^{14}Be$(p, p\alpha)^{10}$He reaction w.r.t. ^{8}He + $2n$ fit with Voigt function of 1 resonance.

The initial values of energy and width were those from [73] for the first resonance and the second resonance. In the case of three resonances, the third energy and width were obtained from [75] and were set as fixed parameters. Figure 4.5 shows the result of using a single resonance fit. The fit procedure gave the values $E_r(0) = 2.42(08)$ MeV, $\Gamma = 2.74(13)$ MeV and reduced $\chi^2 = 4.22$. This resonance energy value is much higher than in previous literature, whether from transfer or knockout reactions. Furthermore, the high reduced χ^2 (4.22) for the single-resonance model statistically excludes this hypothesis with high significance, strongly suggesting the population of excited states. Subsequently, the spectrum was fit with two resonances as shown in Fig. 4.6.

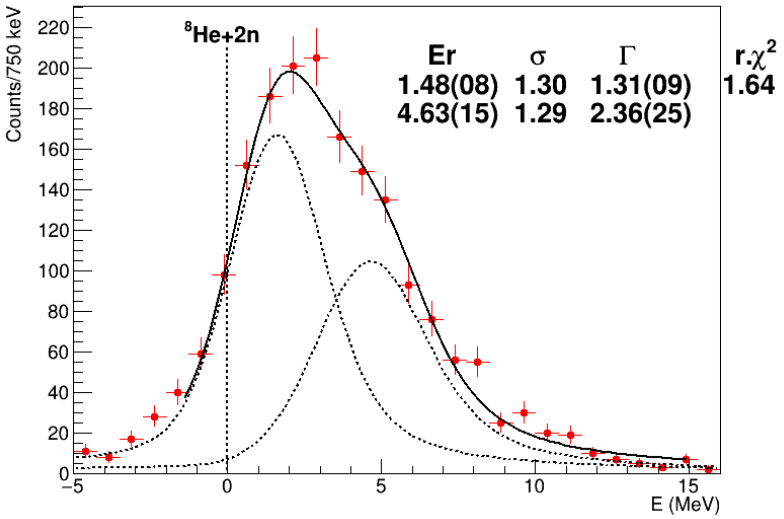


Figure 4.6: ^{10}He energy spectrum from ^{14}Be$(p, p\alpha)^{10}$He reaction w.r.t. ^{8}He + $2n$ fit with Voigt function of 2 resonances.

The lowest energy resonance was found to be (see table 4.1) $E_r(0) = 1.48(08)$ MeV with $\Gamma(0) = 1.31(09)$ MeV which agrees (within errors) with [73] for both the energy and width. As for the second resonance, it had energy $E_r(1) = 4.63(15)$ MeV with $\Gamma(1) = 2.36(25)$ MeV which is larger than [73] values for the energy and width. Finally, the spectrum was fit with three resonances where the third resonance energy and width were fixed at 6.3 MeV and 3.2 MeV respectively [75].

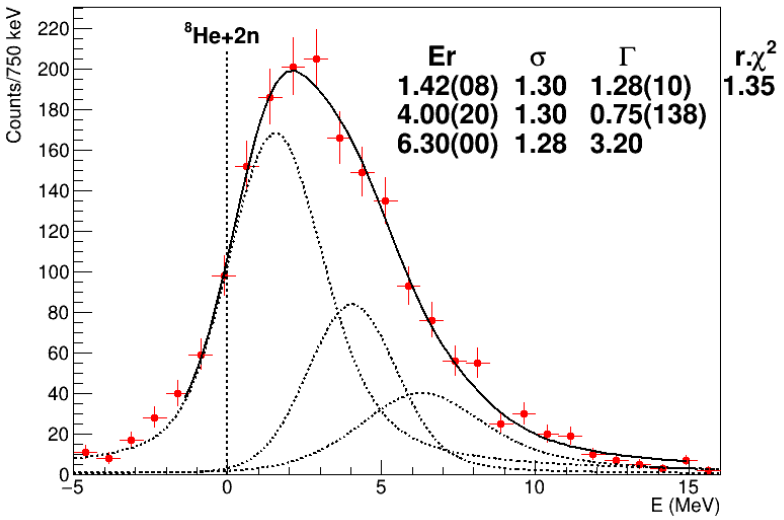


Figure 4.7: ^{10}He energy spectrum from ^{14}Be$(p, p\alpha)^{10}$He reaction w.r.t. ^{8}He + $2n$ fit with Voigt function of 3 resonances.

The lowest energy resonance was found to be $E_r(0) = 1.42(08)$ MeV with $\Gamma(0) = 1.28(10)$ MeV which

agrees (within errors) with the results of most of the previous works except the $2n$ transfer experiment for the energy but the width is lower than them. As for the second resonance, it had energy $E_r(1) = 4.00(20)$ MeV with $\Gamma(1) = 0.75(138)$ MeV which agrees well with [73] values for the energy and width (within error). A slight improvement in the reduced χ^2 was obtained when fitting with the second resonance as a fixed parameter, however, the overall results are the same as shown in table 4.2. We note that the lowest overall reduced $\chi^2 = 1.26$ was lower than that using two resonances which is a weak indication of the population of the resonance at 6.3 MeV seen in [75].

Because of the rather structureless shape of the spectrum, further fits were performed with some restrictions, namely, the variation in the width parameters were restricted to the uncertainties of their values in [73][75]. For the fit with two resonances, table 4.1 shows the parameters tested with the orange boxes representing fixed parameters, green boxes representing limited parameters ($\Gamma 1(0.75 - 2.53)$ MeV) in case **(2)**, and the rest were considered free parameters. Case **(1)**, where all parameters were left free (table 4.1), was found to be the one with best reduced χ^2. The cases where the second resonance energy was fixed at the energy found in [73] produced slightly larger reduced χ^2. We note that an attempt to include this resonance in the spectrum from [74] did not improve the χ^2 (Fig. 4.8). Although the energy obtained is slightly different, our data confirm the presence of a resonance around 4 MeV in ^{10}He.

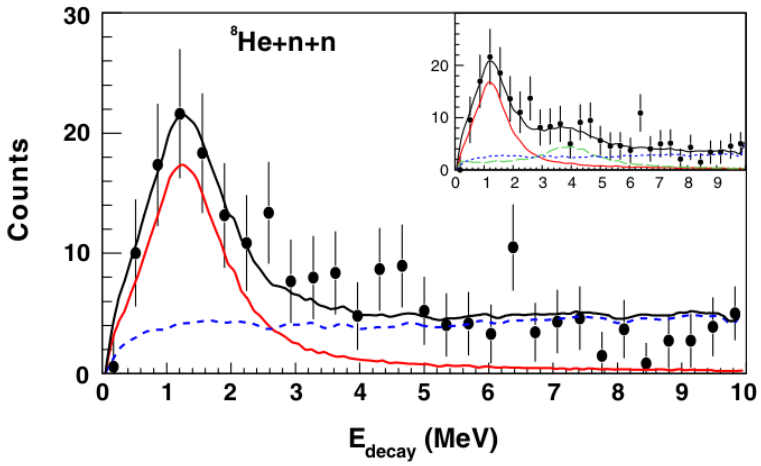


Figure 4.8: The experimental three-body decay energy of ^{10}He is shown as solid black circles with statistical error bars. A Breit-Wigner resonance [solid gray (red) line] and non-resonant background (short dashed blue line) from the Monte Carlo simulation have been fit to the experimental distribution. The sum of the Breit-Wigner and non-resonant components is shown as a solid black line ($\chi^2/\mu = 0.75$). The inset shows a fit to the experimental data which includes the population of the first excited state at 4 MeV (long dashed green line) as measured in [73](Fig. obtained from [74]).

Case	E0	Γ0	E1	Γ1	r.χ^2
1	1.48(08)	1.31(09)	4.63(15)	2.36(26)	1.64
2	1.48(08)	1.31(09)	4.63(15)	2.36(25)	1.64
3	1.25(12)	1.21(14)	3.99(00)	2.53(118)	1.95
4	1.28(13)	1.22(13)	3.99(00)	2.65(22)	2.04
5	1.36(09)	1.88(19)	3.99(00)	1.64(00)	2.64

Table 4.1: Parameter condition used for the Voigt fit with two resonances (orange boxes for fixed parameters, and green boxes for limited parameters).

For the fit with three resonances, Table 4.2 shows the parameters obtained with the orange boxes representing fixed parameters, green boxes representing limited parameters [($\Gamma1(0.75-2.53)$ MeV) in case **(2)**, ($\Gamma1(0.75-2.53)$, $E2(5.6-7)$ MeV) in case **(6)**, and ($E2(5.6-7)$ MeV) in case **(7)**], and the rest were considered free parameters. Case **(1)** was found to be the one with best reduced χ^2 and compatibility with [73]. As in the case of the fit with two resonances, our data confirm the presence of a resonance around 4 MeV in ^{10}He.

Case	E0	Γ0	E1	Γ1	E2	Γ2	r.χ^2
1	1.44(23)	1.29(14)	4.09(57)	1.49(32)	6.3(00)	3.2(00)	1.44
2	1.42(08)	1.28(10)	4.00(20)	0.75(138)	6.3(00)	3.2(00)	1.35
3	1.42(10)	1.28(11)	3.99(00)	0.75(136)	6.3(00)	3.2(00)	1.26
4	1.40(12)	1.28(11)	3.99(00)	1.48(30)	6.3(00)	3.2(00)	1.35
5	1.40(13)	1.28(11)	3.99(00)	1.64(00)	6.3(00)	3.2(00)	1.30
6	1.40(13)	1.28(11)	3.99(00)	0.75(144)	6.42(47)	3.2(00)	1.34
7	1.39(15)	1.27(12)	3.99(00)	1.64(00)	6.45(96)	3.2(00)	1.38

Table 4.2: Parameter condition used for the Voigt fit with three resonances (orange boxes for fixed parameters, and green boxes for limited parameters).

4.1.5 New results on ^{10}He

Very recently new results came out from an experiment performed at RIKEN using the ^{11}Li$(p, 2p)$ reaction at 250 MeV/u (Y.L.Sun et al., to be published in Nature Comm.). In this study high statistics and high sensitivity (especially in the low-energy part of the spectrum) could be achieved. The typical energy resolution was about $\sigma = 0.15$ MeV at 1 MeV above the ^{8}He + $2n$ threshold. The spectrum is displayed in Fig. 4.9. The low energy part (below 2 MeV) is in agreement with the early measurement of [71], but not

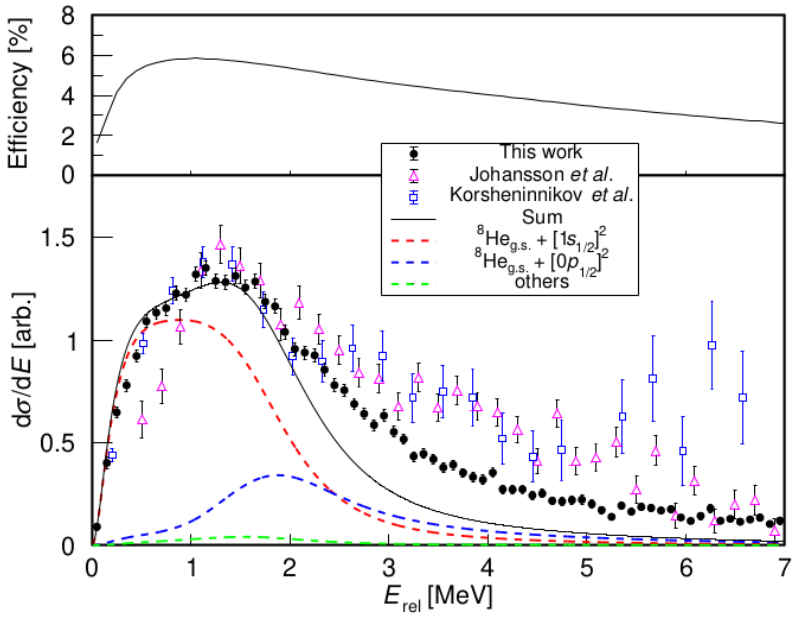


Figure 4.9: (Color online) ^{8}He $- n - n$ relative energy spectrum obtained from the ^{11}Li$(p, 2p)$ reactions compared to two previous results from RIKEN [71] and GSI [73] (both efficiency corrected and re-scaled to match the peak height of current data). The errors shown are statistical. The data are also compared to theoretical calculation (black solid line) that is decomposed to three components: ^{8}He$_{g.s}$ + $[1s_{1/2}]^2$ (red dashed line), ^{8}He$_{g.s}$ + $[0p_{1/2}]^2$ (blue dashed line) and others (two neutrons in partial waves other than $1s_{1/2}$ and $0p_{1/2}$, green dashed line). The upper panel displays the $2n$ detection efficiency after the cross-talk rejection.

with the data of [73]. It is compared to theoretical calculations combining the coupled ^{9}Li + $2n$ three-body model of ^{11}Li and a quasi-free knockout reaction model. The experimental spectrum is discussed as the sum of 3 calculated contributions corresponding to ^{8}He$_{g.s}$ + $[1s_{1/2}]^2$ (red dashed line), ^{8}He$_{g.s}$ + $[0p_{1/2}]^2$ (blue dashed line) and others (two neutrons in partial waves other than $1s_{1/2}$ and $0p_{1/2}$, green dashed line). The two 0^+ states found at about 1 MeV and 2 MeV have $[1s_{1/2}]^2$ and $[1p_{1/2}]^2$ neutron configurations, respectively. The shoulder structure obtained below 1 MeV is assigned to the ^{10}He ground state. This state is discussed in terms of a three-body state with only zero-relative angular momenta between all its subsystems. In the future these contributions could be used to fit our data but the rather limited resolution

obtained in our missing mass measurement would clearly limit the conclusions.

4.2 Calculation of the 6-neutron system energy

In the next section we present the extracted 6-neutron energy spectrum for ^{10}He energies above the 6 neutron emission threshold, as well as an additional gating of events aiming to reduce the background.

$$P_{6n} = \sqrt{P^2_{^{10}\mathrm{He}} + P^2_{\alpha} - 2P_{^{10}\mathrm{He}}P_{\alpha}cos\theta_{^{10}\mathrm{He}-\alpha}} \tag{4.7}$$

$$E_{6n} = E_{^{10}\mathrm{He}} - E_{\alpha} \tag{4.8}$$

$$E_x(6n) = \sqrt{E^2_{6n} - P^2_{6n}} - 6m_n \tag{4.9}$$

After computing the excitation energy of the 6-neutron system, background reduction was needed because of the high background in the ^{10}He energy spectrum. This background arises from several sources of alpha particles—for instance, alphas produced by other reactions in the target, detector windows, or the air—which reach the hodoscope and contaminate the ^{4}He gate.

4.2.1 Background reduction

Figure 4.10 shows the ^{10}He energy spectrum relative to the threshold of $2n$ emission and the corresponding $6n$ spectrum. In the ^{10}He energy spectrum the threshold for $2n$ emission is highlighted in black dashed line, the threshold for $6n$ emission is highlighted in green dashed line, and the blue shade covers energies of 3-15 MeV which represents the energies allowing the emission of 6 free neutrons. A method to possibly reduce the background is to use the trigger from NEBULA which can tag at least one of the six neutrons produced in the α-decay of ^{10}He with good efficiency. In both spectra of Fig. 4.10, the black line represents data without the NEBULA trigger, and red line represents data with the NEBULA trigger. In Fig. 4.2, it appears that the ^{10}He spectrum for the alpha decay channel exhibits an almost flat shape at negative energies, which can be attributed to background. Fig. 4.10 shows that counts at negative energies where no neutrons should be emitted are reduced by about a factor two. In the positive energy region above S_{6n}, the reduction factor becomes about 0.7. Assuming a probability of about 40% for NEBULA to detect

1 neutron, the probability to detect 6 independent neutrons is about 95%. So the background reduction obtained with the NEBULA trigger is about 25%. This number could be refined after a complete analysis of the NEBULA data. Concerning the 6 neutron spectrum in 4.10(right), a similar reduction is observed in the positive energy region, while no gain is found at negative energies. In the following, we will apply the NEBULA trigger gate to all the energy spectra of section 4.2.4.

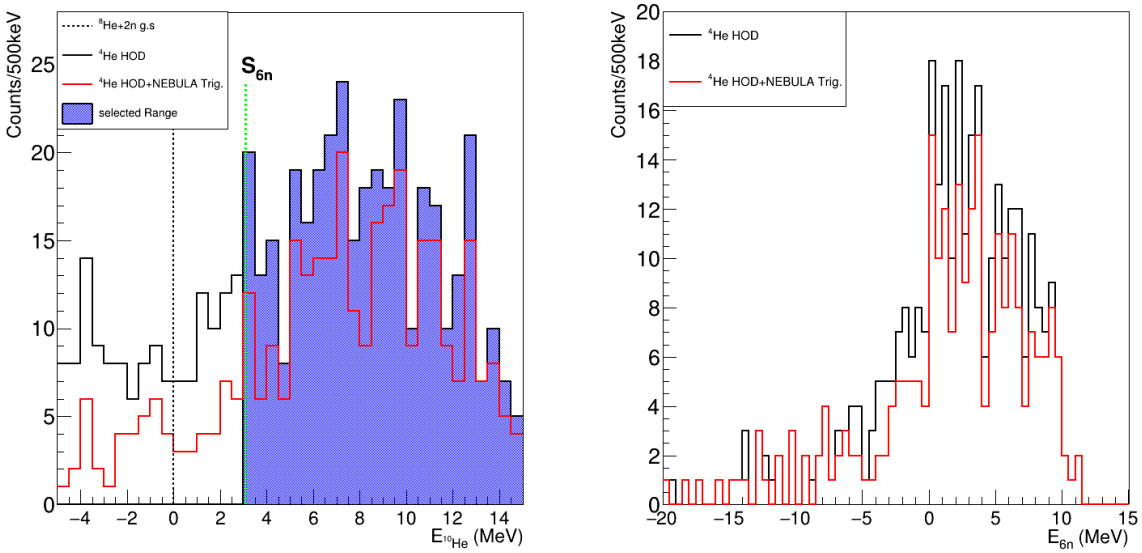


Figure 4.10: (left)^{10}He energy relative to the threshold of 2n emission with ^{4}He HOD gate without NEBULA trigger (black), with NEBULA trigger (red), and the blue shade represents the range of energies above threshold for 6n emission. (right) 6n spectrum corresponding to ^{10}He excitation energy covered by blue shade without NEBULA trigger (black), and with NEBULA trigger (red).

4.2.2 Resolution of 6-neutron energy spectra from simulation

The simulation of the 6n resolution follows a similar procedure as for ^{10}He (see section 4.1.3). The 6n energy is determined from the decay of ^{10}He into an alpha particle and 6-neutron system. Consequently, the 6n resolution depends not only on the detector resolutions for protons and alphas, but also on the angular resolution of the residue, and on the $B\rho$ resolution for the decay alpha.

The first step is to determine the four-momentum of ^{10}He (particle 3) from the reaction in Eq. 4.4. Particle 3 then decays into an alpha particle (3D1) and the 6-neutron system (3D2):

$$3 \rightarrow 3D1 + 3D2. \tag{4.10}$$

Following the notation from the ^{10}He simulation, the four-momentum of the undetected D2 can be reconstructed using momentum conservation:

$$\boldsymbol{P}_{3D2} = \boldsymbol{P}_{\mathrm{CM}} - \boldsymbol{P}_1 - \boldsymbol{P}_2 - \boldsymbol{P}_{3D1}, \tag{4.11}$$

where P_{CM} is the initial four-momentum, and P_1, P_2, and P_{3D1} are the measured final-state four-momenta.

The phase-space of the decay is simulated using ROOT's `TGenPhaseSpace` class [82], which generates the momenta of the decay products when provided with the parent four-momentum and daughter masses. For a given set of observables $(E_{\mathrm{beam}}, T_1, \theta_1, \phi_1, T_2, \theta_2, \phi_2)$, the procedure is as follows:

- Reconstruct the four-momentum of particle 3:

$$\boldsymbol{P}_3 = \boldsymbol{P}_{\mathrm{CM}} - \boldsymbol{P}_1 - \boldsymbol{P}_2, \tag{4.12}$$

  where P_{CM} is the initial state of the reaction.

- Generate the decay products of particle 3 using `TGenPhaseSpace`, providing the four-momentum of P_3 in its rest frame and the daughter masses.

- Boost both decay products (alpha and 6n) to the lab frame if the momenta are physically allowed.

- Compute the 6n energy using Eq. 4.9.

Random Gaussian variations are applied to the observables according to detector resolutions for protons and alphas, as well as the $B\rho$ resolution for the decay alpha to generate new data randomly from the one we had. Figure 4.11 shows the resulting 6n resolution simulation obtained with the used code. The black line is the simulation, while the red line corresponds to the same result scaled as in Fig. 4.4. We observe that the code predicts a slightly better energy resolution than for the ^{10}He spectrum, with a slightly decreasing trend with energy.

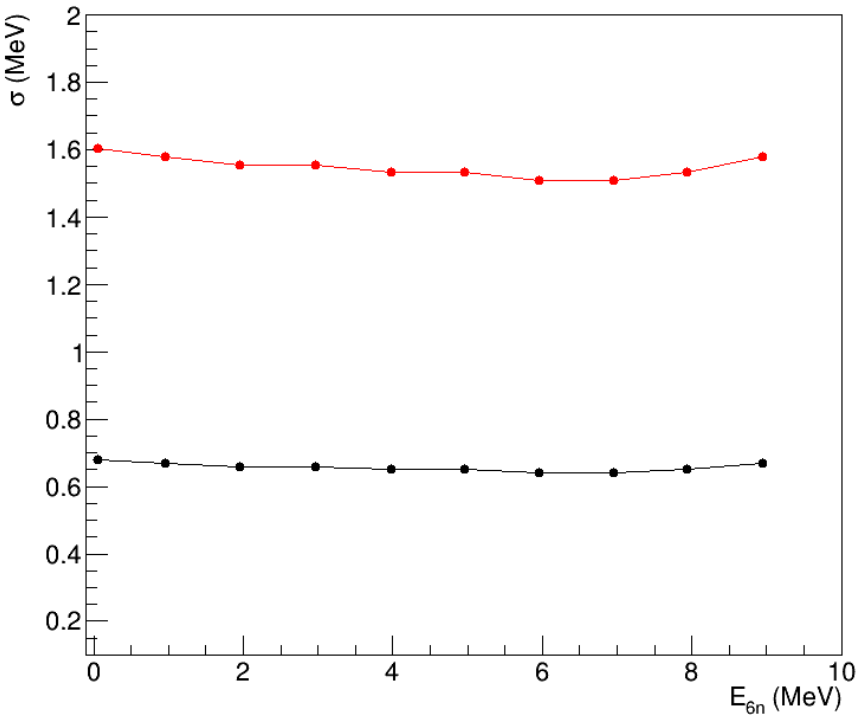


Figure 4.11: σ vs E_{6n} for the $6n$ simulation obtained from fitting each 1 MeV bin with a Gaussian (Black:pre correction, Red:post correction).

4.2.3 Phase-space calculation

One of the main expected contributions to the $6n$ missing mass spectrum is the 7-body phase-space of the alpha and 6-neutron system. Accordingly, a phase-space calculation code was used to compare the experimental data with the expected phase-space distribution, confirm the agreement between them, and identify any structure not seen in the calculation. More details about Lorentz invariant phase-space calculation are shown in Appendix B.

The phase-space calculation begins by generating the ^{10}He nucleus with a uniform distribution of excitation energy within the range obtained from the experimental data. A small experimental smearing of the ^{10}He lab energy is applied to mimic experimental conditions.

The decay is then performed in the ^{10}He center-of-mass (CM) frame. Six neutrons and one alpha particle are generated with random energies and directions (θ, ϕ), while strictly conserving total energy and momentum (formulae 4.13 and 4.14). The generation order of six neutrons and the alpha particle is

randomized for each event to ensure correct statistical sampling.

$$E_{tot} = M_{^{10}He} + E_{ex}(^{10}\text{He}) \tag{4.13}$$

$$\sum \vec{P} = 0 \tag{4.14}$$

The process is performed recursively such that at each step the following takes place:

- A particle is selected randomly (alpha or any of the 6 neutrons).
- Its energy and momentum are assigned randomly according to phase-space constraints.
- The remaining system is updated accordingly.

This procedure continues until all constituents of ^{10}He have been generated, and the full kinematics of the system is determined. The excitation energy of the 6n system is then calculated as the missing mass of the remaining system after the alpha particle has been removed as illustrated in Fig. 4.12.

Finally, the calculated quantities—neutron energies, 6n excitation energy, and ^{10}He excitation energy—are stored in ROOT histograms and a **TTree** for further analysis and comparison with experimental data. This method allows a direct comparison of the measured 6n spectrum with the pure phase-space expectation.

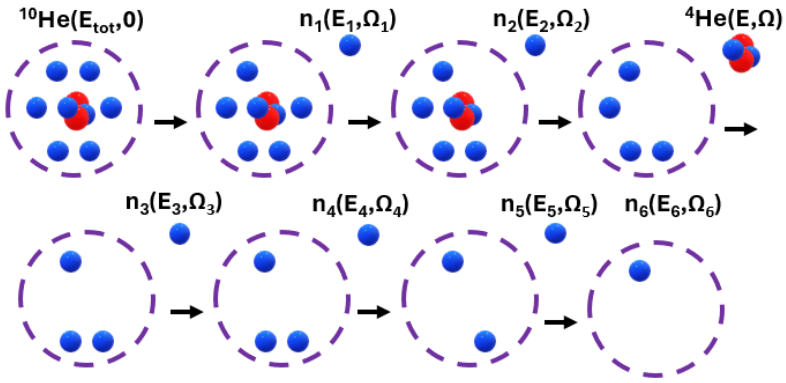


Figure 4.12: Example of recurring process taking place in the phase-space calculation code (E, and Ω are the energy and direction respectively).

4.2.3.1 6-neutron system phase-space

After the determination of the 6-neutron system excitation energy from the phase-space calculation, it was plotted against ^{10}He energy w.r.t.. the ^{8}He + 2n emission threshold. To compare it to the experimental data, three regions in the ^{10}He excitation energy were chosen. Figure 4.13 shows the plot of 6n energy from phase-space calculation vs. the corresponding energy in ^{10}He w.r.t. the ^{8}He + 2n emission with the three ranges of energy considered highlighted in different colors. As the separation energy of 6 free neutrons is $\sim$ 3.1 MeV, there can be no event generated below 3.1 MeV.

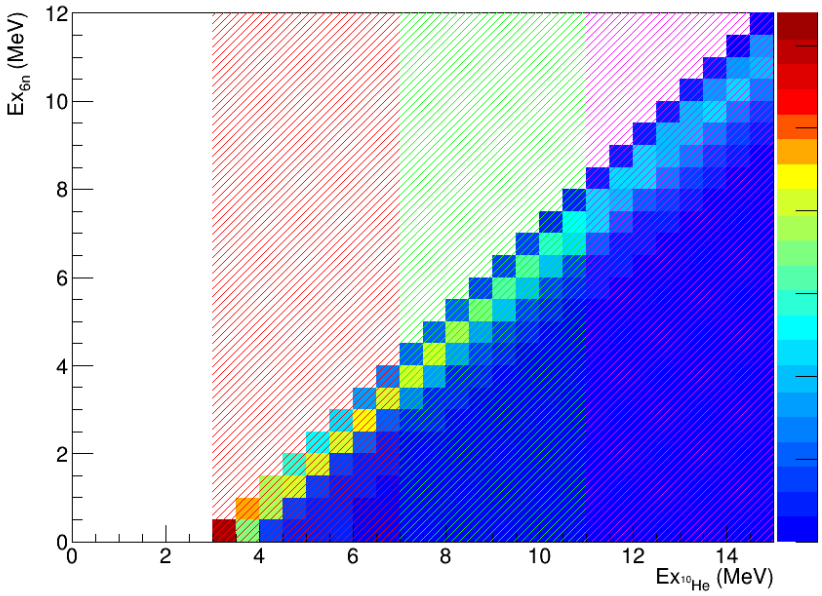


Figure 4.13: 6n energy from phase-space calculation vs. the corresponding energy in ^{10}He w.r.t. ^{8}He + 2n threshold with the three ranges of energy considered highlighted (Red:3-7 MeV, Green:7-11 MeV, and Violet:11-15 MeV).

To account for the resolution of the detection system, the phase space calculation result has been convoluted with a Gaussian with a sigma that is energy dependent and the value of sigma for each energy is interpolated from figure 4.11 (red).

Finally, the phase-space spectrum was normalized to match the data as described below.

4.2.4 Comparison of 6-neutron spectra with phase-space calculations

After the phase-space calculations were performed, the final step to study the 6-neutron spectra is to superimpose the phase-space and the real data and check for any extra structure. In a first step, the ^{10}He

spectrum was divided into 3 energy ranges in $E_{^{10}\mathrm{He}}$ above the separation energy for $6n$ ($\sim$ 3.1 MeV) [R_1 : 3 < $E_{^{10}\mathrm{He}}$ < 7 (MeV), R_2 : 7 < $E_{^{10}\mathrm{He}}$ < 11 (MeV), and R_3 : 11 < $E_{^{10}\mathrm{He}}$ < 15 (MeV)] and the corresponding $6n$ spectrum was investigated. The phase-space was normalized for region R_2 to minimize the overshoot of the phase space at higher energies. Then, the normalization for the other regions was performed relative to R_2 taking into account the statistics of each region in the ^{10}He spectrum. Figure 4.14 shows the ^{10}He excitation energy relative to the threshold of $2n$ emission with ^{4}He HOD gate and NEBULA trigger [left] and the $6n$ energy spectrum corresponding to the full ^{10}He energy range (0-15) MeV (red) and normalized phase-space (blue). To account for the different normalization factors for the phase-space depending on the energy range, the phase-space spectrum in Fig. 4.14 was constructed by summing the three normalized spectra from the three energy regions. As can be seen, the calculated phase-space spectrum reproduces the data in the high energy region but an excess of counts appears in the data, especially in the 0-3 MeV region. It appears useful to investigate the different energy regions as some resonances in ^{10}He might decay preferably to specific states of the $6n$ system.

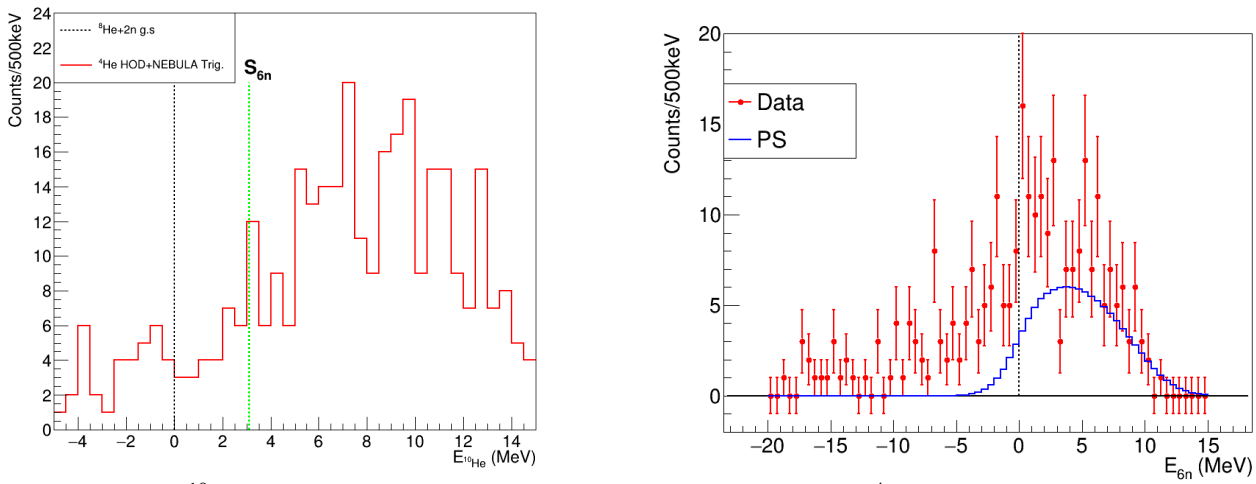


Figure 4.14: (left)^{10}He energy relative to the threshold of $2n$ emission with ^{4}He HOD gate and NEBULA trigger. (right) $6n$ spectrum corresponding to ^{10}He energy (0-15) MeV (red) and normalized phase-space (blue).

Firstly, looking at energy region R_1 (Fig. 4.15(b)), a peak-like structure below zero (~ -2.5 MeV) can be seen which needs further investigation. Only a weak excess of counts with respect to the calculated spectrum seems to appear near 0 MeV, the rest of the spectrum being reproduced by the calculation. We note that a cut seems to take place in the high energy region, whose origins is presently unclear, especially given the low statistics.

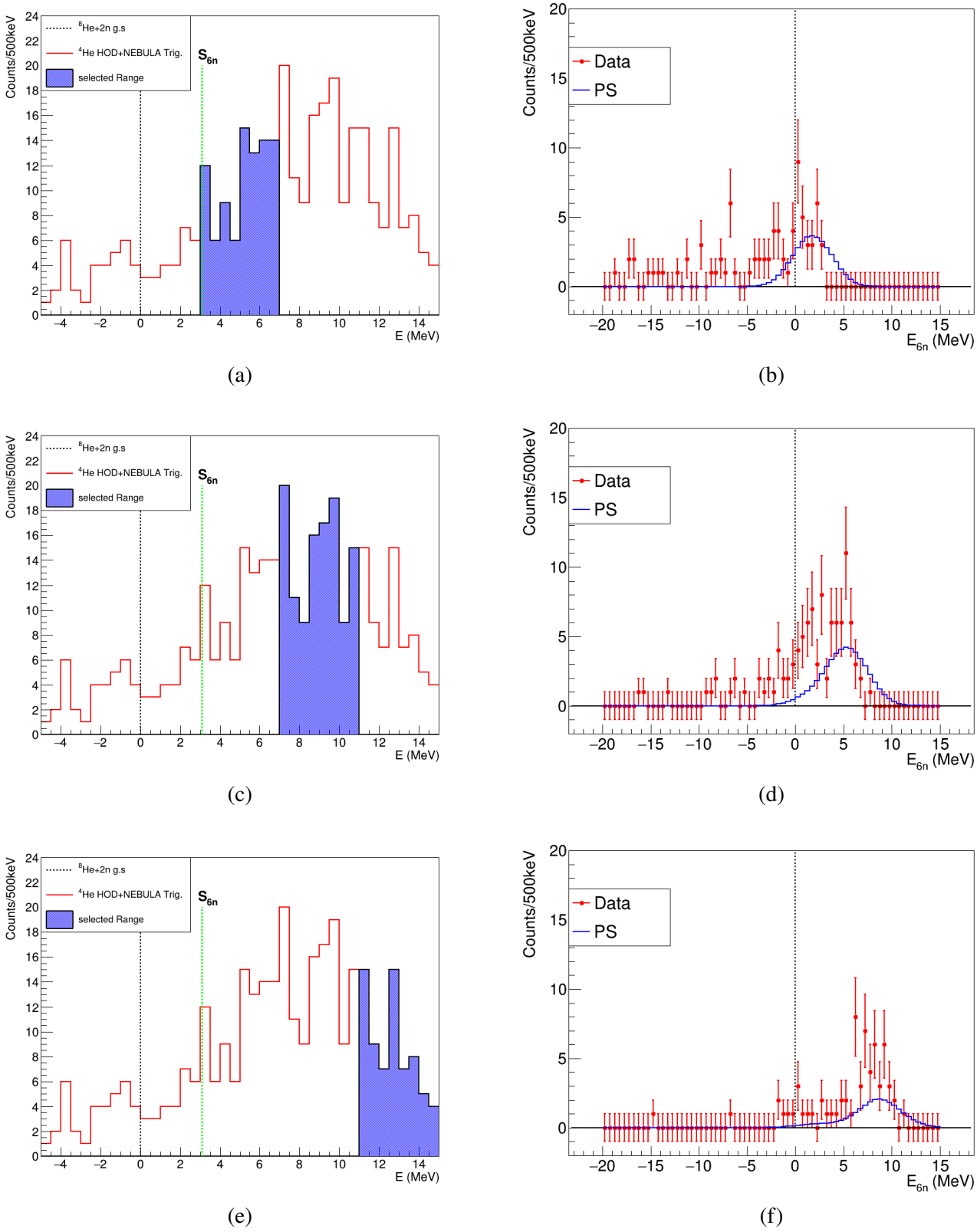


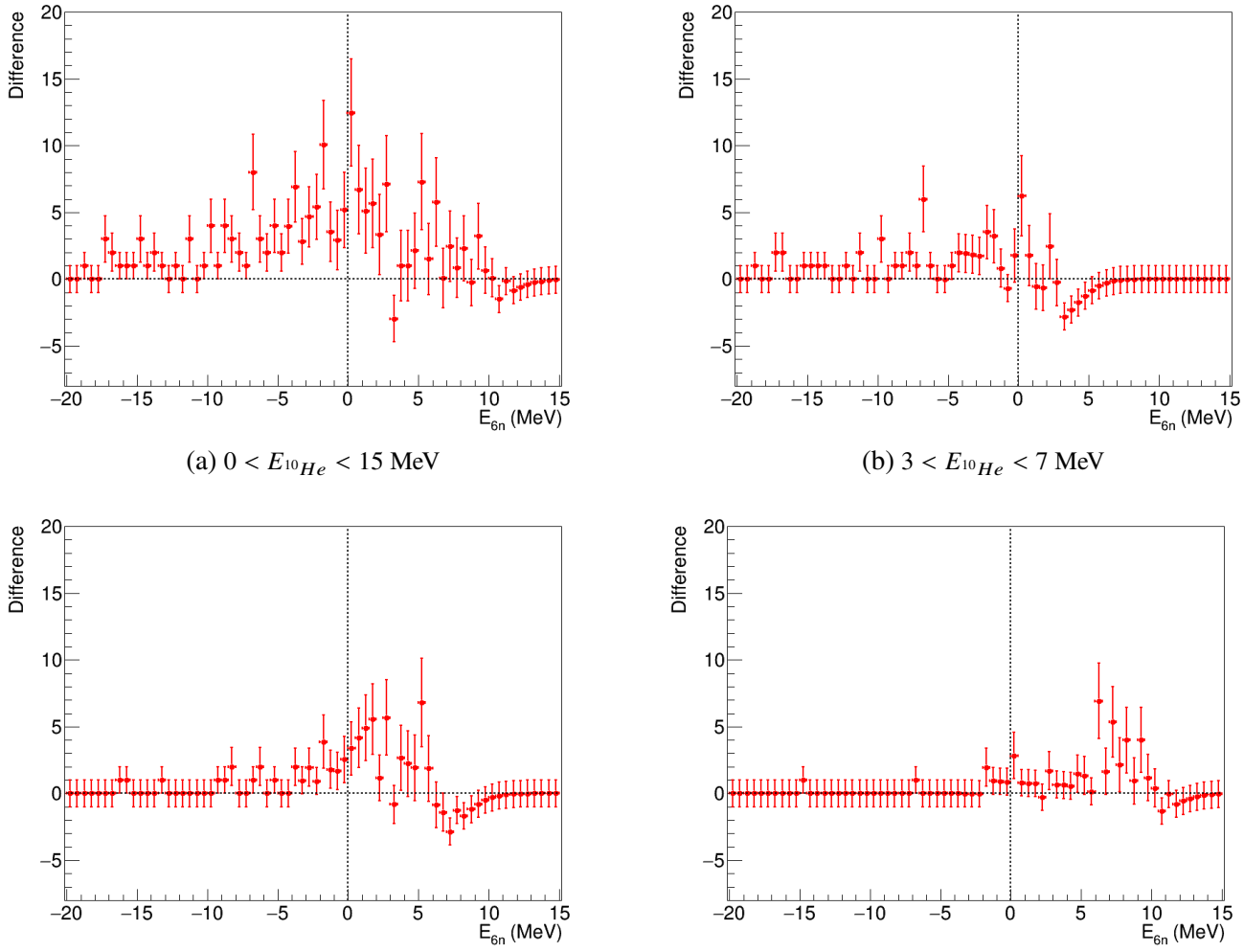
Figure 4.15: (left)^{10}He energy relative to the threshold of $2n$ emission with ^{4}He HOD gate with NEBULA trigger (red). (right) $6n$ spectrum corresponding to ^{10}He energy covered by blue shade (red) and normalized phase-space (blue). R_1:[a-b], R_2:[c-d], and R_3:[e-f].

Subsequently, observing energy region R_2 (Fig. 4.15(d)), the excess of counts in the 0-3 MeV region appears more clearly with the chosen normalization of the calculation. As for the peak-like structure in the bound region, it is no longer visible. Finally, for the energy region R_3 (Fig. 4.15(f)), the low positive energy region is relatively well-accounted for by the calculation, while a weak excess is seen near 6-8 MeV.

One way to confirm the presence of structures beyond the phase-space, is to subtract the phase-space spectra from the experimental ones. Figure 4.16(a) shows the difference between the experimental 6n spectrum corresponding to ^{10}He in the range (0-15) MeV and the corresponding phase-space (3-15) MeV. The same regions of energy ($R_1 - R_3$) were investigated in Fig. 4.16 [(b) - (d)]. The excess of counts in the 0-3 MeV region is confirmed for R_2 only, as well as the weak signal near 6-8 MeV for R_3.

As for the peak-like structure observed in the bound region at ~ -2 MeV, further examination of the negative energy region is needed to understand. To investigate the peak-like structures found in the negative energy region, we consider the 6n energy spectra corresponding to ^{10}He energies below the separation energy of alpha + six free neutrons as shown in Fig. 4.17 and 4.18. At first glance, peak-like structures can be observed at ~ -1.5 MeV for the energy region (0-3) MeV, and at ~ -6.5 for the energy region (-5-3) MeV. Although, the peak-like structure observed in Fig. 4.16 (a) and (b) might be interpreted as a bound 6-neutrons system, we find that considering the extreme case of very negative energies, we observe in Fig. 4.18 that the background of Fig. 4.2 clearly creates structures in the very bound region of the 6-neutron spectrum which is highly improbable. We note that if a bound 6-neutron state were to exist at such low energy, then ^{19}B (invariant mass of 17758.162 MeV/c^2) could instantaneously decay into ^{13}B + 6n if the 6n would be bound by more than 5.22 MeV. However, the decay of ^{19}B to such a peculiar configuration as ^{13}B + 6n could be strongly suppressed. The fact that the counts at very negative ^{10}He energies can create background structures in the 6n spectrum implies that the excess of counts in the 0-3 MeV region of the 6n spectrum may have a similar origin to background present in the positive region of the ^{10}He spectrum, as discussed above. Further analysis is needed to remove the background and more firmly conclude.

To summarize, the 6n energy spectrum resulting from the decay of resonances in ^{10}He into an alpha and six neutrons showed an overall agreement with the phase-space calculations with additional peak-like structures in the bound and unbound regions. Further investigation was carried out using three regions of energy in ^{10}He to investigate the 6n spectrum. An excess of counts with respect to the phase-space



(a) $0 < E_{^{10}He} < 15$ MeV

(b) $3 < E_{^{10}He} < 7$ MeV

(c) $7 < E_{^{10}He} < 11$ MeV

(d) $11 < E_{^{10}He} < 15$ MeV

Figure 4.16: Experimental 6n excitation energy obtained after the subtraction of the phase-space calculation for different energy range regions of ^{10}He w.r.t. ^{8}He + 2n energy.

calculation was found in the 0-3 MeV positive 6n energy region but the low statistics clearly limit the conclusions that our study can bring. As for the peak-like structures in the bound region we found that the background observed down to very negative energies in ^{10}He can actually create such structures. Further attempts to reduce the background are mandatory to bring more definite conclusions.

The next step in the analysis of this dataset would be analyzing NEBULA data, using the ToF of neutrons obtained through NEBULA to separate neutrons from gamma rays while the charged particles can be removed by the VETO detectors. Furthermore, the source of the background clearly seen in the ^{4}He channel at negative energies in ^{10}He (Fig. 4.2) needs to be investigated and possible gates could be applied to remove it. Finally, the effect of the vertical angular acceptance of the SAMURAI magnet needs

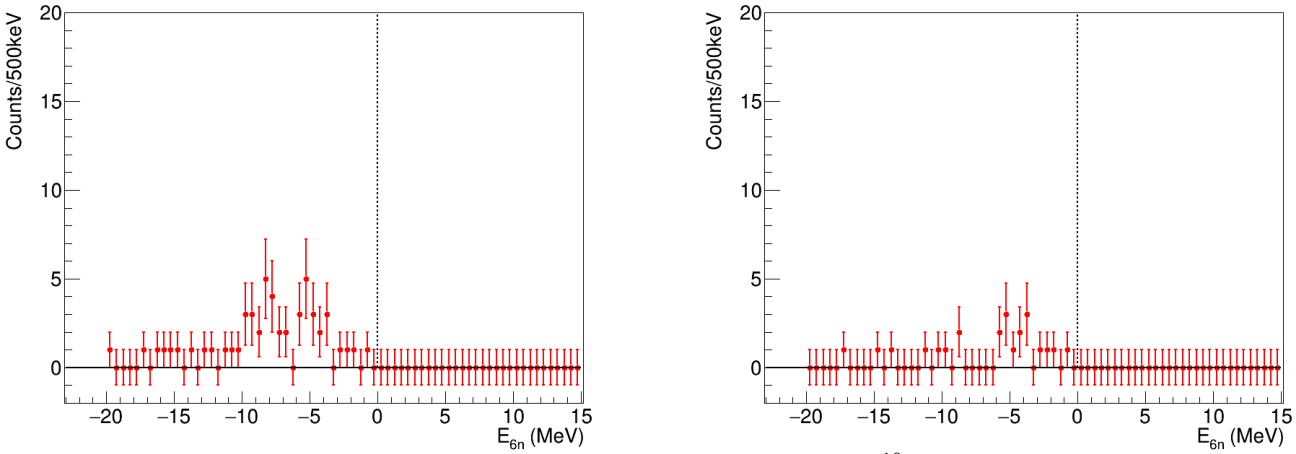


Figure 4.17: Experimental 6*n* excitation energy spectrum corresponding to ^{10}He energy $-5 < E_{^{10}He} < 3$ MeV (left) and $0 < E_{^{10}He} < 3$ MeV (right).

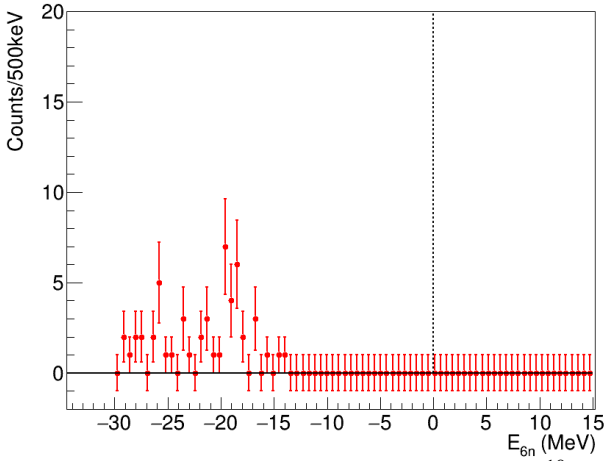


Figure 4.18: Experimental 6*n* excitation energy spectrum corresponding to ^{10}He energy $-20 < E_{^{10}He} < -10$ MeV.

to be estimated more precisely as it will affect the phase space calculations, although a first check showed that the vertical acceptance does not significantly cut the decaying alphas.

Chapter 5

Conclusions and perspectives

5.1 Conclusions

The first 6-neutron energy spectrum was obtained using the SAMURAI spectrometer at RIKEN from the decay of resonances in ^{10}He populated through the $(p, p\alpha)$ reaction with a ^{14}Be beam impinging on a solid hydrogen target. The recoil protons were detected by the ESPRI setup covering an angular range $50° - 70°$ in the lab system. The setup detected the scattering angle using drift chambers and identified the particles using plastic scintillators using the $\Delta E - ToF$ method. A NaI(Tl) scintillation detector used for detecting remaining energy of the protons was utilized for the calibration of the ToF of the plastic. The energy of the proton was determined using the ToF of the plastic which doubled the statistics as it recovered events lost due to geometrical efficiency of the NaI(Tl). The knocked-out alpha particle was detected by the Telescope system covering an angular range $4° - 12°$ in the lab system. The Telescope setup utilized DSSD modules to detect the position and energy loss of the scattering alpha, followed by CsI(Tl) scintillators to recover the total energy of the alpha and perform particle identification using the $\Delta E - E$ method.

The ^{10}He residue observables were determined using the missing mass method. The four-vector of the alpha from the decay of the ^{10}He was determined using $B\rho$ calculation which utilized position information of a drift chamber located downstream from the target and another one after the SAMURAI magnet. Excitation energy of ^{10}He w.r.t threshold of ^{8}He + $2n$ was computed and resonances in ^{10}He were fitted using the Voigt function. The fit had a first resonance energy of $E_1 = 1.42(08)$ MeV with width

$\Gamma_1 = 1.28(10)$ MeV and a second resonance was found at $E_2 = 4.00(20)$ MeV with a width $\Gamma_2 = 0.75(138)$ MeV; both results agree within error with the resonances found by [73] and a third resonance found by [75] was used as a fixed parameter ($E_3 = 6.3$ MeV, $\Gamma_3 = 3.2$ MeV) as it improved the overall reduced χ^2 (reduced $\chi^2 = 1.35$).

The 6-neutron system excitation energy spectra have been obtained for the first time and compared to phase-space calculations. While the calculations reproduce the gross features of the data, they fail to account for the 6*n* spectrum in the 0-3 MeV region, especially for the ^{10}He energy range where the cross-section is the highest. Peak-like structures are observed in the bound-state region, which could be due to the contribution of the background in the alpha-decaying channel. Further investigations are definitely needed to attempt reducing the background.

5.2 Prospective

Further analysis of the data is planned. Namely, a background reduction is needed to reach the final conclusion on the present data of the 6-neutron system. This could be done by analyzing NEBULA data to obtain the neutrons' ToF and separate the neutrons from the gamma-rays and reject charged particles using the VETO detectors to have a better NEBULA trigger. Another prospective is to investigate the source of the background in the ^{4}He decay channel and find a way to remove it. Afterwards, the acceptance of the SAMURAI magnet could be studied and included in the phase-space calculations. Concerning ^{10}He, in the near future the branching ratios will be extracted and compared to structure calculations to provide information on the N-body structure of the populated resonances. On the experimental side, another experiment aiming to study resonances in ^{10}He and the decay channel of ^{4}He+6*n* has been performed at SAMURAI/RIKEN and is currently under analysis. Another experiment was recently performed at SAMURAI/RIKEN with higher neutron detection capabilities that aims to detect the 6 neutrons in coincidence. On the theory side, an exact calculation for the 6-neutron system is currently being performed by Hiyama et al.[83].

Appendix A

Three-body Kinematics

The SAMURAI12 experimental setup allows the detection of the recoil protons and scattered alpha from the quasi-free scattering $(p, p\alpha)$ reaction using ESPRI, and telescope setups respectively. This allows the detection of the polar and azimuthal angles of the protons (θ_1, ϕ_1) and scattering alphas (θ_2, ϕ_2) via the position measurements of particles 1 and 2 respectively. Using the three-body kinematics, two kinematic solutions for the energy of particle 2 can be obtained [84].

Considering the reaction in equation 4.4, if T_1 and (θ_1, ϕ_1) are determined in the lab frame, then the energy and momentum of the combined system of particle 2 and 3 (denoted as R23) can be expressed as

$$E_{23} = E_{CM} - E_1 \tag{A.1}$$

$$P_{23} = |\overrightarrow{P}_{CM} - \overrightarrow{P}_1| = (P_{CM}^2 + P_1^2 - 2P_{CM}P_1 cos\theta_1)^{1/2} \tag{A.2}$$

The angle θ_{23} of the R23 system with respect to the z-axis in the lab frame is expressed as

$$sin\theta_{23} = P_1 sin\theta_1 / P_{23} \tag{A.3}$$

$$cos\theta_{23} = (P_{CM} - P_1 cos\theta_1)/P_{23} \tag{A.4}$$

As the energy, momentum, and angle of the system R23 can be determined from the previous formulae, the three-body kinematics problem can be simplified to a two-body kinematics problem and it is possible

to solve for P_2. By expressing the energy and momentum of particle 2 in system R23 in terms of invariant mass M_{23} we obtain

$$P_2^{R23} = \lambda^{1/2}(M_{23}^2, m_2^2, m_3^2)/(2M_{23}) \tag{A.5}$$

$$E_2^{R23} = (M_{23}^2 + m_2^2 - m_3^2)/(2M_{23}) \tag{A.6}$$

such that

$$\begin{aligned} M_{23}^2 &= (E_2 + E_3)^2 - (\overrightarrow{P}_2 - \overrightarrow{P}_3)^2 \\ &= (E_{CM} - E_1)^2 - (\overrightarrow{P}_{CM} - \overrightarrow{P}_1)^2 \\ &= M_{CM}^2 + m_1^2 - 2E_{CM}E_1 + 2P_{CM}P_1 cos\theta_1 \end{aligned} \tag{A.7}$$

where the function $\lambda(x, y, z)$ is defined as $\lambda(x, y, z) = x^2 + y^2 + z^2 - 2xy - 2yz - 2zx$. Subsequently, the energy, momentum and angle of particle 2 can be determined from that of system R23 through Lorentz transformation between these two frames. The Lorentz transformation can be written as the following [51]:

$$\begin{aligned} E_2^{R23} &= -\gamma\beta P_2 cos\theta_2' + \gamma E_2 \\ &= -\gamma\beta P_2 cos\theta_2' + \gamma(P_2^2 + m_2^2)^{1/2} \end{aligned} \tag{A.8}$$

where $\beta = P_{23}/E_{23}$ and $\gamma = P_{23}/M_{23}$ and the angle θ_2' is measured with respect to the z-axis of the R23 system with $cos\theta_2'$ given as

$$cos\theta_2' = (P_{CM}cos\theta_2 - P_1 cos\theta_{1-2})/P_{23} \tag{A.9}$$

$$cos\theta_{1-2} = cos\theta_1 cos\theta_2 + sin\theta_1 sin\theta_2 cos(\phi_2 - \phi_1) \tag{A.10}$$

Finally, the solution of P_2 can be expressed as

$$P_2 = (-B \pm \sqrt{B^2 - 4AC})/2A \tag{A.11}$$

where

$$A = \gamma^2(1 - \beta^2 cos^2\theta_2') \tag{A.12}$$

$$B = -2E_2^{R23}\gamma\beta cos\theta_2' \tag{A.13}$$

$$C = \gamma^2 m_2^2 - (E_2^{R23})^2 \tag{A.14}$$

Both solutions of the quadratic equations are allowed physically when the discriminant of the quadratic equations is satisfied. The discriminant can be simplified into [51]:

$$\beta^2 \gamma^2 sin^2 \theta_2^{R23} = (\gamma_2^{R23})^2 - 1 \tag{A.15}$$

where $\gamma_2^{R23} = E_2^{R23}/M_2^{R23}$.

Appendix B

Lorentz Invariant Phase Space calculation

This simulation was provided by I. Stefan with the source code and all related information available on [85].

Phase Space Derivation with 3D Momentum-Sphere Diagram

The differential volume in momentum space is

$$d^3\vec{p} = dp_x\, dp_y\, dp_z.$$

In spherical coordinates:

$$p_x = p\sin\theta\cos\phi, \quad p_y = p\sin\theta\sin\phi, \quad p_z = p\cos\theta,$$

the Jacobian gives

$$dp_x\, dp_y\, dp_z = p^2\, dp\, \sin\theta\, d\theta\, d\phi = p^2\, dp\, d\Omega,$$

with $d\Omega = \sin\theta\, d\theta\, d\phi$.

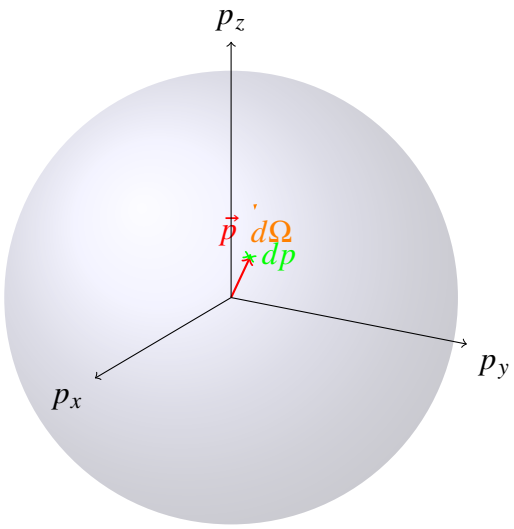
For a relativistic particle of mass m, $E = \sqrt{p^2 + m^2}$, so

$$dp = \frac{E}{p}\, dE \quad \Rightarrow \quad p^2\, dp = p\, E\, dE.$$

Thus, the phase space element in energy and solid angle is

$$\boxed{dN \propto p\, E\, dE\, d\Omega}.$$

3D Momentum Sphere Illustration



This diagram represents:

- The red vector $\vec{p}$ is the momentum of the particle.
- The green arrow shows the shell thickness dp.
- The orange triangle is a small patch corresponding to the solid angle element $d\Omega = \sin\theta\, d\theta\, d\phi$.

Phase Space Derivation and Uniform Momentum Distribution

For a single particle of mass m, the number of available quantum states in a small momentum volume $d^3\vec{p}$ is proportional to

$$dN \propto d^3\vec{p} = dp_x\, dp_y\, dp_z. \tag{B.1}$$

Switching to spherical coordinates,

$$d^3\vec{p} = p^2\, dp\, d\Omega, \tag{B.2}$$

where $p = |\vec{p}|$ and $d\Omega = \sin\theta\, d\theta\, d\phi$ is the solid angle.

For a relativistic particle,

$$E = \sqrt{p^2 + m^2} \quad \Rightarrow \quad dp = \frac{E}{p} dE, \tag{B.3}$$

so the number of states in energy space becomes

$$dN \propto p^2\, dp\, d\Omega = pE\, dE\, d\Omega. \tag{B.4}$$

This shows that in the microcanonical ensemble, all states with the same total energy are equally probable, and therefore the generator should sample the momentum space *uniformly*. Generating energies with probability proportional to p ensures this uniformity in momentum space.

Phase Space Volume Element

The number of quantum states for a free particle of momentum $\vec{p}$ in a volume V (with periodic boundary conditions) is proportional to the volume element in its momentum space. In the continuum limit, the density of states per unit volume in momentum space is

$$dN \;\propto\; d^3\vec{p}.$$

Spherical coordinates give

$$d^3\vec{p} = p^2\, dp\, d\Omega,$$

with $p = |\vec{p}|$ and $d\Omega = \sin\theta\, d\theta\, d\varphi$. Thus

$$dN \;\propto\; p^2\, dp\, d\Omega.$$

This expresses that for an isotropic system the number of states at momentum magnitude p increases as p^2 due to the growing surface area of the sphere of radius p in momentum space ("shell counting").

In relativistic particle decay, the phase-space element for an n-body final state is

$$d\Phi_n(P;\{p_i\}) \;=\; (2\pi)^4\,\delta^4\!\Big(P-\sum_i p_i\Big)\prod_{i=1}^{n}\frac{d^3\vec{p}_i}{2E_i},$$

where $d^3\vec{p}_i$ is the invariant momentum space volume for particle i. This enters directly into decay rate formulas such as Fermi's Golden Rule [B5].

If all directions are equally likely, angles are sampled uniformly in $\cos\theta$ and φ, and p is sampled with weight proportional to p^2 (or equivalently the kinetic energy density if converting variables). This ensures uniform distribution in spatial momentum space consistent with the underlying statistical mechanics postulate of equal a priori probabilities. [B6]

References

1. R. Hagedorn, *Statistical Thermodynamics of Strong Interactions*, Nuovo Cimento 35 (1965) 395–431.

2. J.J. Sakurai, *Advanced Quantum Mechanics*, Ch. 4, Addison-Wesley (1967).

3. G.F. Bertsch, *Nuclear Physics in a Nutshell*, Princeton University Press, 2007, Section 5.1.

4. K.S. Krane, *Introductory Nuclear Physics*, Wiley, 1987, Chapter 7.

5. "Particle decay", Wikipedia, https://en.wikipedia.org/wiki/Particle_decay

6. https://web.stanford.edu/peastman/statmech/phasespace.html

Bibliography

[1] B. Povh et al. *Particles and Nuclei: An Introduction to the Physical Concepts*. Berlin: Springer, 1999.

[2] F. M. Marquès. "The extremes of neutron richness". In: *Eur. Phys. J. Plus* 136.594 (2021). DOI: 10.1140/epjp/s13360-021-01556-z.

[3] I. Tanihata, H. Savajols, and R. Kanungo. "Recent experimental progress in nuclear halo structure studies". In: *Prog. Part. Nucl. Phys.* 68 (2013), pp. 215–313. DOI: 10.1016/j.ppnp.2012.07.001.

[4] W. Glöckle. "S-matrix pole trajectory in a three-neutron model". In: *Phys. Rev. C* 18.1 (1978), pp. 564–572. DOI: 10.1103/PhysRevC.18.564.

[5] R. Offermann and W. Glöckle. "Is there a three-neutron resonance?" In: *Nucl. Phys. A* 318.1 (1979), pp. 138–144. ISSN: 0375-9474. DOI: 10.1016/0375-9474(79)90475-5.

[6] H. Witała and W. Glöckle. "Resonances in the three-neutron system". In: *Phys. Rev. C* 60.2 (1999), p. 024002. DOI: 10.1103/PhysRevC.60.024002.

[7] A. Hemmdan, W. Glöckle, and H. Kamada. "Indications for the nonexistence of three-neutron resonances near the physical region". In: *Phys. Rev. C* 66.5 (2002), p. 054001. DOI: 10.1103/PhysRevC.66.054001.

[8] R. Lazauskas and J. Carbonell. "Three-neutron resonance trajectories for realistic interaction models". In: *Phys. Rev. C* 71.4 (2005), p. 044004. DOI: 10.1103/PhysRevC.71.044004.

[9] R. Lazauskas and J. Carbonell. "Is a physically observable tetraneutron resonance compatible with realistic nuclear interactions?" In: *Phys. Rev. C* 72.3 (2005), p. 034003. DOI: 10.1103/PhysRevC.72.034003.

[10] S. C. Pieper. “Can Modern Nuclear Hamiltonians Tolerate a Bound Tetraneutron?” In: *Phys. Rev. Lett.* 90.25 (2003), p. 252501. DOI: 10.1103/PhysRevLett.90.252501.

[11] A. M. Shirokov et al. “Prediction for a Four-Neutron Resonance”. In: *Phys. Rev. Lett.* 117.18 (2016), p. 182502. DOI: 10.1103/PhysRevLett.117.182502.

[12] S. Gandolfi et al. “Is a Trineutron Resonance Lower in Energy than a Tetraneutron Resonance?” In: *Phys. Rev. Lett.* 118.23 (2017), p. 232501. DOI: 10.1103/PhysRevLett.118.232501.

[13] K. Fossez et al. “Can Tetraneutron be a Narrow Resonance?” In: *Phys. Rev. Lett.* 119.3 (2017), p. 032501. DOI: 10.1103/PhysRevLett.119.032501.

[14] J. G. Li et al. “Ab initio no-core Gamow shell-model calculations of multineutron systems”. In: *Phys. Rev. C* 100.5 (2019), p. 054313. DOI: 10.1103/PhysRevC.100.054313.

[15] E. Hiyama et al. “Possibility of generating a 4-neutron resonance with a $T = 3/2$ isospin 3-neutron force”. In: *Phys. Rev. C* 93.4 (2016), p. 044004. DOI: 10.1103/PhysRevC.93.044004.

[16] L. Wu et al. “Searching for the Tetraneutron Resonance on the Lattice”. In: *Phys. Rev. Lett.* 136.14 (2026), p. 142502. DOI: 10.1103/89w9-p443.

[17] F. M. Marquès and J. Carbonell. “The quest for light multineutron systems”. In: *Eur. Phys. J. A* 57.3 (2021), p. 105. DOI: 10.1140/epja/s10050-021-00417-8.

[18] F. M. Marquès et al. “Detection of neutron clusters”. In: *Phys. Rev. C* 65 (2002), p. 044006. DOI: 10.1103/PhysRevC.65.044006.

[19] F. M. Marquès, R. Guardiola, and J. Navarro. “Halo structure of ^{14}Be”. In: *Phys. Rev. Lett.* 86 (2001), p. 600. DOI: 10.1103/PhysRevLett.86.600.

[20] F. M. Marquès et al. “Neutron cross-talk rejection in a modular array and the detection of halo neutrons”. In: *Nucl. Instrum. Methods A* 450 (2000), pp. 109–113. DOI: 10.1016/S0168-9002(00)00248-5.

[21] M. Labiche. “Etude de la structure du noyau ^{14}Be et de son halo neutronique”. PhD thesis. Université de Caen, 1999.

[22] F. M. Marquès et al. "On the possible detection of 4*n* events in the breakup of ^{14}Be". In: (2005). DOI: 10.48550/arXiv.nucl-ex/0504009. arXiv: nucl-ex/0504009.

[23] E. Rich. "Recherche de l'existence éventuelle du tétraneutron via la réaction de transfert d'alpha ^{8}He(d,^{6}Li)4*n*". PhD thesis. Université Sciences et Technologies - Bordeaux I, 2005.

[24] D. Beaumel et al. "Studies of Exotic Systems Using Transfer Reactions at GANIL". In: *Proc. International Symposium on Physics of Unstable Nuclei (ISPUN 07)*. 2008, pp. 18–25. DOI: 10.1142/9789812776150_0003.

[25] K. Kisamori et al. "Candidate Resonant Tetraneutron State Populated by the ^{4}He(^{8}He,^{8} Be) Reaction". In: *Phys. Rev. Lett.* 116.5 (2016), p. 052501. DOI: 10.1103/PhysRevLett.116.052501.

[26] T. Uesaka et al. "Experimental study of the structure of neutron-rich nuclei near the drip line using the SHARAQ spectrometer". In: *Prog. Theor. Exp. Phys.* 2012 (2012), p. 03C007. DOI: 10.1093/ptep/pts055.

[27] M. Duer et al. "Observation of a correlated free four-neutron system". In: *Nature* 606 (2022), pp. 678–682. DOI: 10.1038/s41586-022-04827-6.

[28] M. V. Zhukov, A. A. Korsheninnikov, and M. H. Smedberg. "Simplified α+4n model for the ^{8}He nucleus". In: *Phys. Rev. C* 50.1 (1994), R1–R4. DOI: 10.1103/PhysRevC.50.R1.

[29] L. V. Grigorenko, N. K. Timofeyuk, and M. V. Zhukov. "Broad states beyond the neutron drip line". In: *Eur. Phys. J. A* 19.2 (2004), pp. 187–201. DOI: 10.1140/epja/i2003-10124-1.

[30] R. Lazauskas, E. Hiyama, and J. Carbonell. "Low Energy Structures in Nuclear Reactions with 4*n* in the Final State". In: *Phys. Rev. Lett.* 130.10 (2023), p. 102501. DOI: 10.1103/PhysRevLett.130.102501.

[31] RIKEN Nishina Center. *RI Beam Factory Accelerator Overview*. https://www.nishina.riken.jp/ribf/accelerator/overview.html.

[32] T. Kubo et al. "Development of a high-field superconducting magnet for the SHARAQ spectrometer". In: *IEEE Trans. Appl. Supercond.* 17 (2007), pp. 1069–1072. DOI: 10.1109/TASC.2007.898727.

[33] K. Miki et al. "Precise Spectroscopy of the $3n$ and $3p$ Systems via the ^{3}H(t, ^{3}He)$3n$ and ^{3}He(^{3}He, t)$3p$ Reactions at Intermediate Energies". In: *Phys. Rev. Lett.* 133.1 (2024), p. 012501. DOI: 10.1103/PhysRevLett.133.012501.

[34] K. Miki et al. "Development and fabrication of a thick Ti-3H target for the ^{3}H(t,^{3}He)$3n$ experiment at intermediate energies". In: *Nucl. Instrum. Methods A* 1056 (2023), p. 168583. DOI: 10.1016/j.nima.2023.168583.

[35] M. Ichimura. *Computer code PROD3N*. Computer code. 2016.

[36] V. G. J. Stoks et al. "Partial-wave analysis of all nucleon-nucleon scattering data below 350 MeV". In: *Phys. Rev. C* 48.2 (1993), pp. 792–815. DOI: 10.1103/PhysRevC.48.792.

[37] A. Obertelli et al. "MINOS: A vertex tracker coupled to a thick liquid-hydrogen target for in-beam spectroscopy of exotic nuclei". In: *Eur. Phys. J. A* 50.1 (2014), p. 8. DOI: 10.1140/epja/i2014-14008-y.

[38] C. Santamaria et al. "Tracking with the MINOS Time Projection Chamber". In: *Nucl. Instrum. Methods A* 905 (2018), pp. 138–148. ISSN: 0168-9002. DOI: 10.1016/j.nima.2018.07.053.

[39] T. Kobayashi et al. "SAMURAI spectrometer for RI beam experiments". In: *Nucl. Instrum. Methods B* 317 (2013), pp. 294–304. DOI: 10.1016/j.nimb.2013.05.089.

[40] H. Sato et al. "Superconducting Dipole Magnet for SAMURAI Spectrometer". In: *IEEE Trans. Appl. Supercond.* 23.3 (2013), p. 4500308. DOI: 10.1109/TASC.2012.2237225.

[41] K. Boretzky et al. "NeuLAND: The high-resolution neutron time-of-flight spectrometer for R3B at FAIR". In: *Nucl. Instrum. Methods A* 1014 (2021), p. 165701. ISSN: 0168-9002. DOI: 10.1016/j.nima.2021.165701.

[42] T. Nakamura and Y. Kondo. "Large acceptance spectrometers for invariant mass spectroscopy of exotic nuclei and future developments". In: *Nucl. Instrum. Methods B* 376 (2016), pp. 156–161. ISSN: 0168-583X. DOI: 10.1016/j.nimb.2016.01.003.

[43] T. Faestermann et al. "Indications for a bound tetraneutron". In: *Phys. Lett. B* 824 (2022), p. 136799. ISSN: 0370-2693. DOI: 10.1016/j.physletb.2021.136799.

[44] M. Löffler, H. J. Scheerer, and H. Vonach. "The ion optical properties of the Munich Q3D-spectrograph investigated by means of a special experimental ray tracing method". In: *Nucl. Instrum. Methods* 111.1 (1973), pp. 1–12. ISSN: 0029-554X. DOI: 10.1016/0029-554X(73)90090-6.

[45] G. Dollinger and T. Faestermann. *Physics at the Munich Tandem accelerator laboratory*. 2018. arXiv: 1802.07057 [physics.ins-det]. URL: https://arxiv.org/abs/1802.07057.

[46] C. Albrecht et al. *Jahresbericht 1993, Beschleunigerlabor der LMU und TU München*. Technical Report. Ludwig-Maximilians-Universität München and Technische Universität München, Beschleunigerlabor, 1994.

[47] P. Neumaier et al. "High-resolution elastic recoil detection utilizing Bayesian probability theory". In: *Nucl. Instrum. Methods B* 183.1 (2001). Ion Beam Techniques with Atomic Layer Resolution, pp. 48–61. ISSN: 0168-583X. DOI: 10.1016/S0168-583X(01)00347-0.

[48] R. Guardiola and J. Navarro. "Correlated basis function study of neutron matter". In: *Phys. Rev. Lett.* 84 (2000), pp. 1144–1147. DOI: 10.1103/PhysRevLett.84.1144.

[49] G. S. Anagnostatos. "On the Possible Stability of Tetraneutrons and Hexaneutrons". In: *Int. J. Mod. Phys. E* 17.8 (2008), pp. 1557–1575. DOI: 10.1142/S0218301308010568.

[50] Y. Yano. "The RIKEN RI Beam Factory Project: A status report". In: *Nucl. Instrum. Methods B* 261 (2007), pp. 1009–1013. DOI: 10.1016/j.nimb.2007.04.174.

[51] P. Li. "Cluster Structure of Neutron-Rich Beryllium Isotopes Investigated via (p,pα) Reaction in Inverse Kinematics at 150 MeV/u". PhD thesis. The University of Hong Kong, 2021.

[52] T. Kubo. "In-flight RI beam separator BigRIPS at RIKEN and elsewhere in Japan". In: *Nucl. Instrum. Methods B* 204 (2003), pp. 97–113. DOI: 10.1016/S0168-583X(02)01896-7.

[53] Y. Matsuda et al. "Large, thin solid hydrogen target using para-H_2". In: *Nucl. Instrum. Methods A* 643 (2011), pp. 6–10. DOI: 10.1016/j.nima.2011.04.022.

[54] H. Suzuki et al. "Production Cross Section Measurements of Radioactive Isotopes by BigRIPS Separator at RIKEN RI Beam Factory". In: *Nucl. Instrum. Methods B* 317 (2013), pp. 756–768.

[55] H. Ryuto et al. “Liquid hydrogen and helium targets for radioisotope beams at RIKEN”. In: *Nucl. Instrum. Methods A* 555.1 (2005), pp. 1–5. DOI: 10.1016/j.nima.2005.08.102.

[56] A. Obertelli and T. Uesaka. “Hydrogen targets for exotic-nuclei studies developed over the past 10 years”. In: *Eur. Phys. J. A* 47 (2011), p. 105. DOI: 10.1140/epja/i2011-11105-5.

[57] Y. Matsuda et al. “Elastic scattering of protons from ^{9}C with a 290 MeV/nucleon ^{9}C beam”. In: *Phys. Rev. C* 87 (2013), p. 034614. DOI: 10.1103/PhysRevC.87.034614.

[58] Micron Semiconductor Ltd. *Micron Semiconductor Ltd.* http://www.micronsemiconductor.co.uk.

[59] G. Verde et al. “The Farcos project: Femtoscope Array for Correlations and Femtoscopy”. In: *J. Phys.: Conf. Ser.* 420 (2013), p. 012158. DOI: 10.1088/1742-6596/420/1/012158.

[60] A. Pagano et al. “Fragmentation studies with the CHIMERA detector at LNS in Catania: recent progress”. In: *Nucl. Phys. A* 734 (2004), pp. 504–511. DOI: 10.1016/j.nuclphysa.2004.01.092.

[61] Tokyo Institute of Technology. *NEBULA Specifications*. http://be.nucl.ap.titech.ac.jp/~nebula/specifications.php. Neutron-detection system for Breakup of Unstable Nuclei with Large Acceptance.

[62] H. Baba et al. “New data acquisition system for the RIKEN Radioactive Isotope Beam Factory”. In: *Nucl. Instrum. Methods A* 616 (2010), pp. 65–68. DOI: 10.1016/j.nima.2010.02.120.

[63] W. R. Leo. *Techniques for Nuclear and Particle Physics Experiments*. Berlin: Springer, 1987.

[64] O. B. Tarasov and D. Bazin. “LISE++: Radioactive beam production with in-flight separators”. In: *Nucl. Instrum. Methods B* 266 (2008), pp. 4657–4664. DOI: 10.1016/j.nimb.2008.05.110.

[65] J. Hwang. “Study of ^{19}C by One-Neutron Knockout Reaction with a Carbon Target”. PhD thesis. Unknown, 2015.

[66] R. Qiao et al. “A New Uniform Calibration Method for Double-Sided Silicon Strip Detectors”. In: *IEEE Trans. Nucl. Sci.* 61 (2014), pp. 596–601. DOI: 10.1109/TNS.2013.2293342.

[67] J. Kahlbow. "The low-Z Shore of the Island of Inversion: Invariant-mass Spectroscopy of the heavy Fluorine Isotopes $^{29}F^{*}$ & ^{30}F at SAMURAI with NeuLAND". URN: urn:nbn:de:tuda-tuprints-91920. PhD thesis. Technische Universität Darmstadt, 2019.

[68] A. Matta et al. "NPTool: a simulation and analysis framework for low-energy nuclear physics experiments". In: *J. Phys. G* 43 (2016), p. 045113. DOI: 10.1088/0954-3899/43/4/045113.

[69] R. L. Burden and J. D. Faires. *Numerical Analysis*. 9th ed. Brooks/Cole, 2011.

[70] C. Lenain. "Etude des décroissances multi-neutron des isotopes lourds d'hélium et d'hydrogène". NNT: 2021NORMC260. PhD thesis. Normandie Université, 2021.

[71] A. Korsheninnikov et al. "Observation of ^{10}He". In: *Phys. Lett. B* 326 (1994), pp. 31–36.

[72] T. Kobayashi et al. "Quasifree Nucleon-Knockout Reactions from Neutron-Rich Nuclei by a Proton Target: p(^{6}He,pn)^{5}He, p(^{11}Li,pn)^{10}Li, p(^{6}He,2p)^{5}H, and p(^{11}Li,2p)^{10}He". In: *Nucl. Phys. A* 616 (1997), p. 223c.

[73] H. T. Johansson et al. "The unbound isotopes ^{9,10}He". In: *Nucl. Phys. A* 842 (2010), pp. 15–32. DOI: 10.1016/j.nuclphysa.2010.04.009.

[74] Z. Kohley et al. "Unresolved Question of the ^{10}He Ground State Resonance". In: *Phys. Rev. Lett.* 109 (2012), p. 232501. DOI: 10.1103/PhysRevLett.109.232501.

[75] A. Matta et al. "New Findings on Structure and Production of ^{10}He from ^{11}Li with the (d,^{3}He) Reaction". In: *Phys. Rev. C* 92 (2015), p. 041302.

[76] S. I. Sidorchuk et al. "Structure of ^{10}He Low-Lying States Uncovered by Correlations". In: *Phys. Rev. Lett.* 108 (2012), p. 202502.

[77] L. V. Grigorenko and M. V. Zhukov. "Problems with the interpretation of ^{10}He ground state". In: *Phys. Rev. C* 77 (2008), p. 034611.

[78] P. G. Sharov et al. "Anomalous Population of ^{10}He States in Reactions with ^{11}Li". In: *Phys. Rev. C* 90 (2014), p. 024610.

[79] M. D. Jones et al. "Further Insights into the Reaction ^{14}Be(CH_2, X)^{10}He". In: *Phys. Rev. C* 91 (2015), p. 044312.

[80] S. Aoyama. “Theoretical Prediction for the Ground State of ^{10}He with the Method of Analytic Continuation in the Coupling Constant”. In: *Phys. Rev. Lett.* 89 (2002), p. 052501.

[81] H. T. Fortune. “Relative Population of 0^+ States in ^{10}He in Various Reactions”. In: *Phys. Rev. C* 88 (2013), p. 054623.

[82] R. Brun and F. Rademakers. “ROOT – An Object Oriented Data Analysis Framework”. In: *Proc. AIHENP’96 Workshop, Lausanne*. Vol. 389. 1997, pp. 81–86.

[83] Hiyama et al. Private communication.

[84] S. Kakigi et al. “Three-Particle Relativistic Kinematics”. In: *Bull. Inst. Chem. Res. Kyoto Univ.* 57.1 (1979), pp. 83–91.

[85] I. Stefan. *n-body-phase-space*. `https://gitlab.in2p3.fr/iulian.stefan/n-body-phase-space.git`.

Résumé en français

Motivation

L'existence d'un noyau dépourvu de protons constitue une question ouverte de longue date en physique nucléaire. Un tel noyau modifierait notre compréhension fondamentale des interactions nucléaires et imposerait une nouvelle compréhension des systèmes massifs riches en neutrons, tels que les étoiles à neutrons. Il est bien établi que les dineutrons ne sont pas liés ; cependant, un assemblage plus grand de neutrons pourrait démontrer le contraire. De nombreux calculs théoriques, utilisant des approches exactes et des approches à N corps, ont été réalisés pour les systèmes à 3 et 4 neutrons au cours des dernières décennies ; cependant, des conclusions contradictoires en ont été tirées. Bien que la plupart concluent qu'aucun système multineutronique lié ne pourrait exister, certains évoquent l'existence de résonances. De multiples expériences ont été menées pour étudier différents systèmes à 3 et 4 neutrons, certaines d'entre elles ayant trouvé des indices de résonances en accord avec certains des calculs théoriques ; toutefois, des études théoriques ultérieures concluent généralement à l'absence de résonances dans le système multineutronique. Ces calculs et ces expériences mettent davantage en évidence la controverse qui règne dans ce domaine.

Le système à 6 neutrons, en particulier, manque de calculs et de prédictions théoriques en raison de sa complexité ; c'est pourquoi une expérience a été proposée à RIKEN dans le but d'étudier ce système. L'objectif était d'exploiter la réaction de diffusion quasi libre ^{14}Be$(p, p\alpha)^{10}$He afin d'observer la désintégration de ^{10}He en un alpha et six neutrons, puis de déterminer les observables du système à 6 neutrons par la méthode de la masse manquante. Comme produit secondaire de cette expérience, une étude des résonances de ^{10}He a été réalisée et les résultats ont été comparés à des travaux antérieurs.

Dispositif expérimental

L'expérience a été réalisée à RIKEN Nishina au moyen du spectromètre SAMURAI. Un faisceau primaire de ^{18}O à 230 MeV/u est produit et entre en collision avec une cible de production de Be afin de produire un faisceau de ^{14}Be d'énergie $\sim$ 150 MeV/u. Le faisceau secondaire est ensuite filtré par le séparateur de fragments BigRIPS et acheminé vers le hall expérimental du spectromètre SAMURAI, où son énergie est déterminée par la méthode du temps de vol à l'aide de détecteurs à scintillation plastique placés en deux points focaux différents de la ligne de faisceau, tandis que sa direction est déterminée à l'aide de deux chambres à dérive placées en amont de la cible.

Le faisceau de ^{14}Be interagit ensuite avec la cible d'hydrogène solide par l'intermédiaire de l'interaction de diffusion quasi libre, qui éjecte un alpha du faisceau et fait reculer un proton de la cible. Le proton est détecté à l'aide du dispositif ESPRI, qui couvre un domaine de $50° - 70°$ dans le référentiel du laboratoire. ESPRI est constitué de deux bras, chaque bras contenant une chambre à dérive appelée RDC, un large scintillateur plastique et un ensemble de détecteurs à scintillation NaI(Tl). Dans cette analyse, l'angle de diffusion des protons est déterminé à l'aide de la RDC, tandis que leur énergie est déterminée par le temps de vol mesuré par le scintillateur plastique, et l'identification des particules est réalisée par la méthode $\Delta E - ToF$.

Les particules alpha diffusées issues de la réaction de diffusion quasi libre sont détectées à l'aide d'un dispositif appelé télescope, qui couvre les angles avant de $4° - 12°$. À l'instar d'ESPRI, le télescope est également constitué de deux bras, chaque bras contenant un détecteur DSSD et un ensemble de détecteurs à scintillation CsI(Tl). L'angle de diffusion de l'alpha est déterminé à l'aide du DSSD, tandis que son énergie totale est déterminée à partir de la perte d'énergie dans le DSSD et de l'énergie restante déposée dans le détecteur CsI(Tl). L'identification des particules a été réalisée par la méthode $\Delta E - E$.

L'angle de la particule alpha issue de la désintégration de ^{10}He est déterminé à l'aide d'une chambre à dérive située après la cible et avant l'aimant SAMURAI, et l'énergie de cet alpha est déterminée à partir de sa rigidité magnétique ($B\rho$) en exploitant l'aimant SAMURAI ainsi que les chambres à dérive situées avant et après l'aimant.

Enfin, les résidus de la désintégration de ^{10}He sont déterminés à l'aide de deux murs de scintillateurs plastiques placés après la chambre à dérive en aval de l'aimant, appelés l'hodoscope. Un mur de scintilla-

teurs plastiques placé le long de l'axe de la ligne de faisceau, appelé NEBULA, a été utilisé pour filtrer les événements liés aux neutrons afin de réduire le bruit de fond.

Analyse

L'analyse des différents systèmes de détection a été réalisée afin de déterminer les angles et les énergies de diffusion du faisceau, des protons de recul et de l'alpha diffusé, ce qui permet de déterminer l'énergie et l'angle de diffusion de ^{10}He par la méthode de la masse manquante. Une correction de l'étalonnage du temps de vol des protons mesuré par les scintillateurs plastiques d'ESPRI a été effectuée, ce qui a amélioré la résolution en énergie d'excitation. Cette amélioration a été réalisée à l'aide d'un faisceau de ^{12}Be à 150 MeV/u sur la même cible d'hydrogène solide avec la même réaction de diffusion quasi libre. Par la suite, l'énergie d'excitation du système à 6 neutrons a été déterminée par la méthode de la masse manquante à partir de l'énergie de ^{10}He et de celle de l'alpha de désintégration ; cette dernière a été déterminée par un calcul de $B\rho$. Ensuite, une simulation de la résolution de ^{10}He et du système à 6 neutrons a été réalisée afin de permettre une étude expérimentale rigoureuse des résonances de ^{10}He et du système à 6 neutrons. Enfin, un calcul d'espace de phase du système à 6 neutrons a été effectué afin de pouvoir le comparer aux données expérimentales et de les interpréter.

Résultats et discussion

L'analyse des données de ^{10}He a été réalisée en ajustant le spectre de ^{10}He par une fonction de Voigt et en extrayant l'énergie et la largeur des différentes résonances. Ces résonances ont été comparées à des publications antérieures, et un accord a été observé entre le présent travail et les études antérieures pour la résonance de l'état fondamental et celle du premier état excité, dans les limites des marges d'erreur. Ensuite, la comparaison entre le spectre en énergie d'excitation du système 6n et le calcul d'espace de phase a été effectuée et, bien que quelques événements situés au-dessus de l'espace de phase aient été observés, la faible statistique et le bruit de fond élevé ont empêché une interprétation concluante de ces événements en tant que résonance dans le système 6n.

Conclusion

Le premier spectre de masse manquante du système à 6 neutrons a été obtenu à partir de la réaction de diffusion quasi libre ^{14}Be$(p, p\alpha)^{10}$He. Des calculs d'espace de phase ont été réalisés et comparés aux données expérimentales. Quelques événements situés au-dessus de l'espace de phase ont été observés ; cependant, aucune conclusion définitive n'a pu être tirée en raison de la faible statistique et du bruit de fond élevé. Comme sous-produit de l'analyse, une spectroscopie de ^{10}He a été réalisée à l'aide d'un ajustement de Voigt, et les résultats ont été comparés à des travaux antérieurs. Un accord a été trouvé (dans les limites des erreurs) entre ce travail et les expériences antérieures. Les perspectives futures concernant ces données ont été évoquées et des améliorations possibles sont en cours.